



Telomerase-targeting radiopharmaceuticals for the selective treatment of cancer

A thesis presented for the degree Doctor of Philosophy

By

Bas Maarten Bavelaar
CR-UK/MRC Oxford Institute for Radiation Oncology
Hertford College

Supervisor
Professor Katherine Anne Vallis

Trinity Term 2018

Telomerase-targeting radiopharmaceuticals for the selective treatment of cancer

Word count: 32232

C'est ton
qui fait la musique

ABSTRACT

Title: Telomerase-targeting radiopharmaceuticals for the selective treatment of cancer
Author: Bas Maarten Bavelaar MSc || Affiliation: Hertford College || Submission: Trinity 2018
Award programme: Doctor of Philosophy in Radiobiology

Background
Telomerase is a ribonucleoprotein that is expressed in the majority of malignancies, whilst being largely absent in differentiated tissue. Previous research has shown that short-term inhibition of telomerase can lead to radiosensitisation of cancer cells. It has been shown previously that enhanced retention and nuclear localisation of transfected Indium-111 (^{111}In)-labelled oligonucleotides, targeted to the RNA template of telomerase (hTR), resulted in a telomerase-dependent cytotoxic induction of DNA double-strand breaks.

Aim
The aim of this DPhil project was to develop an *in vitro* and *in vivo* delivery system for ^{111}In-labelled anti-hTR oligonucleotides. To this end, we set out to synthesise and characterise ^{111}In-labelled anti-telomerase gold nanoparticle (AuNP) constructs that can be targeted to the tumour site with ultrasound-activatable cavitation nuclei.

Results
hTR complementary (Match) or non-complementary (Scramble) oligonucleotides were conjugated to DTPA for labelling with the Auger electron-emitter ^{111}In. AuNP, 15.5 nm in diameter, were synthesised by citrate reduction and decorated with a monofunctional layer of oligonucleotides (ON-AuNP) or a multifunctional layer of oligonucleotides, PEG800-SH and the cell-penetrating peptide Tat (ON-AuNP-Tat).
The synthesised AuNP constructs were found to greatly enhance the cellular uptake of radiolabelled oligonucleotides, whilst retaining the ability to inhibit telomerase activity. The addition of Tat on the AuNP surface resulted in increased nuclear localisation, as shown in internalisation and fractionation experiments, as well as confocal and transmission electron microscopy. This uptake resulted in a significant dose-dependent impact of ^{111}In-Match-AuNP-Tat on the clonogenic survival of a telomerase-positive cell line, but not telomerase-negative cells, and corresponded with an increase in DNA double-strand breaks. ^{111}In-Match-AuNP did not reduce clonogenic survival, which is partly attributed to the lower nuclear uptake of the construct. For this reason, only ^{111}In-Match-AuNP-Tat was taken forward into the animal studies.
It was found in a biodistribution study of ^{111}In-Match-AuNP-Tat and ^{111}In-Scramble-AuNP-Tat that the AuNP constructs accumulated in the liver with low tumour uptake. To mitigate this effect, nanocups, ultrasound-activatable cavitation agents, were used to direct the AuNP constructs to the tumour. Nanocups significantly increased extravasation of Cy5-Match-AuNP-Tat in an *in vitro* model, and was therefore trialled in an *in vivo* setting. A pilot study demonstrated promising tumour uptake, prompting ongoing research of this delivery strategy.

Conclusions
This DPhil study has delivered a solution for the subcellular targeting of radiolabelled anti-hTR oligonucleotides by using an AuNP-based system. This novel approach of combined modality telomerase-targeting may be a start for future *in vivo* research with ultrasound-mediated delivery. The techniques described in this thesis may provide a building block for nucleic acid-based radiopharmaceutical research.

DECLARATION

This thesis is a presentation of my original research work. Work previously accepted for submission and collaborator contributions are listed below.

- Fig. 1.1 B: Image adapted with permission from Nguyen et al. (2018). Copyright by Springer Nature.
- Fig. 2.1 and 2.2: Adapted from Dr H. Lea-Banks.
- Fig. 4.2: This figure has been partly adapted from previous work submitted for the degree of Master of Science in Radiation Biology and Oncology. Department of Oncology, University of Oxford.
- Fig. 4.6: Dr E. Johnson performed the cutting of the sample for TEM.
- Fig. 5.1 B: Image adapted with permission from Kwan et al. (2015). Copyright John Wiley & Sons, Inc.
- Fig. 5.3: Experiment performed in collaboration with Dr V. Kersemans and S. Able.
- Fig. 5.4: Experiment performed in collaboration with Dr H. Lea-Banks.
- Fig. 5.5-5.7: Experiments performed in collaboration with Prof R. Carlisle, Dr C. Mannaris and Dr H. Lea-Banks.

ACKNOWLEDGEMENTS

After ten years in higher education, writing this piece as the last part of my thesis feels like the end of an era. Although I don't have the pretention that this thesis makes its way to even a fifth of the people that I mention here, I strongly believe that it is an important moment for self-reflection. The writing of these acknowledgements has created a great awareness of the positive influence that so many people have had on my professional and personal development, and I am very grateful to have these people in my life.

First and foremost, I thank my supervisor, Prof Kate Vallis, for the privilege of working in her lab group. Her scientific knowledge, friendly words, and unwavering patience with my opinionated way of working have been essential for the development of this thesis.

I am indebted to Cancer Research UK, their volunteers and sponsors for supporting me and my research over the past four years, as well as the Dutch funding bodies Studiefonds 'Ketel 1' and the Prins Bernhard Cultuurfonds for their financial contributions.

I also extend my gratitude to my DPhil examiners, as well as my transfer assessors Prof Tim Maughan and Prof Bart Cornelissen, for bearing my writings. Thanks to the members of my thesis committee, Dr Lei Song and Prof Madalena Tarsounas, for the opportunity to learn from such excellent scientists.

I am grateful to my collaborators at IBME, in particular Dr Harriet Lea-Banks and Prof Carlisle, whose hard work and intellectual input have been crucial in the development of Chapter 5 of this thesis.

It has been an honour to have worked alongside the intelligent people in my lab group, who created a culture of support, friendliness and hard work devoid of competition. Sarah, your constant availability to answer both difficult and easy questions has been absolutely essential in the development of this work and I am very grateful to you. Martin, I appreciated all of our conversations, and I will miss them from a professional and personal point of view. Your scientific input on my work has been invaluable, and I learned a lot from you. Nadia, thanks for all the insights and encouraging words. Irini, thank you for dealing with my rants about clonogenics, football and everything in between, you have been a great support. Edyta, Elliot, Javian, Eloise, Ole, Richard, Boon, Rachel and Abirami, thanks for the countless hours you have helped me with words, deeds and encouragements.

I also thank Hidde for being there with me for the biggest part of this journey, and never failing to beat my grades, no matter how hard I tried. Without this one-sided competition, as well as your friendship, I would not have been here.

To my Hertford College friends, especially Rory, Francis and Naomi: Thank you for making me feel at home in Oxford from the first day I arrived here. Your presence in my life has been more enriching than my words can express.

To my friends from back home: Leaving the Netherlands was one of the hardest things I have done, and your support pulled me through. De Eerlijke app, Jasper, Daan, Johan and Vincent: I am very lucky to have friends like you, who have come to visit me more times than I can count. Thanks for keeping me sane, sociable and welcome in the Netherlands, it has been very important to me. The same accounts for the Bouwstraat and other Utrecht friends, especially Jeroen and Jorg, who gave me the required dose of madness when I drowned myself in work.

Thanks to my two younger brothers, Koen and Tom, for their tacit but ever-present support. I admire the way you both live your lives and you are in many ways inspirational to me.

My parents have been the single-greatest supporters throughout my life. Their unshakable love, help and patience with me and my ambition make them the greatest parents a man can wish for. Sandra, I am certain that I would not be finishing this DPhil without all your library visits, and, Ton, the same accounts for our many hours on the football pitch dealing with highs and lows. Bedankt voor alles.

Lastly, to my fiancée, who I met at the most unexpected of times, at the most beautiful of times: Jessica, words fail to describe the positive influence you have on me. Free time is more enjoyable, work more meaningful and the world more colourful since you are in my life. Thanks for the fun, support and love that you give, you will always be the best thing I have taken with me from Oxford.

TABLE OF CONTENTS

Abstract ..... **I**

Declaration ..... **II**

Acknowledgements ..... **III**

List of submissions and funding ..... **VIII**

List of abbreviations ..... **IX**

List of figures ..... **XII**

List of tables ..... **XIII**

Chapter 1. Introduction **1**

1.1 Cancer **1**

1.2 Telomerase **1**

1.2.1 Telomerase structure and biogenesis 1

1.2.2 Canonical function of telomerase 4

1.2.3 Non-canonical functions of telomerase 6

1.2.4 Telomerase as a target for drug discovery 9

1.2.5 Telomeres, telomerase and radiosensitivity 11

1.3 Targeted radionuclide therapy **11**

1.3.1 Radionuclide properties and radiobiological implications 12

1.3.2 Nuclear targeting with TRT 14

1.3.3 hTR targeting with TRT 15

1.4 Delivery of radiolabelled oligonucleotides **16**

1.4.1 Barriers for oligonucleotide delivery 16

1.4.2 Gold nanoparticles 17

1.4.3 Gold nanoparticles for the delivery of oligonucleotides 17

1.4.4 Gold nanoparticles and cell-penetrating peptides 19

1.5 Aims of the study **21**

Chapter 2. Materials and methods **22**

2.1 Tissue culture **22**

2.2 Synthesis **22**

2.2.1 Oligonucleotides 22

2.2.2 Gold nanoparticles 22

2.2.3 Fluorophore-labelling of oligonucleotides 24

2.2.4 Radiolabelling of oligonucleotides 24

2.2.5 ON-AuNP conjugates 25

2.2.6 ON-AuNP radiolabelling 26

2.3 Telomeric repeat amplification protocol **26**

2.3.1 Cell lysate extraction 26

2.3.2 TRAPeze XL 26

2.4 Internalisation and fractionation assays **27**

2.5 Confocal microscopy **28**

2.5.1 Subcellular distribution studies 28

2.5.2 γH2AX studies 28

2.6 Transmission electron microscopy **29**

2. 7 Clonogenic assay **30**

2.8 In vitro model for ultrasound-mediated AuNP delivery **31**

2.9 Animal studies 32
2.9.1 Pharmacokinetics and biodistribution of ^{111}In-ON-AuNP-Tat 34
2.9.2 Ultrasound-mediated tumour delivery of Cy5-Match-AuNP 34

2.10 Statistical analysis 36

Chapter 3. Synthesis of gold nanoparticle radiopharmaceuticals 37

3.1 Introduction 37
3.1.1 Therapeutic oligonucleotides 38
3.1.2 Radiolabelled oligonucleotides 39
3.1.3 Oligonucleotide-decorated gold nanoparticles 40
3.1.4 Cell-penetrating peptide – decorated gold nanoparticles 41
3.1.5 PEGylation of gold nanoparticles 41
3.1.6 Aims and outline 42

3.2 Methods 42

3.3 Results 42
3.3.1 Oligonucleotide modifications 42
3.3.2 Gold nanoparticle synthesis 44
3.3.3 Gold nanoparticle functionalisation 47
3.3.4 Gold nanoparticle radiolabelling 49
3.3.5 Gold nanoparticle stability 50

3.4 Discussion 51
3.4.1 Oligonucleotides were modified with 5'end fluorophores and ^{111}In-DTPA 51
3.4.2 Gold nanoparticles were synthesised for drug delivery 52
3.4.3 Gold nanoparticles were functionalised with oligonucleotides 53
3.4.4 Gold nanoparticles were functionalised with oligonucleotides and Tat 54
3.4.5 Ultra-small gold nanoparticles were functionalised with oligonucleotides 55
3.4.6 Concluding remarks 56

Chapter 4. In vitro characterisation of gold nanoparticle radiopharmaceuticals 57

4.1 Introduction 57
4.1.1 Telomerase inhibition with radiolabelled oligonucleotides 57
4.1.2 Subcellular distribution of gold nanoparticle constructs 59
4.1.3 Telomerase and gold nanoparticle radiosensitisation 60
4.1.6 Aims and outline 61

4.2 Methods 61

4.3 Results 61
4.3.1 Telomerase inhibition 61
4.3.2 Subcellular distribution of gold nanoparticle constructs 64
4.3.3 Clonogenic survival 68
4.3.4 Radiosensitisation assays 71
4.3.5 γH2AX assays 72

4.4 Discussion 74
4.4.1 Dose-dependent inhibition of telomerase by gold nanoparticle constructs 74
4.4.2 Cellular and nuclear uptake of gold nanoparticle constructs 76
4.4.3 ^{111}In-Match-AuNP-Tat induces cytotoxic DNA double-strand breaks 80
4.4.4 Concluding remarks 83

Chapter 5. In vivo assessment of gold nanoparticle radiopharmaceuticals 84

5.1 Introduction 84
5.1.1 In vivo delivery of gold nanoparticles 84
5.1.2 Ultrasound-mediated drug delivery 86
5.1.3 Aims and outline 89

5.2 Methods 89

5.3 Results 89
5.3.1 Xenograft model 89

5.3.2 In vivo and ex vivo biodistribution of ^{111}In-Match-AuNP-Tat 90
5.3.3 In vitro ultrasound-mediated delivery of gold nanoparticle constructs 92
5.3.4 IVIS detection of gold nanoparticle constructs 92
5.3.5 In vivo ultrasound-mediated delivery of gold nanoparticle constructs 94
5.3.6 In vivo ultrasound-mediated delivery of gold nanoparticle constructs in CT26 xenografts 96

5.4 Discussion 97
5.4.1 Match-AuNP-Tat accumulates in liver and spleen 98
5.4.2 Ultrasound-activated nanocups resulted in extravasation of Match-AuNP-Tat in vitro 99
5.4.3 Ultrasound-activated nanocups have a mixed effect in vivo 100
5.4.4 Concluding remarks 102

Chapter 6. Discussion 103

6.1 hTR-targeting gold nanoparticle radiopharmaceuticals 103

6.2 In vitro perspectives and future work 104
6.2.1 Internalisation and uptake 104
6.2.2 Molecular biology and radiosensitisation 106
6.2.3 Binding properties 106

6.3 In vivo perspectives and future work 107

6.4 Clinical perspectives 109

6.5 Summary and conclusion 110

References 112

LIST OF SUBMISSIONS AND FUNDING

Papers

- Bavelaar, B.M., B.Q. Lee, M.R. Gill, N. Falzone, and K.A. Vallis. 2018. Subcellular targeting of theranostic radionuclides. *Frontiers in Pharmacology*. Accepted.
- Jackson, M.R., B.M. Bavelaar, P. Waghorn, M.R. Gill, A.H. El-Sagheer, T. Brown, and K.A. Vallis. 2018. Dual-action ^{111}In-labelled oligonucleotides against the RNA subunit of telomerase inhibit enzymatic activity and are radiotoxic against telomerase-positive cancer cells. *In preparation*.
- Bavelaar, B.M., M.R. Jackson, M.R. Gill, S. Able, I. Skaripa-Koukelli, L. Song, P. Waghorn, M. Tarsounas, and K.A. Vallis. 2018. Gold nanoparticle radiopharmaceuticals for the selective treatment of telomerase-positive tumours. *In preparation*.

Presentations

- Bavelaar, B.M., M.R. Jackson, L. Song, P. Waghorn, M. Tarsounas, and K.A. Vallis. 2016. Gold nanoparticle radiopharmaceuticals for the selective treatment of telomerase-positive tumours. *National Cancer Research Institute Conference 2016*.
- Bavelaar, B.M., M.R. Jackson, L. Song, P. Waghorn, M. Tarsounas, and K.A. Vallis. 2016. Gold nanoparticle radiopharmaceuticals for the selective treatment of telomerase-positive tumours. *European Radiation Research Society 2016*.
    - Best Poster Prize

Other Coverage

- Cancer Research UK Press release
    - http://www.cancerresearchuk.org/about-us/cancer-news/press-release/2016-11-08-gold-nanoparticles-help-deliver-lethal-one-two-punch-to-cancer
- BBC Radio 5
    - http://www.bbc.co.uk/programmes/b081mrxk#play
    - From 57:00
- The ASCO Post
    - http://www.ascopost.com/News/44107
- The Sun
    - https://www.thesun.co.uk/living/2135400/tiny-gold-particles-armed-with-disease-busting-drugs-destroy-cancer-cells/

Funding

- Cancer Research UK Prize Studentship
- Studiefonds 'Ketel 1' Scholarship
- Prins Bernhard Cultuurfonds Scholarship

LIST OF ABBREVIATIONS

Abbreviation	Description
%I.D./g	Percentage of the injected dose per gram of tissue
^{111}Cd	Cadmium-111
$^{111}InCl_3$	^{111}Indium chloride
^{131}I	Iodine-131
^{137}Cs	Cesium-137
^{177}Lu	Lutetium-177
2'OMe	2'-O-methylated
$^{223}RaCl_2$	Radium-223 dichloride
^{90}Y	Yttrium-90
ATR	Ataxia telangiectasia and Rad3 related
Au	Gold
AUC	Area under the curve
AuNP	Gold nanoparticle
BCA	Bicinchoninic acid
BDMA	Benzyl dimethylamine
CHK1	Checkpoint kinase 1
CPM	Counts per minute
CPP	Cell-penetrating peptide
CSDA	Continuous-slowing-down-approximation
CTE	C-terminal extension
DAPI	4', 6-diamidino-2-phenylindole
DDR	DNA damage response
DLS	Dynamic light scattering
DMEM	Dulbecco's Modified Eagle's Medium
DMSO	Dimethyl sulfoxide
DNA	Deoxyribonucleic acid
DNA-PKcs	DNA-dependent protein kinase catalytic subunit
DTPA	Diethylenetriaminepentaacetic dianhydride
DVB	Poly(styrene-co-divinylbenzene)
EBR	External beam radiation
EGFP	Enhanced green fluorescent protein
FCS	Foetal bovine serum
FUS	Focussed ultrasound
GMD	Geometric mean diameter
h	Hour
H_2O_2	Hydrogen peroxide
$HAuCL_4$	Hydrogen tetrachloroaurate (III)
HCl	Hydrochloric acid

HEMA	Hydroxyethylmethyl methacrylate
HNO_3	Hydrogen nitrate
hnRNP A1	Heterogeneous nuclear ribonucleoprotein A1
HP1	Heterochromatin protein 1
HPLC	High-performance liquid chromatography
hTERT	Human telomerase reverse transcriptase
hTR	Human telomerase RNA subunit
i.v.	Intravenous
IBME	Oxford Institute of Biomedical Engineering
IL	Interleukin
iNC	Inactivated nanocups
IVIS	*In vivo* imaging system
LET	Linear energy transfer
MAP	Model amphipathic peptide (MAP)
$MgCl_2$	Magnesium chloride
MID	Mean inactivation dose
min	Minute
MMA	Methyl methacrylate
mRNA	Messenger RNA
$Na_3C_6H_5O_7$	Trisodium citrate
NaCl	Sodium chloride
$NaH_2C_6H_5O_7$	Sodium citrate
$NaHCO_3$	Sodium hydrogen carbonate
NaOH	Sodium hydroxide
NC	Nanocup
NLS	Nuclear localisation sequence
NPS	N3'→P5'-thiophosphoramidate
ON-AuNP	Oligonucleotide-functionalised 15.5 nm AuNP
ON-AuNP-Tat	Oligonucleotide/PEG-SH/Tat-functionalised 15.5 nm AuNP
ON-uAuNP	Oligonucleotide-functionalised 2.4 nm AuNP
OsO_4	Osmium tetroxide
p.i.	Post-injection
PCD	Passive cavitation detector
PEG-SH	Polyethylene glycol methyl ether thiol
PET	Positron emission tomography
PIPES	1,4-piperazinediethanesulfonic acid buffer
POT1	Protection of telomeres 1
PS	Phosphorothioate
PSG	Penicillin/streptomycin/glutamate
PSMA	Prostate specific-membrane antigen
PTDs	Protein transduction domains
RAP1	Repressor and activator protein 1

RES	Reticuloendothelial system
RNA	Ribonucleic acid
ROS	Reactive oxygen species
RPA	Replication protein A
rRNA	Ribosomal RNA
s	Second
S	Sulphur
scaRNA	Small Cajal body RNA
SEC	Size exclusion chromatography
SER	Sensitiser enhancement ratio
SF	Surviving fraction
SiRNA	Silencing RNA
snoRNA	Small nucleolar RNA
snRNA	Small nuclear RNA
SPECT	Single-photon emission computed tomography
SRS	Single-stranded DNA retention surface
SSB	Single-strand break
T:B ratio	Tumour-to-background ratio
TEM	Transmission electron microscope
TEN	telomerase N-terminal
THPC	Tetrakis(hydroxymethyl)phosphonium chloride
TIN2	TRF1-interacting nucleotide protein 2
TLC	Thin-layer chromatography
TNF	Tumour necrosis factor
TRBD	hTR-binding domain
TRF1	Telomeric repeat-binding factor 1
TRF2	Telomeric repeat-binding factor 2
TRT	Targeted radionuclide therapy
TS	Telomerase substrate
UV-Vis	ultraviolet – visible

LIST OF FIGURES

Figure	Name	Page
1.1	Structure of hTR and hTERT	2
1.2	The telomerase catalytic cycle	5
1.3	Non-canonical function of hTR in the phosphorylation of hnRNP A1	8
1.4	Radionuclide properties	14
2.1	Schematic illustration of the in vitro ultrasound setup	33
2.2	Schematic representation of the in vivo ultrasound delivery set-up	35
3.1	AuNP constructs	37
3.2	DTPA dianhydride conjugation	39
3.3	Schematic representation of the synthesis of hTR-targeting AuNP	43
3.4	Oligonucleotide 5'end modifications	44
3.5	AuNP properties	45
3.6	Functionalisation of Match-AuNP and Scramble-AuNP	47
3.7	Functionalisation of Match-AuNP-Tat and Scramble-AuNP-Tat	48
3.8	Functionalisation of Match-uAuNP and Scramble-uAuNP	49
3.9	TLC data from ON-AuNP, ON-AuNP-Tat, and ON-uAuNP after purification	50
3.10	AuNP stability	51
4.1	TRAP assay steps	58
4.2	Telomerase activity inhibition with oligonucleotides and AuNP	63
4.3	Internalisation and fractionation of AuNP constructs after 24 h	65
4.4	Subcellular distribution of AuNP constructs in MDA-MB-435 cells after incubation for 2.5 h	66
4.5	Subcellular distribution of AuNP constructs in MDA-MB-435 cells after incubation for 24 h	67
4.6	Subcellular distribution of AuNPs in MDA-MB-435 cells after incubation for 24 h with TEM	69
4.7	Clonogenic survival of cell lines after treatment for 24 h with AuNP constructs	70
4.8	Effect of ON-AuNP-Tat on radiosensitivity	72
4.9	γH2AX foci after treatment of cells with ^{111}In-labelled ON-AuNP-Tat	73
5.1	Ultrasound-mediated drug delivery	87
5.2	Tumour growth curve of MDA-MB-435 xenografts	89
5.3	SPECT imaging and ex vivo biodistribution of ^{111}In-Match-AuNP-Tat	91
5.4	*In vitro* ultrasound-mediated extravasation of Cy5-Match-AuNP-Tat	93
5.5	*In vivo* Cy5-Match-AuNP-Tat detection with IVIS	94
5.6	*In vivo* imaging of the effect of ultrasound-activatable nanocups on tumour uptake of Cy5-Match-AuNP-Tat in MDA-MB-435 xenografts	95
5.7	*In vivo* imaging of the effect of ultrasound-activatable nanocups on tumour uptake of Cy5-Match-AuNP-Tat in CT26 xenografts	97

LIST OF TABLES

Table	Name	Page
3.1	hTR-targeting oligonucleotide sequences and 2'-O-methyl modifications	38
3.2	Characteristics of AuNP constructs	46
4.1	MIDs and survival fractions for AuNP constructs and controls	71
4.2	Radiosensitisation and MIDs for Match-AuNP-Tat and Scramble-AuNP-Tat	72

CHAPTER 1. INTRODUCTION

1.1 Cancer

Cancer is a hypernym for a diverse group of malignant diseases, characterised by unrestrained cell division, cellular invasion of adjacent tissue, and metastatic dissemination to distal organs (Hanahan and Weinberg, 2011). In 2017, 17.2 million people worldwide were diagnosed with cancer and 8.9 million people lost their lives as a consequence of malignant disease, emphasising the need for novel therapies (GBD Cancer Collaboration et al., 2018). Various cellular mechanisms play a role in neoplastic disease development, including sustained proliferative signalling, growth suppressor evasion, induction of angiogenesis, cell death resistance, avoidance of the immune system, reprogramming of energy metabolism, genome instability, inflammation, and enabling of replicative immortality (Hanahan and Weinberg, 2011). These hallmarks of cancer may form attractive targets for anticancer therapy due to their differential expression in comparison to normal tissue.

1.2 Telomerase

The focus of this thesis is telomerase, a ribonucleoprotein that is a key player in cancer cell immortality. Telomerase is upregulated in 80-90% of tumours, whilst being sparsely expressed in normal tissue, making it an interesting target for pharmaceutical treatment (Sekaran et al., 2014; Shay and Bacchetti, 1997).

1.2.1 Telomerase structure and biogenesis

Human telomerase is comprised of a telomerase ribonucleic acid (RNA) subunit (hTR), containing the internal template for synthesis of telomeric hexanucleotide deoxyribonucleic acid (DNA) repeats (Fig. 1.1 A); a protein component, telomerase reverse transcriptase (hTERT), which acts primarily as a reverse-transcriptase that catalyses the addition of nucleotides at telomere ends (Fig. 1.1 B); and the accessory proteins dyskerin, NHP2, NOP10, and GAR1

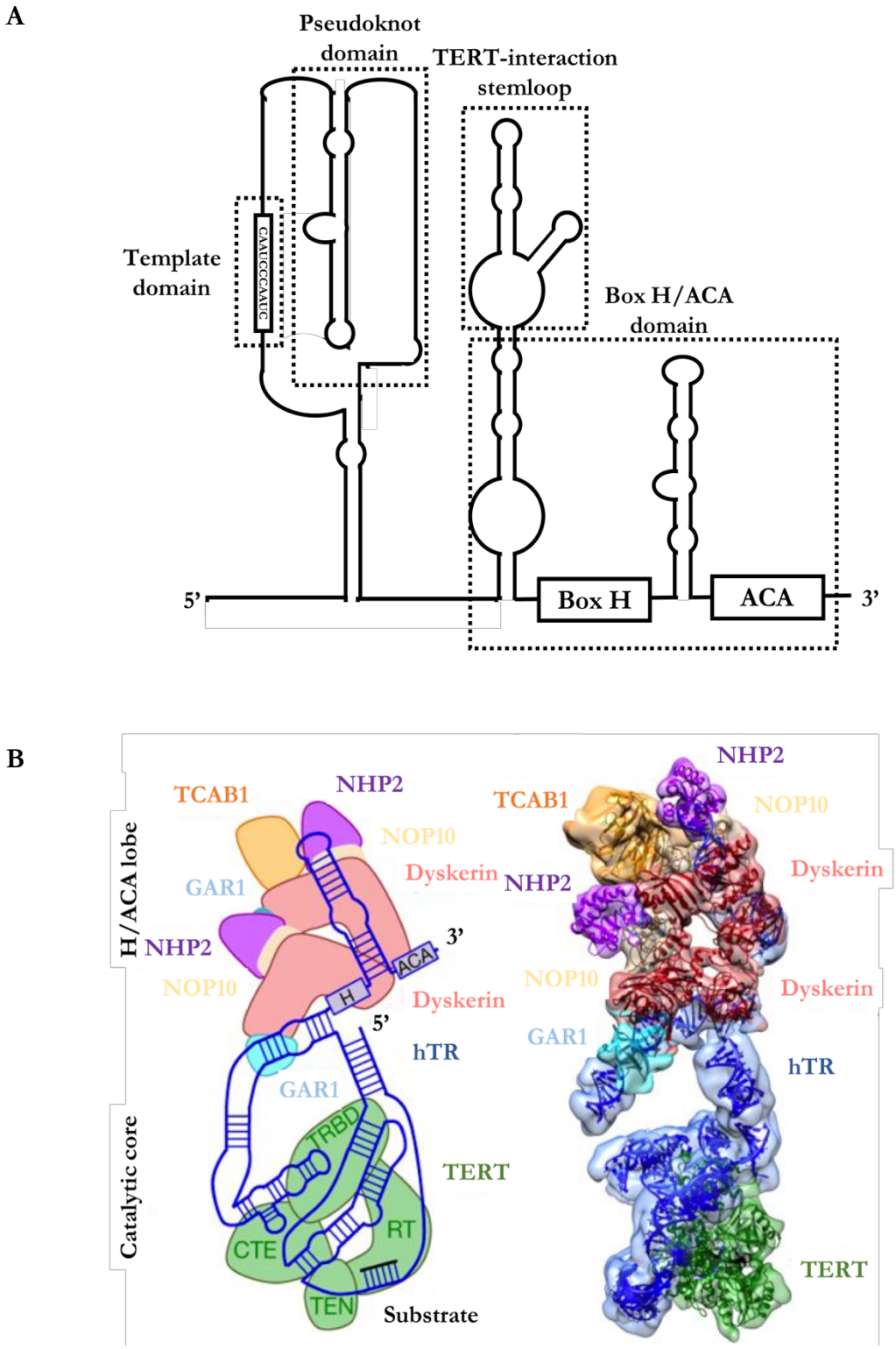


Figure 1.1 Structure of hTR and hTERT. A) The secondary structure of hTR. hTR consists of four key structural domains: The reverse transcriptase template, the pseudoknot, the TERT-binding stem loop and the 3'end H/ACA domain. B) Secondary and tertiary structure of the telomerase holoenzyme. The hTR H/ACA domain binds two sets of dyskerin, NOP10, NHP10 and GAR1. TCAPB1 interacts with dyskerin and the H/ACA domain. Image adapted with permission from Nguyen et al. (2018). Copyright by Springer Nature.

(Jiang et al., 2018; Sauerwald et al., 2013). The formation of the holoenzyme is a multistep process requiring various cofactors (Schmidt and Cech, 2015).

1.2.1.1 hTR synthesis and development

TRs differ in sequence and size between species, ranging from 150 to over 2000 nucleotides. Despite this variation, at least four functional groups are evolutionary conserved: 1) The reverse transcriptase template, 2) the pseudoknot domain, 3) a TERT-interaction stem-loop (CR4/5 domain), and 4) a RNA-stabilising 3' element (Fig. 1.1 A) (Theimer and Feigon, 2006). Mature hTR consists of 451 nucleotides and has all the above mentioned functional features (Zhang et al., 2011). The 3'end RNA-stabilising element is an H/ACA motif that contains two hairpins linked by the H-box, a small single-stranded stretch, and a terminal ACA region (Mitchell et al., 1999). The H/ACA motif is found in other small Cajal body and nucleolar RNAs (scaRNAs and snoRNAs) and associates with the cofactors dyskerin, GAR1, NOP10 and NHP2 (Kiss et al., 2010). hTR is transcribed from its own promoter by RNA polymerase II and cleaved up to the boundary formed by the H/ACA motif-dyskerin association (Feng et al., 1995; Fu and Collins, 2003). Rapid association of the shelterin complex is essential for nuclear accumulation of hTR, and mutations in this complex have been shown to result in reduced telomerase activity due to reduced nuclear levels of hTR (Darzacq et al., 2006).

1.2.1.2 hTERT synthesis

The hTERT protein consists of four functional regions: the telomerase N-terminal (TEN) domain, the reverse transcriptase domain, the hTR-binding domain (TRBD), and the C-terminal extension (CTE) (Fig. 1.1 B) (Blackburn and Collins, 2011). The TEN domain is essential in telomerase recruitment and the catalysis of telomeric repeat synthesis (Robart and Collins, 2011). The reverse transcriptase domain contains the enzymatically active site of the holoenzyme (Nakamura et al., 1997). Furthermore, this domain, together with the TRBD domain, provides the crucial interaction sites with hTR (Lai et al., 2001). The CTE-unit is

adjacent to the reverse transcriptase, but its function is poorly understood (Schmidt and Cech, 2015). hTERT is synthesised in the cytoplasm and associates with two chaperones, HSP90 and p23, for holoenzyme assembly (Holt et al., 1999).

1.2.1.3 Assembly and structural organisation of telomerase

hTR and hTERT are assembled with the aid of AAA^+ ATPases Pontin and Reptin, before TCAB1-mediated recruitment to the Cajal bodies (Venteicher et al., 2008). The hTERT subunit interacts with hTR by binding the penultimate hairpin with the CR4/5 domain. Furthermore, the reverse transcriptase domain associates with the pseudoknot region, although the affinity of this interaction is significantly lower than the TRBD-CR4/5 interaction. RNA encircles TERT in the catalytic core, resulting in a well-ordered tertiary structure (Jiang et al., 2018; Nguyen et al., 2018).

1.2.2 Canonical function of telomerase

The principal function of the telomerase holoenzyme is the addition of simple-sequence repeats to telomeres to counteract DNA erosion (Fig. 1.2) (Wu et al., 2017a). Telomeres are protective structures at chromosome ends that are essential for continued proliferation. Functional telomeres consist of specific and repetitive DNA, containing multiple thousands of base pairs with the repetitive sequence 5'-TTAGGG-3', as well as a single-stranded G-rich 3'end overhang (Sekaran et al., 2014). Furthermore, the chromosome end is capped by the shelterin protein complex, which consists of six proteins: the telomeric repeat-binding factors 1 and 2 (TRF1; TRF2), TRF1-interacting nucleotide protein 2 (TIN2), repressor and activator protein 1 (RAP1), protection of telomeres 1 (POT1) and TPP1 (O'Sullivan and Karlseder, 2010). These telomere-specific proteins have two key functions: maintenance of functional and structural integrity of the telomere and facilitating telomeric DNA replication.

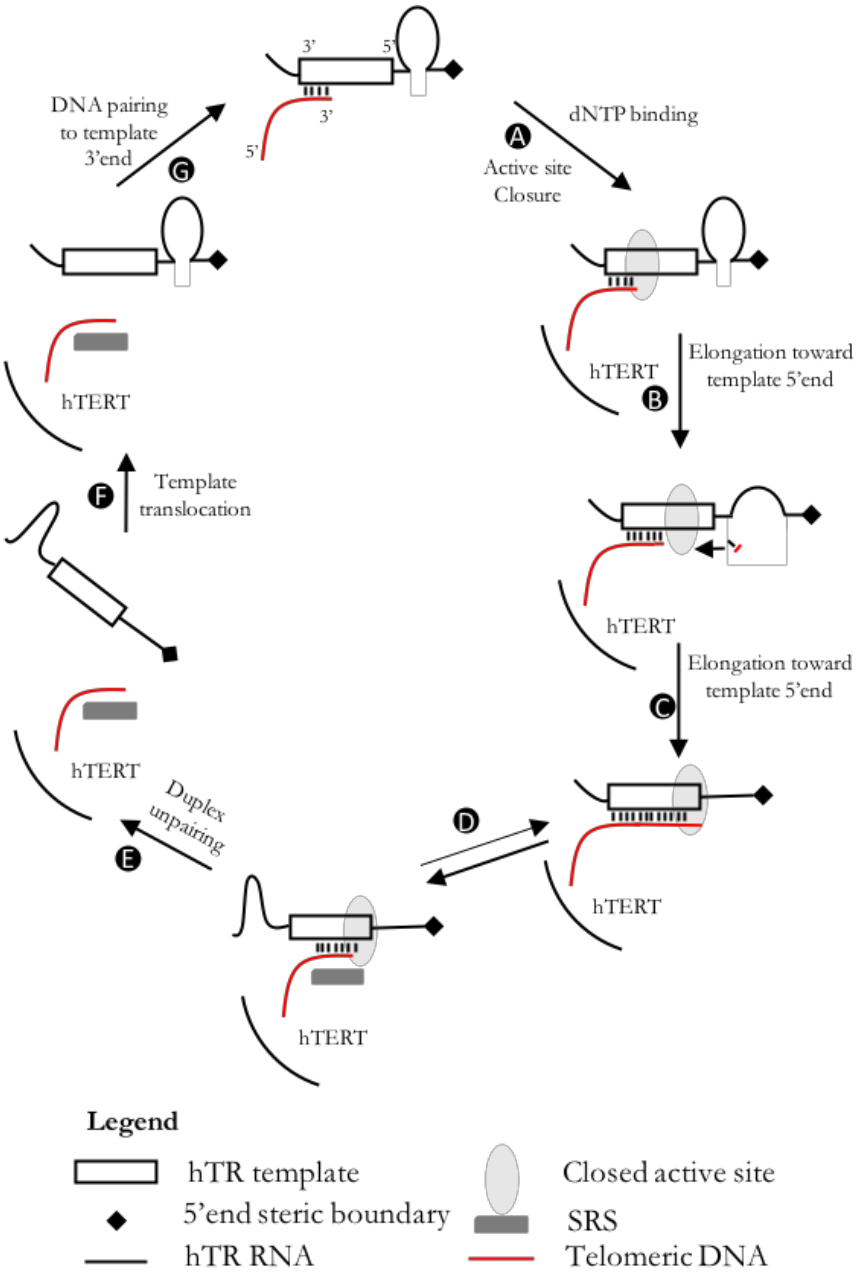


Figure 1.2 The telomerase catalytic cycle. The telomerase catalytic cycle is initiated by DNA primer base pairing of the 3'end template, whilst the 5'end loops out (upper image). A) After duplex and deoxynucleotide triphosphate (dNTP) binding, the holoenzyme active site closes to enable elongation-competent confirmation. B+C) Telomeric DNA is elongated by the hTERT until the 5'end steric barrier is reached. Displacement of the 3'end region occurs when the template 5'end is reeled into the active site. D) Once a critical number of base pairs is displaced (5-7 left) from the active site, confirmation of the 3'end of the template is altered. Subsequently, the strand can either realign for further repeats (thin arrow), or E) favour an active site opening which enables strand separation. F) Previously held base pairs can be kept in place by single-stranded DNA retention surface (SRS) of hTERT, facilitating the fixation of de novo added telomeric repeats during template translocation. G) Following template translocation, a small duplex is formed at the DNA 3'end, which can either be caught by the hTERT central ring for a subsequent round of repeat synthesis or be released to abort further elongation.

Progressive cell divisions in normal somatic cells result in the gradual shortening of telomeres due to the end-replication problem, which is the requirement of DNA polymerase for a labile primer to initiate 5'-3' unidirectional synthesis, causing uncopied 3' end bases. Shortening below a certain threshold results in dysfunctional telomeres (de Lange, 2009). If telomeres are dysfunctional, chromosome ends are identified by DNA damage response (DDR) proteins, which results in senescence or cell death (Jafri et al., 2016). Telomere maintenance is therefore an important survival mechanism for proliferative cancer cells (O'Sullivan and Karlseder, 2010). In humans, telomere maintenance is primarily regulated by telomerase (Greider and Blackburn, 1985).

Telomeric repeat addition is initiated by telomerase accumulation in the Cajal body via TCAB1 activation, after which the ribonucleoprotein is redistributed to telomeres driven by telomerase-TPP1 interactions. At the telomeres, action during the S-phase is facilitated by the recruitment of heterochromatin protein 1 (HP1) (Nandakumar and Cech, 2013). The telomeric catalytic cycle exists of two phases (Fig. 1.2). The first phase involves the addition of nucleotides via synthesis of a telomeric DNA repeat to the 3'end by pairing with the hTR template. The second phase consist out of repeat addition: template regeneration for additional repeat synthesis. This processive synthesis of various telomeric repeats via the same template is a unique polymerase feature and requires a specialist template regeneration mechanism. After six nucleotides, 5'-GGTTAG-3', are attached to the 3' end of the DNA primer from the active site RNA template, nucleotide addition is arrested after which the protein either realigns for additional synthesis, or dissociates (Wu et al., 2017a).

1.2.3 Non-canonical functions of telomerase

Besides the well-known canonical function of telomerase, several non-telomeric functions of hTERT and hTR have been reported (Martínez and Blasco, 2011).

1.2.3.1 TERT

Emerging evidence has demonstrated functions of hTERT beyond telomere-maintenance (Li and Tergaonkar, 2014). hTERT has been shown to influence signalling pathways, gene expression and mitochondrial function, thereby affecting cellular stress and survival (Saretzki, 2014). hTERT functions as a transcriptional modulator of NF-κB signalling via the direct binding of p65, leading to an enhanced expression of pro-inflammatory and cancer-promoting NF-κB target genes such as interleukin (IL)-6, IL-8, and tumour necrosis factor (TNF)-α (Ghosh et al., 2012). Furthermore, hTERT has been demonstrated to serve as a co-factor in a β-catenin transcriptional complex (Park et al., 2009). By interacting with BRG1, it activates Wnt target genes by physically occupying gene promotors, resulting in the expression of proteins involved in proliferation, stem cell renewal and cell survival. Additionally, hTERT has been found in extra-nuclear locations, such as the mitochondria and cytoplasm. hTERT was shown to bind to mitochondrial DNA, increase mitochondrial membrane potential, and interact with mitochondrial tRNAs. The absence of hTERT in the mitochondria was associated with an increased reactive oxygen species (ROS) generation, which negatively impacted cell viability (Sharma et al., 2012).

1.2.3.2 hTR

Although the role of the hTR subunit of telomerase has been less well emphasised for extra-telomeric roles, there has been considerable interest in its interaction with Ku (Fig. 1.3). It is well-established that long non-coding RNAs can play essential roles during malignant transformation by acting as scaffolds for the regulation of protein interactions with other proteins, DNA and RNA (Zhang et al., 2016a). The 47-nucleotide region of the 3'end of hTR interacts with Ku70/80, resulting in the stimulation of DNA-dependent protein kinase catalytic subunit (DNA-PKcs) to phosphorylate heterogeneous nuclear ribonucleoprotein A1 (hnRNP A1) during the G2 and M phases of the cell cycle (Fig. 1.3) (Ting et al., 2005, 2009). hnRNP A1 phosphorylation results in a myriad of downstream effects, including the promotion of

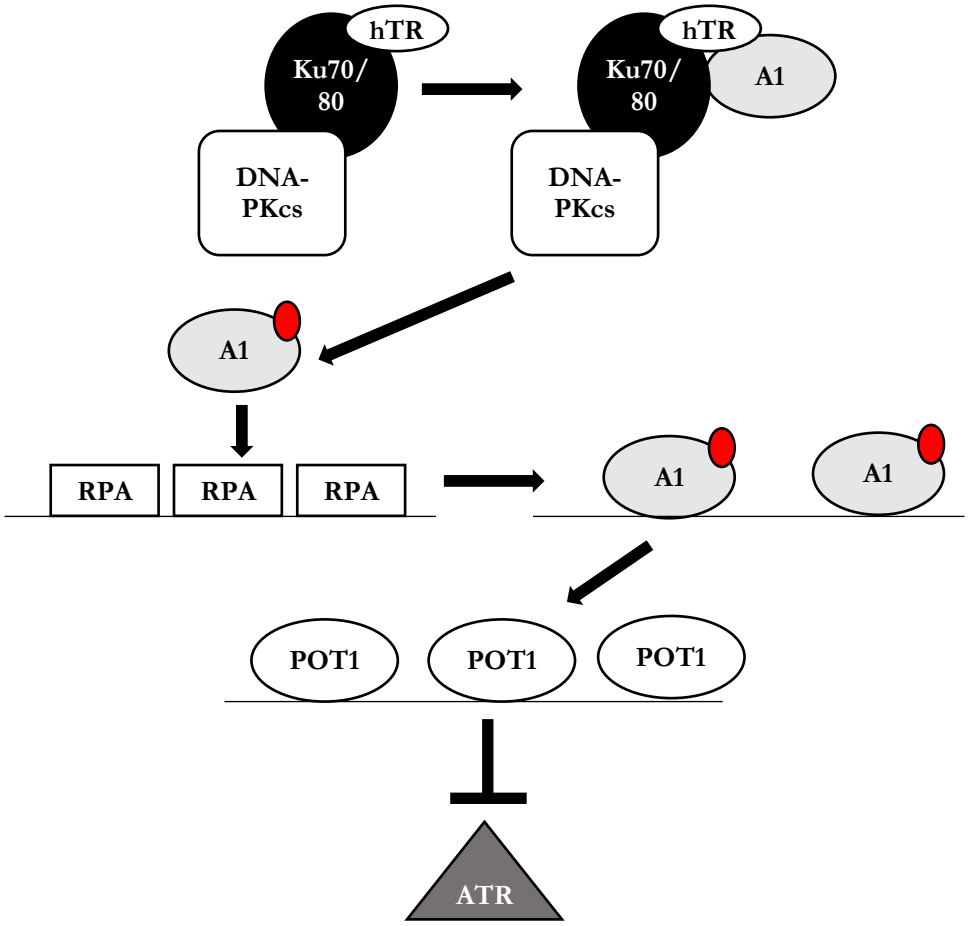


Figure 1.3 Non-canonical function of hTR in the phosphorylation of hnRNP A1. hTR binds Ku70/80 and hnRNP A1, resulting in hnRNP A1 phosphorylation. In S-phase, RPA is associated with telomeric DNA to enable replication and ATR activation. After S-Phase, phosphorylated hnRNP A1 causes RPA displacement, which promotes POT1 accumulation, leading to suppression of ATR activity at telomeres.

replication protein A (RPA)-to-POT1 switching on telomeric single-stranded 3'end overhangs (Flynn et al., 2011). Abrogation of this process leads to RPA-to-POT1 switch impairment, which results in DDR via ataxia telangiectasia and Rad3 related (ATR) protein at telomeres in mitotic cells (Sui et al., 2015). This is in agreement with a study by Kedde et al. (2006). These investigators reported that inhibition of hTR mRNA expression resulted in telomerase-independent growth arrest related to p53 and CHK1 activation. The effects were demonstrated to be mediated via the activation of telomeric ATR, indicating a role for hTR in the DDR and telomere stability regardless of its function in the telomerase holoenzyme. Enhancement of G2/M arrest via ATR upregulation has been associated with cytotoxic and non-proliferative effects, potentially providing a mechanism for short-term hTR-dependent cell kill (DiPaola,

2002). The fact that hTR is more than a template for telomere elongation is further highlighted by a study that showed that hTR can act as a noncoding RNA that protects from cell death independent of its role in long-term telomere preservation in normal human immune cells (Gazzaniga and Blackburn, 2014). An additional role is also found in zebrafish, where it has been shown to modulate myeloid-erythroid fate decision by controlling the levels of the key myeloid and erythroid transcription factors spi1 and gata1, respectively, via stimulation of granulocyte colony-stimulating factor (GCSF) and macrophage colony-stimulating factor (MCSF) (Alcaraz-Pérez et al., 2014).

1.2.4 Telomerase as a target for drug discovery

Proteins exhibiting differential expression and activity in cancer cells when compared to normal cells are appealing targets for treatment strategies. Accordingly, the finding that the ribonucleoprotein telomerase is over-expressed in 80-90% of malignancies, but is absent in in normal differentiated cells, has led to many efforts to validate telomerase as a drug target for anticancer therapy (Shay and Bacchetti, 1997; Sekaran et al., 2014). Several telomerase-targeting strategies have been developed in recent years, including hTERT and hTR inhibitors, vaccines, and gene therapy (Chen and Zhang, 2016). Of particular relevance to this DPhil project is hTR inhibition with antisense oligonucleotides.

1.2.4.1 hTR antisense oligonucleotides

Therapeutic inhibition of telomerase activity in malignant cells results in telomere shortening due to DNA replication during cellular proliferation (Hahn et al., 1999). This erosion of telomeric DNA may eventually lead to senescence or apoptosis, dependent on the cell type (Deng et al., 2008). In the absence of telomerase activity, human cells lose 50-200 base pairs of telomeric DNA during proliferation after each cell cycle (Huffman et al., 2000). Since telomere sizes in human cells range between 5000 and 15000 base pairs, a lag time between the initiation of telomerase inhibition treatments and a phenotypical consequence of telomerase inhibition is

to be expected (Zou et al., 2004). Interestingly, some studies report immediate and short-term effects with antisense oligonucleotides that do not display the phenotypic lag that is characteristic for telomerase activity inhibitors, indicating a mechanism that is independent of telomeric erosion. An explanation may be that these immediate effects are the result of the non-canonical roles of hTR (Wu et al., 2017b).

Several researchers have investigated the potential of hTR antagonists *in vitro* and *in vivo*, including Norton et al. (1996), Pitts and Corey (1998), Herbert et al. (1999) and Beisner et al. (2010). The most prominent example is the development of imetelstat, a chemically modified N3'→P5'-thiophosphoramidate (NPS) 13-nucleotide long antisense oligonucleotide (sequence: 5'-TAGGGTTAGACAA-3') first described by Asai et al. (2003). The NPS modification conferred high stability to the molecule, whilst maintaining a sequence-specific potency for inhibiting hTR (IC_{50}: 0.14 μM). In a later study, the 5'end was modified with a terminal palmitoyl group that was linked via an amide bond to α-aminoglycerol of the thiophosphoramidate, which did not reduce the potency of the compound (Herbert et al., 2005). Many investigators have proven the effect of the drug as a single agent and in combination with chemotherapy or irradiation (Marian et al., 2010; Tokcaer-Keskin et al., 2010; Goldblatt et al., 2009a; b; Gomez-Millan et al., 2007; Hochreiter et al., 2006; Dikmen et al., 2005; Shammas et al., 2008; Djojosubroto et al., 2005). Clinically, the drug has demonstrated potential in recently reported phase II trials (Tefferi et al., 2015; Baerlocher et al., 2015). Fast and sustained haematological and molecular responses were found in patients with essential thrombocythemia (Baerlocher et al., 2015). Imetelstat was also observed to be active in a subset of patients with myelofibrosis (complete or partial response: 21%), but clinically significant myelosuppression was also demonstrated (Tefferi et al., 2015). The success of this compound illustrates the potential of antisense oligonucleotides against hTR and provides a stepping stone for the work in this DPhil project.

1.2.5 Telomeres, telomerase and radiosensitivity

There is a frequently described relation between telomerase, telomeres and radiosensitivity. Telomerase expression is upregulated in response to ionising radiation by a post-translational mechanism via the Ras/phosphatidylinositol 3-kinase/Akt pathway (Ram et al., 2009), which may promote repair of DNA DSBs (Akiyama et al., 2002). Various studies have demonstrated that inhibition of telomerase with antisense oligonucleotides leads to a higher chance of DNA damage following exposure to DNA damaging agents or external beam radiation (Wu et al., 2017b; Yu et al., 2015; Ferrandon et al., 2015; Wu et al., 2012; Agarwal et al., 2008; Gomez-Millan et al., 2007; Ji et al., 2006). This effect is often ascribed to telomerase inhibition-induced telomere shortening and decapping, which renders chromosome ends more susceptible to DNA damage. Indeed, it has been shown by others that telomere dysfunction enhances sensitivity to ionising radiation (Wong et al., 2000; Goytisolo et al., 2000; Castella et al., 2007). However, given the upregulation of telomerase as a consequence of DNA damage, extra-telomeric roles of hTR may also play a role. This is in agreement with other studies that demonstrate short-term effects (Wu et al., 2017b; Ferrandon et al., 2015), indicating that hTR inhibition can radiosensitise cancer cells via pathways involving long- and short-term processes.

1.3 Targeted radionuclide therapy

Based on the radiosensitising effect and nuclear localisation of hTR-targeting antisense oligonucleotides, it was hypothesised that this therapeutic strategy may be enhanced through combination with targeted radionuclide therapy (TRT).

TRT is an anticancer treatment modality that involves the utilisation of radionuclide-conjugated cancer-specific vectors, such as small molecules, peptides, antibodies, and nanoparticles, to selectively deliver cell-killing radiation to the tumour (Bavelaar et al., 2018). TRT is frequently designed as a theranostic treatment; when coupled to appropriate radionuclides it can be used for positron emission tomography (PET) or single-photon emission computed tomography

(SPECT). A large body of data, accumulated over more than 70 years of research, has demonstrated that TRT can be effective in the eradication of cancer cells (Aghevlian et al., 2017; Pouget et al., 2015). Clinically, this has been particularly successful in treatments for lymphoma and leukaemia (Yttrium-90 (^{90}Y)-ibritumomab tiuxetan), as well as for neuroblastoma (Iodine-131 (^{131}I)-MIBG), and prostate cancer (Radium-223 dichloride ($^{223}RaCl_2$)) (Gill et al., 2017; Larson et al., 2015). Recently, the successful NETTER1 trial with Lutetium-177 (^{177}Lu)-Dotatate in patients with midgut neuroendocrine tumours (Strosberg et al., 2017), and the promising results of ^{177}Lu-prostate specific-membrane antigen (^{177}Lu-PSMA) for prostate cancer treatment (von Eyben et al., 2018) have further established the potential value of TRT.

1.3.1 Radionuclide properties and radiobiological implications

Radionuclides are unstable atomic nuclei that decay by electromagnetic radiation emission in the form of X- or γ-rays and by particulate radiation emission in the form of α-particles, β-particles, or Auger electrons (Fig. 1.4) (Bavelaar et al., 2018). Their effect is defined in dosimetric terms by the linear energy transfer (LET), the amount of energy deposited in matter per distance unit. Radionuclides are used widely for therapeutic and diagnostic purposes in cancer medicine. Historically, β-emitters have been the most commonly used class of radionuclides in the therapeutic setting. β-emitters release electrons with a mean energy between 0.2 and 1.0 MeV, leading to a long track path-length with a continuous-slowing-down-approximation (CSDA) range in water of up to 12 mm. Consequently, the LET of β-emitters is low (< 1 keV/μm) (Kassis, 2004). For this reason, β-electrons result in sparse ionisations over several hundreds of cell diameters, meaning that a β-emitter vector may not need to reach each and every tumour cell to achieve the desired anti-tumour effect ('crossfire effect') (Pouget et al., 2015). On the downside, this also results in a higher chance of receiving a significant absorbed dose to normal tissue, which limits the dose that can be administered safely. Furthermore, the low-LET

radiation track means that DNA damage caused by β-electrons may not be sufficient to cause cell death, especially in cancer cells which are often radioresistant.

α-Emitters have been a heavily researched topic over the past decade with the notable example of $^{223}RaCl_2$ being adopted into clinical practise. α-Emitters decay by emission of one or more helium nuclei (α-particles). These particles have an energy ranging from 5 to 9 MeV over an intermediate track path-length in water (50-100 μm), giving rise to a high LET (50-230 keV/μm) (Pouget et al., 2015). α-Particles therefore act over a significantly shorter distance (roughly 5-10 cell diameters) than β-particles, but causes more complex, irreparable DNA damage in every cell that they traverse.

The last major category of therapeutic radionuclides consists of Auger electron-emitters. Auger electron-emitters eject electrons from their high shells following a process called internal atomic ionisation. This process is a result of electron capture or internal conversion, which are nuclear decay modes that interact strongly with atomic shells. Most Auger electrons have a low energy (< 5 keV) and a very low tissue penetration depth (< 0.5 μm) in comparison to α- and β-emitters, leading to a high LET (4-26 keV/μm) (Lee et al., 2015). Auger electrons cause dense ionisation over a very short range (nanometre scale), which means that these type of radionuclides are relatively harmless unless they are in close proximity to a targeted, sensitive organelle (Falzone et al., 2015). This feature can be highly beneficial in reducing the side effects of TRT as, unlike α-or β-particles, non-targeted adjacent cells remain unharmed. For the radiopharmaceutical to be effective in the targeted cell, however, subcellular targeting is crucial to achieve the optimal anti-tumour effect.

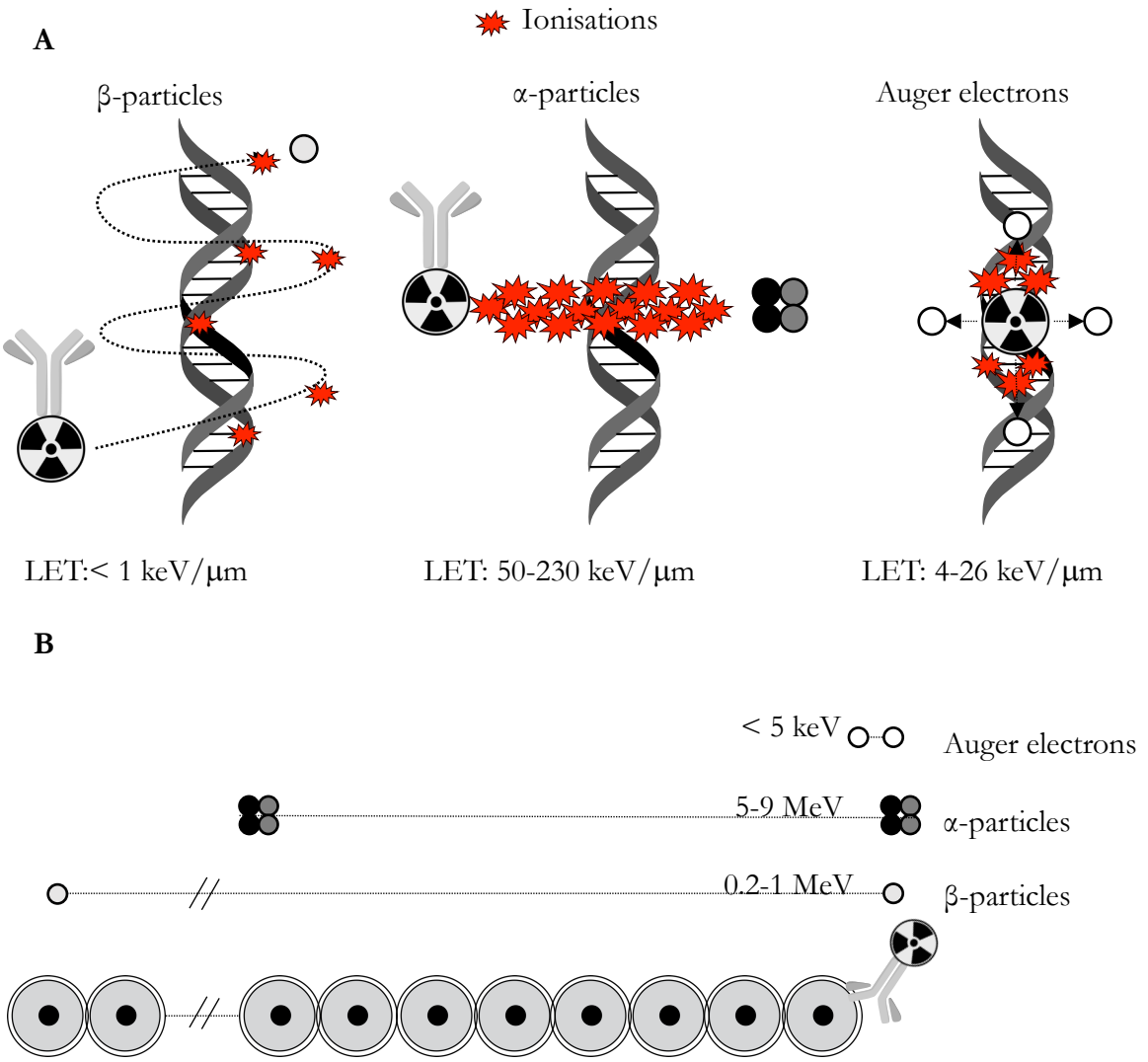


Figure 1.4 Radionuclide properties. A) β-emitting radionuclides produce sparsely ionising radiation along a bent track that causes readily repairable damage. α-Particles on the other hand, cause dense ionisations and complex damage along a linear track. Auger electron-emitting radionuclides cause short-range complex ionisations by release of an electron cascade but require proximity to the DNA. B) The track path-length of Auger electrons (< 0.5 µm), α-particles (10 cell diameters), and β-particles (up to 100 cell diameters) (Pouget et al., 2011).

1.3.2 Nuclear targeting with TRT

The principal target for particulate ionising radiation is nuclear DNA (Bavelaar et al., 2018). Irradiation can damage the DNA directly via one-electron oxidation reactions, or indirectly via the formation of ROS, such as superoxide radicals (O_2^-) and hydrogen peroxide (H_2O_2), that form the precursors of harmful hydroxyl radicals (·OH) (Pouget et al., 2015). These reactions

can lead to single-strand and double-strand DNA breaks (SSBs and DSBs), as well as DNA crosslinks and base damage. If this damage goes unrepaired, cell death by mitotic catastrophe or apoptosis is triggered (Pouget et al., 2015). For this reason, cancer-specific nuclear targeting is of interest to the research community to exploit the optimal effect of TRT. Various investigators have established strategies to bring radionuclides into the close vicinity of cancer cell DNA for Auger electron therapy, including via direct targeting of the DNA (Imstepf et al., 2015; Kotzerke et al., 2014), via sex steroid receptors (androgen, oestrogen) targeting (DeSombre et al., 1992; Kortylewicz et al., 2012), and via the targeting of nuclear trafficking cell surface receptors (EGFR, HER2) (Cai et al., 2016; Cornelissen et al., 2009a). Furthermore, subnuclear targeting has been achieved by binding of nuclear proteins such as γH2AX and telomerase (Cornelissen, 2014; Cornelissen et al., 2012; Waghorn et al., 2017).

1.3.3 hTR targeting with TRT

Here, we explore TRT nuclear targeting of hTR by using an Indium-111 (^{111}In)-labelled antisense oligonucleotide. ^{111}In is a commonly used Auger electron-emitter with a physical half-life of 67.32 h, that decays by electron capture to Cadmium-111 (^{111}Cd) (Cornelissen and Vallis, 2010). This half-life is sufficiently long for therapeutic purposes to allow accumulation in the target volume, but short enough to have decayed before non-beneficial long-term radiation dose effects occur (Pratt and Evan, 2007). The decay of ^{111}In results in a high yield of Auger electrons (14.7), as well as in photon emissions that can be imaged by SPECT.

The hTR-targeting antisense oligonucleotide used, was previously developed by Herbert et al. (1999), who showed that it inhibited telomerase enzyme activity in a dose-dependent and sequence-specific manner. Jackson et al. (2018) modified this sequence with a 5'end amino-linker to facilitate conjugation to DTPA, a metal chelator that is able to bind ^{111}In. The researchers found that this modification did not reduce the affinity for the hTR template. Furthermore, the radiolabelled oligonucleotide reduced the clonogenic survival of telomerase-

expressing cancer cells in a dose-dependent way when transfected, which was accompanied by upregulation of the DNA damage marker γH2AX. Confocal microscopy analysis revealed that the Cy3-labelled oligonucleotide localised in close proximity to nuclear Cajal bodies in telomerase-positive cells and were longer retained than scramble sequence oligonucleotides. This study indicated that radiolabelled oligonucleotides that specifically target the hTR have combined therapeutic activity through potent hTR inhibition and radiation-induced DNA damage induction, which impacts cell survival in telomerase-expressing cancer cells. However, the application of this novel radiopharmaceutical remains limited unless the problems of instability *in vivo* and the need to cross cellular membranes can be addressed (Jackson et al., 2018). These barriers are a common challenge for therapeutic oligonucleotides, and many strategies have been developed to address these issues.

1.4 Delivery of radiolabelled oligonucleotides

1.4.1 Barriers for oligonucleotide delivery

The main challenge for nucleic acid-based cancer therapy is the delivery of the drug to the target organelles of tumour cells (Juliano, 2016). This problem can be broken up into two distinct issues: The first is to target the oligonucleotide to the tumour whilst minimising normal tissue exposure. These tissue barriers include the vascular endothelial system, the reticuloendothelial system (RES), and renal excretion. The second issue is the delivery of the oligonucleotide to the correct subcellular structure, in this case the nucleus, which includes barriers such as the cellular, endosomal and nuclear membranes. Strategies to address barriers involve either chemical modification and conjugation of the oligonucleotide, or incorporation into some form of nanocarrier (Juliano, 2016). In this DPhil thesis, the focus is on nanoparticulate solutions for oligonucleotide delivery.

1.4.2 Gold nanoparticles

Nanosized drug delivery vehicles have provided a novel platform for experimental target-specific delivery (Ghosh et al., 2008). Over the past two decades, various nanocarriers have been developed, such as dendrimers (Paleos et al., 2004), polymers (Xu et al., 2007), liposomes (Kisak et al., 2003), nanotubes (Wu et al., 2005), and nanorods (Salem et al., 2003). Gold nanoparticles (AuNP) have been established as an attractive drug delivery candidate for various payloads. These payloads include oligonucleotides, small molecules, peptides, proteins and antibodies (Su et al., 2013). AuNP exploit unique physical-chemical properties for transport of pharmaceutics. In the first place, the gold core is biologically inert and non-toxic. Furthermore, AuNPs can be produced in a scalable fashion from 1-150 nm with low size dispersity. Lastly, the surface can be decorated with multiple moieties, allowing the design of nanoparticles with a ligand shell of targeting agents, cell-penetrating peptides (CPPs) or oligonucleotides (Ghosh et al., 2008). These properties give rise to a set of positive attributes for AuNP-adsorbed molecules, including improved cellular uptake, increased *in vivo* stability and circulation half-life, and the potential of physical and biological targeting. Furthermore, AuNPs can act as 'drug reservoirs' for controlled and sustained release of bioactive compounds (Ghosh et al., 2008).

1.4.3 Gold nanoparticles for the delivery of oligonucleotides

Over the past twenty years, many groups have synthesised, characterised and tested oligonucleotide-functionalised AuNP constructs (ON-AuNP) (Mirkin et al., 1996). This class type of nanoparticles is comprised of an AuNP core that is decorated with a dense shell of thiol-modified oligonucleotides (Giljohann et al., 2010). ON-AuNP have favourable properties as a result of surface interactions, and these properties have been used for gene silencing (Rosi et al., 2006), enzyme-free diagnostic assays (Nam et al., 2003) and programmable crystallisation (Nykypanchuk et al., 2008). Indeed, the binding, catalytic and optical properties of ON-AuNPs have been applied for various electronic (Park et al., 2002), scanometric (Taton et al., 2000),

colorimetric (Liu and Lu, 2003) and Raman-based (Cao et al., 2002) detection approaches, with some having recently been commercialised (Taton et al., 2000).

An unusual property of ON-AuNP is their capacity to internalise into various cell types (Giljohann et al., 2010). This high uptake was not predicted at first, since ON-AuNP have a polyanionic ligand shell, and typical oligonucleotide internalisation required the presence of positively charged compounds. Despite these predictions, it has been demonstrated that ON-AuNP is taken up in high numbers when added to cell media in more than 30 cell lines (Giljohann et al., 2010). Although the number of internalised nanoconstructs varies as a function of concentration, construct size, construct charge, incubation time and cell type, uptake has been found to be at least an order of magnitude higher than for free oligonucleotides (Rosi et al., 2006). The mechanism of cellular uptake is a topic of great interest and appears to dependent on the physical characteristics of specific constructs. It is highly likely that multiple pathways play a role, which will be discussed in further detail in Chapter 4.

Besides the effect on uptake, oligonucleotide functionalisation has a profound effect on the ability to bind complementary nucleic acids (Jin et al., 2003). Interestingly, surface decoration results in an increased affinity towards the target, which may be as much as two orders of magnitude (Giljohann et al., 2010). This observation is explained via the thermodynamic model that attributes the rapid hybridisation of complementary strands to cooperative process that originates from two main factors: the presence of various DNA linkers between each pair of AuNP and a decrease in melting temperature as oligonucleotide sequences dissociate due to a reduction in local salt concentration (Jin et al., 2003). Therefore, the high local concentration of oligonucleotides on the AuNP surface results in a higher affinity. In the context of *in vitro* and *in vivo* therapeutics, it has been suggested by researchers that this effect would result in greater intracellular binding, thereby increasing the therapeutic effectiveness (Rosi et al., 2006).

Nucleic acid-based therapeutics are often hampered by enzymatic hydrolysis *in vivo*, resulting in inactive compounds (Giljohann et al., 2010; Cazenave et al., 1987). Several studies have demonstrated that oligonucleotide decoration of AuNP results in resistance to enzymatic degradation by DNase I and similar proteins (Rosi et al., 2006). The enhanced stability can be explained by steric hindrance as a result of dense oligonucleotide packing, resulting in inaccessibility of oligonucleotides, and inactivation of the nuclease enzyme due to high local Na^+ ion concentrations (Seferos et al., 2009). Therefore, ON-AuNP constructs have a higher *in vivo* stability than free oligonucleotides, rendering them potentially suitable for therapy.

The ability to translocate cargo over cell membranes, improved binding affinity and resistance to degradation have led to an enormous interest in the application of ON-AuNPs in cancer biology. It is frequently described as an excellent tool for antisense gene control by developing complementary ON-AuNP constructs for target mRNA to prevent protein translation (Rosi et al., 2006). Similarly, silencing RNA (siRNA) decorated AuNP have been used to knock down gene expression (Giljohann et al., 2009). Furthermore, it has been used for intracellular detection of RNA via quenchable complementary strands that release a fluorescent signal upon binding *in vitro* (Seferos et al., 2007).

Based on these results, it was hypothesised that AuNP may form an excellent platform for the delivery of hTR-targeting ^{111}In-labelled oligonucleotides. However, there is no ready-made AuNP for all purposes. For every biological cancer target and oligonucleotide payload, the carrier should be optimised (Dykman and Khlebtsov, 2014). For this reason, multiple strategies were explored, including the use of different sized AuNP, and the addition of CPPs to the ligand shell.

1.4.4 Gold nanoparticles and cell-penetrating peptides

The highest cellular uptake is found for AuNP with a positively charged ligand shell. AuNP complexes are generally negatively charged, and cellular entry is therefore aided by the

adsorption of a positively charged CPP/nuclear localisation sequence (NLS) (Dykman and Khlebtsov, 2014). CPPs are short peptides that generally contain domains of less than 20 amino acids, and are highly charged due to the basic residues lysine and arginine (Torchilin, 2008). CPPs can be categorised in three classes: protein-derived, model, and designed peptides. Protein-derived CPPs are small domains that contain the effective translocating group of proteins, and are therefore also coined protein transduction domains (PTDs) (Torchilin, 2008). Examples of such PTDs are TAT (48-60), which is originally derived from the 86-mer Tat protein (Vivès et al., 1997), and penetratin (43-58), which is derived from the homeodomain of Drosophila Antennapedia (Derossi et al., 1994). Model CPPs are peptides that mimic the properties of known CPPs, such as the model amphipathic peptide (MAP) (Oehlke et al., 1998). Lastly, designed CPPs involve chimeric peptides, that are synthesised by hydrophilic and hydrophobic domain fusion from different sources, such as transportan, which is a fusion of galanin and mastoparan (Pooga et al., 1998).

Investigators have found several translocation mechanisms for CPPs to facilitate membrane traversal, including clathrin-mediated endocytosis, lipid raft-mediated caveolae endocytosis, and macropinocytosis (Torchilin, 2008). Clathrin-mediated endocytosis involves clathrin-coated membrane pit formation that separate from the cell membrane by forming vesicles that can be processed. Several studies have shown this mechanism for Tat, including Console et al. (2003). In contrast, Fittipaldi et al. (2003) found that internalisation was caveolae-mediated and clathrin-independent. Caveolae-mediated uptake encompasses flask-like uncoated invagination formation of roughly 50-70 nm, which are primarily composed of lipid rafts (Torchilin, 2008). Lastly, a non-specific form of cellular uptake, macropinocytosis, was suggested, which involves the formation of large vesicles, macropinosomes, that are made from actin filaments (Kaplan et al., 2005).

A frequently used CPP/NLS for AuNP delivery is Tat, a short arginine-rich peptide that is derived from the transcriptional activator protein encoded by human immunodeficiency virus 1 (Torchilin, 2008). To further facilitate cellular and nuclear entry, Tat is conjugated to constructs studied in this thesis.

1.5 Aims of the study

The primary aim of this DPhil thesis is the synthesis and characterisation of AuNPs functionalised with ^{111}In-labelled hTR-targeting oligonucleotides with and without the CPP Tat for the treatment of telomerase-positive cancer cells. The potential of such treatment may provide advantages for the treatment and diagnosis of telomerase-positive tumours, which account for 80-90% of human malignancies. This aim is addressed by investigating the following three aspects:

- Chapter 3: The synthesis and characterisation of ^{111}In-, Cy3, or Cy5-labelled anti-hTR oligonucleotide-decorated AuNP.
- Chapter 4: The *in vitro* evaluation of ^{111}In- or Cy3-labelled anti-hTR oligonucleotide-decorated AuNP.
- Chapter 5: The *in vivo* assessment of ^{111}In- or Cy5-labelled anti-hTR oligonucleotide-decorated AuNP with and without ultrasound-activatable cavitation agents.

CHAPTER 2. MATERIALS AND METHODS

2.1 Tissue culture

The melanoma-derived cell line MDA-MB-435 and the osteosarcoma-derived cell line U20S were used for cell studies. Cell lines were obtained from the American Type Tissue Culture Collection. Cells were kept in Dulbecco's Modified Eagle's Medium (DMEM; Sigma-Aldrich #D5796) with 10% foetal bovine serum (FCS; Gibco#10270) and 1% penicillin/streptomycin/glutamate (PSG; Sigma-Aldrich #G1146). Cells were regularly passaged by using 0.05% trypsin-EDTA (Gibson #25300-054). Cells were checked monthly for mycoplasma contamination (MycoAlert testing kit; Lonza#LT07).

2.2 Synthesis

2.2.1 Oligonucleotides

High-performance liquid chromatography (HPLC) - purified 2' OMeRNA with hTR complementary (Match) and random (Scramble) oligonucleotide sequences with 5'-amino linkers and 3'-thiols were purchased from Sigma-Aldrich. The following sequences were used:

Match: 5'-CAGUUAGGGUUAG-3'

Scramble: 5'-GCAGUGUGAUGAU-3'

2.2.2 Gold nanoparticles

15.5 nm AuNPs were synthesised as described previously (Rosi et al., 2006). Briefly, AuNPs were prepared by citrate reduction of hydrogen tetrachloroaurate (III) ($HAuCL_4$) trihydrate (Sigma-Aldrich #G4022). Glassware was cleaned in aqua regia ((hydrochloric acid (HCl); Sigma-Aldrich # 258148 : (Hydrogen nitrate (HNO_3); Sigma-Aldrich #438073) = 3:1)), rinsed with Milli-Q water (18.2 MΩ; Millipore) and oven dried before use. $HAuCl_4$ was dissolved in Milli-Q water (1 mM, 200 mL) and brought to a reflux whilst stirring. Upon reflux, 20 mL 38.8 mM

trisodium citrate ($Na_3C_6H_5O_7$; Sigma-Aldrich #S4641**)** solution was added, which caused a colour shift from pale yellow to deep red. Hereafter, the solution was refluxed for 30 minutes (min), and subsequently cooled down to room temperature. The AuNP solution was transferred to a clean glass container and stored at 4 °C.

2.4 nm AuNP were synthesised as described previously (Kumar et al., 2013). In short, 0.5 mL of 1 M sodium hydroxide (NaOH; Sigma-Aldrich #221465) and 1 mL of tetrakis (hydroxymethyl) phosphonium chloride solution (THPC; Sigma-Aldrich #404861) (12 µL of 80% THPC in water to 1 mL of Milli-Q water) was added to 45 mL Milli-Q water and stirred vigorously for 5 min at room temperature. Subsequently, 2 mL of 25 mM $HAuCl_4$ was rapidly added to the solution. Under rapid stirring, the suspension changed colour from yellow to dark brown. The mixture was stirred for another 15 min and cooled to room temperature. The AuNP solution was transferred to a clean glass container and stored at 4 °C.

The concentration and quality of the solutions were determined by spectrophotometer (NanoDrop ND-1000) via the Beer-Lambert Law ($A= \varepsilon bc$, where ε is the molar extinction coefficient, b is the optical path length and c is the concentration). Absorbance was measured at wavelength λ = 450 nm. Molar extinction coefficients were obtained from Haiss et al. (2007).

The AuNP size and distribution were determined by dynamic light scattering (DLS) with a Nano series Zetasizer instrument (Malvern Instruments). Samples were diluted to a concentration of 5 nM in Milli-Q water and transferred to disposable plastic cuvettes (Malvern Instruments #ZEN0118) at room temperature. The samples were measured in triplicate and the hydrodynamic radius was calculated by the software ZS Xplorer using Stoke-Einstein's relation for the Brownian motion of particles.

Particle size and morphology were further analysed using a transmission electron microscopy (TEM). Samples were lyophilized for 24 hours (h) on 150 mesh TEM grids (Agar Scientific # AGG201N) and images were acquired by a Fei Tecnai 12 TE microscope and imaged with a 16

Megapixel Gatan OneView camera with CMOS sensors. Images were obtained with a 1 second (s) exposure time, and a pixel saturation of 5000-6000. Analysis was performed with ImageJ software.

2.2.3 Fluorophore-labelling of oligonucleotides

Oligonucleotides were dissolved in sodium hydrogen carbonate ($NaHCO_3$; 0.1 M pH 8.3; Sigma-Aldrich #S5761) to a concentration of 100 μM. Cy3-monoreactive dye (GE Healthcare #PA23001) or Cy5-monoreactive dye (GE Healthcare #PA25001) were reconstituted in 20 μL dimethyl sulfoxide (DMSO; Sigma-Aldrich #276855) and subsequently added to the oligonucleotide solution. The incubation lasted at least 120 min at room temperature under periodic mixing. Using P4 (BioRad #150-4120) size exclusion chromatography (SEC), reaction products were separated into 50 μL phosphate-buffered saline (PBS) fractions. Fractions were analysed by spectrophotometer at wavelength 260 (oligonucleotides), 550 (Cy3) and 649 (Cy5) nm. Cy3- and Cy5-conjugated oligonucleotides were stored at -20 °C.

2.2.4 Radiolabelling of oligonucleotides

Oligonucleotides were dissolved in $NaHCO_3$ buffer (0.1 M, pH8.3) to a concentration of 100 μM. Diethylenetriaminepentaacetic dianhydride (DTPA; Sigma-Aldrich #284025-1G) was dissolved in DMSO and added to the oligonucleotide solution in a ten-fold molar excess. The reaction was incubated for at least 60 min. Reaction products were separated by SEC with P4-Biogel into 50 μL sodium citrate ($NaH_2C_6H_5O_7$; 0.1 M pH5; Sigma-Aldrich #71498) fractions. Concentration was determined by spectrophotometer at wavelength 260 nm. DTPA-labelled oligonucleotides were stored at -20 °C. Analytical radiolabelling was performed in sodium citrate (0.1 M, pH5.0) by incubating DTPA-labelled oligonucleotides with ^{111}In chloride ($^{111}InCl_3$; Curium Pharma #DRN4901) at a specific activity of 0.8 MBq/μg. Radiolabelling efficiency was determined using a radio-thin layer chromatography (TLC) Imaging Scanner (Bioscan #AR-2000).

2.2.5 ON-AuNP conjugates

ON-AuNP and ON-AuNP-Tat conjugates were synthesised as described previously (Rosi et al., 2006). For ON-AuNP, oligonucleotides (final concentration 3 μM) were added to a 15 nM solution of 15.5 nm AuNPs. For ON-AuNP-Tat, polyethylene glycol methyl ether thiol (PEG-SH; MW: 800; Sigma-Aldrich #729108) (final concentration 45 μM) was dissolved in a 15 nM AuNP solution for 20 min prior to the addition of oligonucleotides (final concentration 1.5 μM). After a 10-min incubation with oligonucleotides, Tat (Sequence: GRKKRRQRRRPQGYGCG; Cambridge Peptides; end concentration 1.5 μM) was added to the solution. Both ON-AuNP and ON-AuNP-Tat were subsequently incubated overnight. On day 2, both suspensions were salt-aged over an 8 h period to achieve a final sodium chloride (NaCl; Sigma-Aldrich #S7653) concentration of 0.3 M. The mixture was shaken overnight. The functionalised AuNP were purified by centrifugation (20000 x *g*; 40 min; 4 °C, three times) (Eppendorf #5417R), after which the pellet was resuspended in Milli-Q water. New constructs were prepared prior to every repeat experiment. Particle size and morphology was determined as described in section 2.2.3.

The number of copies of the oligonucleotide per particle was determined by ^{111}In-labelling the oligonucleotide with a known ^{111}In to oligonucleotide ratio. Subsequently, constructs were synthesised as described above. The number of oligonucleotides per pellet was calculated by comparing the ^{111}In counts per min (CPM) of the resuspended pellet with a known standard using a Wizard3" automatic gamma-counter (Perkin-Elmer 2480). All treatment concentrations refer to the concentration of oligonucleotides.

AuNP concentration and quality was determined by ultraviolet-visible (UV-Vis) spectrometry as described above. Stability was monitored over time at 4 and 37 °C and analysed by DLS as described in section 2.2.2.

2.2.6 ON-AuNP radiolabelling

AuNP constructs were reconstituted in sodium citrate (0.1 M, pH5.0) prior to radiolabelling. Subsequently, $^{111}InCl_3$ at the desired specific activity was added and incubated overnight. The next day, radiolabelling was confirmed with TLC, and AuNP were purified by centrifugation (20000 x *g*; 40 min).

2.3 Telomeric repeat amplification protocol

2.3.1 Cell lysate extraction

Cells were harvested with 0.05% trypsin-EDTA and counted using a haemocytometer. Cells were centrifuged (160 x *g*; 10 min; 4 °C), washed with PBS, and re-pelleted. 1% CHAPS lysis buffer (EMD-Millipore #S7707) was added (200 µL/10^6 cells) and the cell pellets were incubated on ice for 30 min. Lysates were subsequently centrifuged (12000 x g; 20 min; 4 °C) to remove insoluble material. The protein concentration of lysates was determined using the Pierce bicinchoninic acid (BCA) Protein Assay kit (Thermo Scientific #23225), according to the manufacturer's instructions. The optical density of the lysate was analysed at 562 nm in a fluorescence plate reader (Tecan Infinite M2000). Lysates were aliquoted, snap frozen on dry ice, and stored at -80 °C.

2.3.2 TRAPeze XL

The TRAPeze XL Telomerase Detection kit (EMD-Millipore #S7707) was set up according to the manufacturer's protocol, with the following alterations to the polymerase chain reaction (PCR) protocol: the first cycle was set to 30 °C for 30 min, followed by 36 cycles of 94 °C for 30 s; 53.5 °C for 30 s; 72 °C for 60 s and a final extension of 72 °C for 3 min. The reaction mix contained 2 Jumpstart-*Taq* polymerase (Sigma-Aldrich #D9307) units, 2 µL of cell lysate with a concentration of 100 ng/µL, 5x Reaction buffer, nuclease-free water, and inhibitor/control up to a total volume of 55.5 µL. After the PCR, samples were centrifuged (20000 x *g*; 30 min; 4 °C) to remove AuNPs. 40 µL of the supernatant was subsequently mixed with 160 µL of the

read buffer (Tris-HCl pH 7.4 (10 mM; Sigma-Aldrich #T5941), NaCl (50 mM; Sigma-Aldrich #S7653), Magnesium chloride ($MgCl_2$; 2 mM; Sigma-Aldrich #M1028) in a 96-well flat black plate (Costar #3915) and read with a fluorescence plate reader. Telomerase activity was measured by fluorescein and sulforhodamine emission (485/535 nm and 585/620 nm). Telomerase activity was normalised against an untreated control. Results were controlled for non-specific interactions by the use of the control template TSR8. TSR8 is an oligonucleotide with an identical sequence to the primer extended with 8 telomeric repeats, allowing the efficiency of the reaction to be tested. Experiments were performed in duplicate.

2.4 Internalisation and fractionation assays

For internalisation assays, cells were seeded in a 12-well plate (Greiner bio-one #665180) at 2 x 10^5 cells/well overnight. Cells were incubated with the compound under study for 24 h. Following incubation, the medium was aspirated and retained. Cells were then washed with 500 µL and 250 µL PBS, and the washes combined with the medium to constitute the free-fraction. Free-fractions were diluted 10-fold to facilitate counting in a gamma-counter. Cell membranes were washed using 500 µL glycine (0.1 M; pH 2.5; Sigma-Aldrich #G8898) at 4 °C for 6 min and re-washed with 500 µL PBS. NaOH (0.1 M; 250 µL; Sigma-Aldrich #72068) was added and plates incubated for 20 min at room temperature to lyse the cells. The internalised fraction was then collected and combined with the two PBS washes of 500 µL and 250 µL. Fractions were counted in a Wizard gamma-counter.

The commercially available Nuclei EZ Prep Nuclei Isolation kit (Sigma-Aldrich #NUC101-1KT) was used to determine the subcellular distribution of AuNP constructs. Nuclei were isolated according to the manufacturer's protocol with minor adjustments. In brief, 1 x 10^5 cells/well were plated in a 24-well plate overnight and treated for the indicated time. Following incubation, the medium was aspirated and retained (container 1). Cells were harvested using 0.05% trypsin-EDTA (100 µL), mixed with 400 µL PBS (4 °C), and transferred to a 1.5 mL vial.

The vials were centrifuged in a microcentrifuge for 5 min at 500 x g, after which the supernatant was collected and combined with the retained medium giving the free fraction (container 1). Nuclei EZ lysis buffer (200 μL) was added to the vial, and the mixture was vortexed vigorously. The vial was spun down for 5 min at 500 x g and the cytosolic supernatant fraction was collected and transferred to container 2. The pellet was again suspended in 200 μL Nuclei EZ lysis buffer, and the previous step was repeated to purify the nuclear pellet. After transfer of the supernatant to container 2, the nuclear fraction was mixed with 1 mL PBS and transferred to container 3. All fractions were counted in a Wizard gamma-counter.

2.5 Confocal microscopy

2.5.1 Subcellular distribution studies

Cells (2 x 10^5/well) were seeded in an 8-well chamber slide (Thermo Scientific #177402) and incubated overnight. Cells were incubated with 500 nM Cy3-Match-AuNP or Cy3-Match-AuNP-Tat for the indicated time in 200 μL media. After incubation, cells were washed in PBS before fixation in 200 μL of 4% formaldehyde (Sigma-Aldrich #252549) for 10 min at room temperature. Before removal of the media-chamber, cells were washed three times with PBS. One drop of Vectashield (Vector #H-1200) containing 4', 6-diamidino-2-phenylindole (DAPI) was added to each well, after which samples were mounted with a 24 x 24 mm coverslip (VWR International #6310127). Images were obtained using a laser-scanning Leica confocal microscope (TCS SP8). Confocal planes were imaged using line-scanned consecutive acquisition channels through a 63x/1.40 oil immersion lens, with a pixel dwell time of 0.64 μs, and pin-hole of 1 Airy unit, with the following settings: DAPI - illumination 405 nm. Cy3 - illumination, 543 nm, 563-660 detector.

2.5.2 γH2AX studies

Cells (2 x 10^5/well) were seeded in an 8-well chamber slide (Thermo Scientific #177402) and incubated overnight. Cells were treated with 210 nM ^{111}In-labelled ON-AuNP-Tat (18

MBq/nmol) or media for 24 h in 200 μL media. The positive control consisted of cells exposed to external beam irradiation (4 Gy). After incubation, cells were washed twice in PBS, fixed in paraformaldehyde, permeabilised with 1% Triton X-100 in PBS and blocked for 1 h at 37 °C with 2% BSA in PBS (Cornelissen et al., 2013). Fixed cells were incubated with anti-γH2AX primary antibody (JBW301; Millipore; 1:800 dilution) for 1 hour at 37°C, washed 3 times, and exposed to AF488-labelled goat-anti-mouse antibody (Invitrogen; 1:250 dilution) for 1 h at 37 °C. Cells were washed three times with PBS before removal of the media-chamber. One drop of DAPI was added to each well, after which samples were mounted with a 24 x 24 mm coverslip (VWR International #6310127). Images were obtained using a laser-scanning Leica confocal microscope (TCS SP8). Confocal planes were imaged using line-scanned consecutive acquisition channels through a 63x/1.40 oil immersion lens. The number of γH2AX foci and nuclear surface area (NSA) were automatically calculated with ImageJ software. All data is expressed as foci/NSA.

2.6 Transmission electron microscopy

MDA-MB-435 cells were plated on to Thermanox plastic coverslips 13 mm-diameter (Thermo Scientific, #174950) in 6-well plates (Greiner bio-one #657160) at a seeding density of 8 x 10^5 cells and left to adhere overnight. Media was refreshed before incubation with 500 nM Match-AuNP or Match-AuNP-Tat. After 24 h, the medium was removed, and cells were washed twice in 1,4-piperazinediethanesulfonic acid buffer (PIPES buffer; 0.1 M; pH 7.2; Sigma-Aldrich # P8203) for 5 min. Cells were then fixed in pre-warmed (37 °C) primary fixative (2.5% glutaraldehyde (Sigma-Aldrich #G5882) and 2% paraformaldehyde (Fisher Scientific #1044336) in 0.1 M PIPES for 1 h at room temperature. The primary fixative was subsequently aspirated, and cells were washed in 0.1 M PIPES (four changes) for 1 h. Subsequently, coverslips were transferred to a 24-well plate and fixed in 1% Osmium tetroxide (OsO_4; Sigma-Aldrich #201030) in 0.1 M PIPES for 1 h at 4 °C. Coverslips were washed three times in Milli-Q water

for 10 min per wash, before tertiary fixation in 0.5% aqueous uranyl acetate (Agar Scientific #R1260A) overnight at 4 °C in the dark. The next day, cells were washed twice in Milli-Q water for 5 min prior to dehydration. The dehydration step occurred in 30%, 50%, 70%, 80%, 90% and 95% ethanol (Sigma-Aldrich #459844) in ascending order for 10 min per concentration prior to the final incubation with 100 % dry ethanol for 30 min (three ethanol changes). Cells were subsequently set in Agar100 (Agar Scientific #R1140) resin by incubating at room temperature for 1 h at 3:1 ratio (100% dry ethanol : Agar100), 2 h at a 1:1, and 1 h for 1:3, after which the cells were exposed to 100% Agar100 with benzyl dimethylamine (BDMA; Agar Scientific #R1140; 300 μL for 10 mL of resin) overnight (one replacement step after 2 h). The following day, the resin was replaced, and cells were incubated for another 2 h prior to oven polymerisation. Coverslips were removed from the 24-well plate, placed in flat embedding capsules (Electron Microscopy Sciences #70021) that were filled with fresh Agar100/BDMA, and put in a polymerisation oven for 2 h at 100 °C. After polymerisation, capsules were dropped in liquid nitrogen for 30 s, and the capsule was removed using a razor blade (Fisher Scientific #11904325) and capsule splitter (TAAB #C065). Blocks were sectioned on an ultramicrotome (Leica EM UC7) by Dr Errin Johnson (Sir William Dunn School of Pathology, University of Oxford), after which the 90 nm sections were placed on a nickel TEM grid and moved to a petri dish for post staining with lead(II) citrate tribasic trihydrate (Sigma-Aldrich #15326); and uranyl acetate. To avoid carbonisation and precipitate formation, petri dishes were lined with parafilm and NaOH pellets (Sigma-Aldrich #72068). After staining, sections were analysed on a Tecnai 12 TEM and imaged with a 16 Megapixel Gatan OneView camera with CMOS sensors. Images were obtained with a 1 s exposure time, and a pixel saturation of 5000-6000.

2. 7 Clonogenic assay

Cells were seeded in a 96-well plate (Greiner bio-one #662160) at 2 x 10^4 cells/well overnight. Cells were transfected with radiolabelled and non-radiolabelled oligonucleotides, ON-AuNP

and ON-AuNP-Tat (27 MBq/nmol) for 24 h. In the case of experiments designed to test the effect of ON-AuNP constructs on sensitivity to external radiation, cells were irradiated after 24 h of AuNP construct treatment using a Cesium-137 (^{137}Cs)-irradiator (0.662 MeV) to achieve a dose of 2, 4, and 6 Gy, after which the cells were left for 1 h.

After incubation, cells were harvested following washing in PBS and the addition of 50 μL trypsin-EDTA. Harvested cells were counted before plating in 6-well plates (Greiner bio-one #657160) at a density sufficient to give > 75 colonies for counting. Untreated (control) cells were typically seeded at 600 cells/well. Colonies were grown for > 7 days, washed in PBS and stained with 1% methylene blue (Alfa Aesar #A18174) in 50% methanol (Fisher Scientific #M/4000/ PC17). Excess stain was washed-off with water. Colonies containing > 50 cells were counted. The surviving fraction (SF) was calculated using the plating efficiency (PE) of untreated cells and the dose (D). The Mean Inactivation Dose (MID), defined as $\mathrm{MID}=\int_0^\infty \mathrm{SF}(\mathrm{D})\mathrm{dD}$, was calculated for each curve (Fertil et al., 1984; Subiel et al., 2016). MIDs were compared using One-Way ANOVA with Bonferroni correction for multiple comparison. For radiosensitivity assays, a sensitiser enhancement ratio (SER) was calculated by dividing the MID of the non-AuNP-treated group by the MID of the AuNP-treated group ($\mathrm{SER}=\frac{\mathrm{MID_{AuNP}}}{\mathrm{MID_{No\ AuNP}}}$).

2.8 *In vitro* model for ultrasound-mediated AuNP delivery

The effect of ultrasound-activatable cavitation agents, such as SonoVue (Bracco) and SonoTran nanocups (OxSonics), on the extravasation of AuNP constructs was tested *in vitro* in collaboration with Dr Harriet Lea-Banks (Oxford Institute of Biomedical Engineering (IBME)). Ultrapure agarose powder (Sigma-Aldrich #A2576) was dissolved in degassed Milli-Q water (1 wt%) and boiled for 30 min, after which it was allowed to cool to 40 °C. Agarose was poured into the MCcell vessel phantom (IBME) (Fig. 2.1 A) and cooled to 4 °C overnight. The next day, the steel channel-forming rods were removed, and the channels were flushed with Milli-Q

water. The phantom inlet and outlet were coupled to Tygon tubing. Subsequently, the phantom was suspended in a water bath at 37 °C. A HIFU transducer (Sonic Concepts H107D-013) was aligned to the phantom and its position in each channel was confirmed with a B-Mode scanner (Philips HD7). Cy5-ON-AuNP-Tat (5 nM) with and without nanocups (1 mg/mL) or SonoVue (2.25 μg/mL) were injected into the tube system at a flow rate of 300 μL min^{-1} before exposure to ultrasound (frequency: 0.5 MHz, pressure: 1.5 MPa, 2500 cycles, 200 bursts, 2.5% duty cycle) via an amplifier (Electronics and Innovation USAA300 (019667)). After ultrasound exposure, the channels were flushed, and the phantom was removed from the water bath (IBME). The agarose gel was subsequently removed from the phantom and the gel was sliced for an axial and cross-sectional view (Fig. 2.1 B). The slices were placed on a glass plate for analysis by confocal microscopy Zeiss 780; objective: EC Plan-Neofluar10x/0.30 M27, Filters: Ch1: 642-740, Lasers: 488nm, 633nm). A Matlab script was used to map fluorescent pixels across the image and calculate the total fluorescent surface and peak penetration depth.

2.9 Animal studies

All animal procedures were carried out in accordance with the UK Animals (Scientific Procedures) Act 1986 and with local ethical committee approval. Single-photon emission computed tomography (SPECT), biodistribution, and *in vivo* imaging system (IVIS) studies were performed using female athymic nude mice (Charles River, UK) bearing MDA-MB-435 xenografts. MDA-MB-435 xenografts were established by subcutaneous (s.c.) injection in the flank of 5-10 million cells in PBS and matrigel (BD Bioscience #354234) in a 1:1 ratio. Imaging was performed when xenografts reached a volume of approximately 500 mm^3. Prior to every treatment, animals were anaesthetised using 2-4% isoflurane gas (Sigma-Aldrich #792632) (0.5 L/min in oxygen) and body temperature was kept at 37 °C throughout imaging sessions.

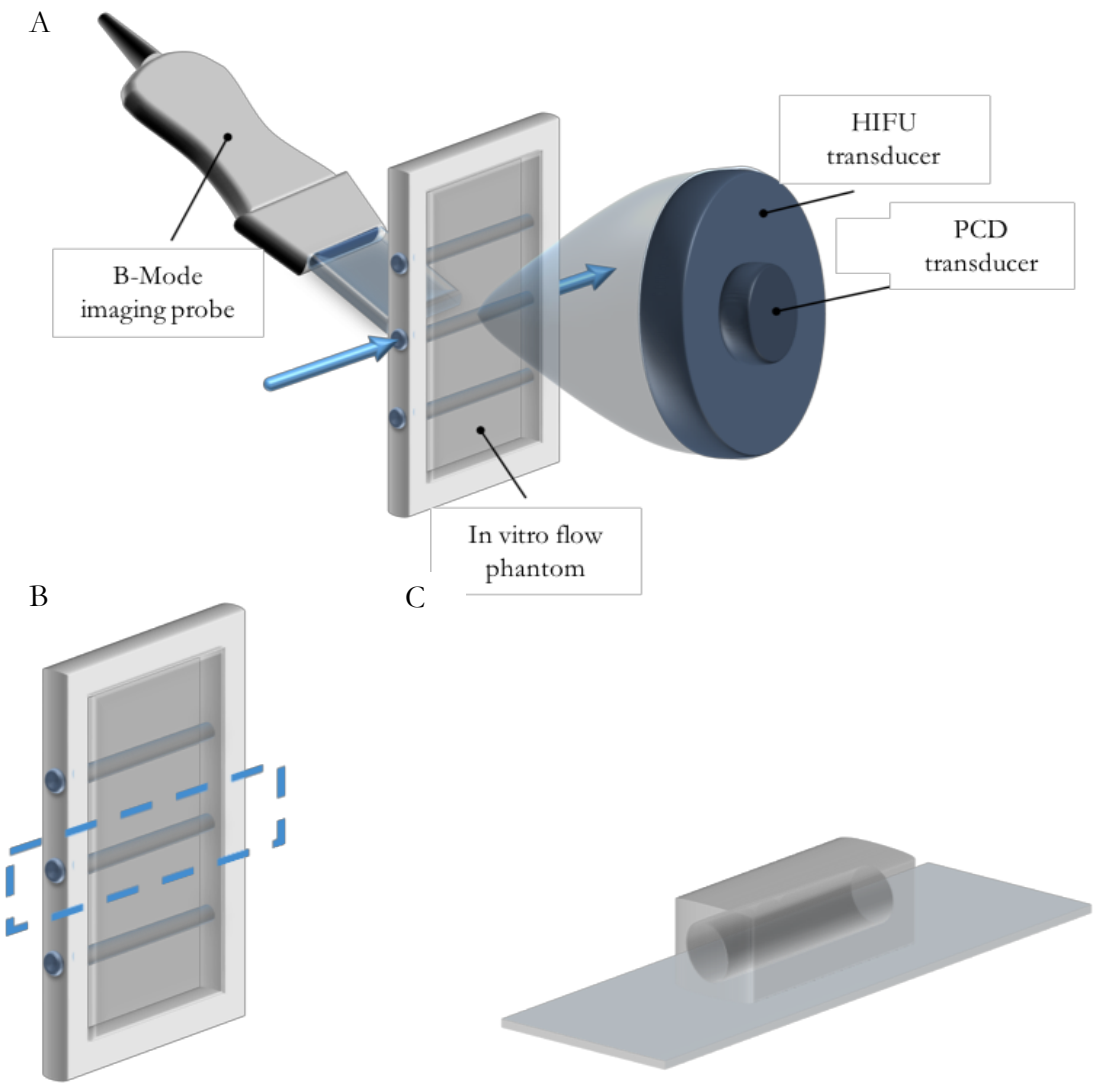


Figure 2.1 Schematic illustration of the *in vitro* ultrasound setup (Image by courtesy of Dr H. Lea-Banks). A) An MCcell agarose phantom model is suspended in a water bath and a HIFU and PCD transducer are aligned with the help of a B-Mode imaging probe. Solutions containing Cy5-Match-AuNP with or without nanocups/SonoVue were injected at 300 µL min-1 through the phantom channel and exposed to ultrasound (frequency: 0.5 MHz, pressure: 1.5 MPa, 2500 cycles, 200 bursts, 2.5% duty cycle). B) The phantom is lifted out of the water bath and individual channels are cut out, and C) placed on a glass slide for analysis by laser-scanning confocal microscopy.

2.9.1 Pharmacokinetics and biodistribution of ^{111}In-ON-AuNP-Tat

For SPECT imaging, athymic nude mice bearing MDA-MB-435 xenografts on the right flank received 2.5 μg oligonucleotide (10 MBq) of ^{111}In-Match-AuNP-Tat (n=3) or ^{111}In-Scramble-AuNP-Tat (n=3) intravenously. Images were acquired 24, 48 and 72 h post-injection using the VECTor^{4}CT (MIlabs), a scanner that provides high resolution (0.25 mm) SPECT images and integrated CT. Whole-body SPECT images were acquired for 30 min per mouse with an ultra-high-resolution rat/mouse 1.8 mm collimator (HE-UHR-RM) (6 time frames, 30 s per bed position, 10 positions). An anatomical reference with a cone beam CT scan (55 kV, 0.19 mA) was performed after the SPECT image acquisition. SPECT images were reconstructed using MiLabs ImageJ software packages. Following the last SPECT imaging session (72 h post-injection), animals were euthanised, and organs were removed and transferred to a pre-weighted counting tube. The tissue-containing tube was weighed again and measured using a gamma-counter. Measurements were decay-corrected to the activity at the time of injection. A calibration curve was generated to convert CPM to the unit for radioactivity (MBq), allowing the calculation of the percentage of the injected dose per gram of tissue (%ID/g).

2.9.2 Ultrasound-mediated tumour delivery of Cy5-Match-AuNP

Optical imaging studies using an IVIS (Xenogen IVIS 100) were conducted to determine the biodistribution of Cy5-Match-AuNP-Tat with and without ultrasound-activated nanocups. Cy5-Match-AuNP-Tat (0.001 – 1 μg/well) in tumour lysate was plated out in a black well plate and measured by plate reader and IVIS to determine the minimal detectable dose. The dose was then confirmed by IVIS imaging of intra-tumoural injections Cy5-Match-AuNP-Tat (0.001 – 1 μg) in athymic nude mice bearing MDA-MB-435 xenografts. The determined dose of 1 μg oligonucleotide of Cy5-Match-AuNP-Tat was used in all subsequent studies.

Two weeks prior to the start of the treatment, mice received a Teklad Global Diet 2019X (Harlan) to reduce fluorescence of the gastro-intestinal tract. Athymic nude mice bearing

bilateral MDA-MB-435 xenografts or Balb-c mice bearing unilateral CT26 xenografts received 1 µg oligonucleotide of Cy5-Match-AuNP-Tat in 100 µL PBS by intravenous (i.v.) injection. For studies with ultrasound, mice were anaesthetised, cannulated, and Cy5-Match-AuNP-Tat was injected, immediately followed by 2 mg nanocups or inactivated nanocups in a total volume of 200 µL. Experimental groups consisted of 3 mice unless otherwise indicated. The ultrasound was set up and delivered by Drs Christophoros Mannaris and Harriet Lea-Banks. Ultrasound was delivered over 10 min directly after injection with a focussed ultrasound (FUS) transducer operating at 0.5 MHz at a pressure not exceeding 1.5 MPa to initiate *in vivo* nanocup cavitation (Fig. 2.2). The installation was set up as reported previously by Bhatnagar et al. (2016). Briefly, a 5 MHz passive cavitation detector (PCD), confocally and co-axially aligned with the FUS transducer, was used to record cavitation-associated acoustic emissions. A degassed water-filled cone was used to transduce the ultrasound signal to the tumour, and the cone was coupled to the tumour with a rubber O-ring filled with coupling gel. Mice were anaesthetised with 2-4%

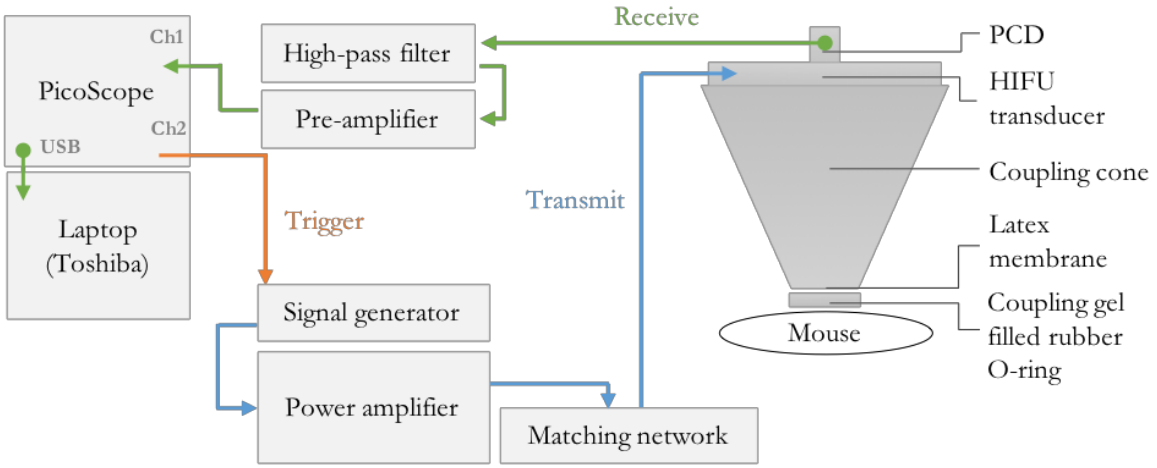


Figure 2.2 Schematic representation of the in vivo ultrasound delivery set-up. A computer-controlled function generator and high-power RF amplifier generated a driving signal for the HIFU transducer via a matching network. The HIFU transducer was connected to the mouse via a coupling cone containing degassed, deionised water that was positioned right above the mouse tumour, and a rubber O-ring filled with coupling gel. Acoustic emissions from the focus were measured by PCD, which was coaxially aligned with the rubber O-ring, cone and HIFU transducer. The signal was conditioned via a high pass filter and a broadband amplifier, after which the signal was recorded by the PicoScope. Image adapted from a schematic by Dr H. Lea-Banks.

isoflurane gas and then imaged using an IVIS camera 0.5 h prior to, directly after and 2.5 hour after the injection of Cy5-labelled AuNP and ultrasound application. Following the last imaging session, mice were euthanised, and organs were harvested. Organs and tumours were homogenised and measured by plate reader.

2.10 Statistical analysis

Data were plotted using GraphPad Prism 6.0. Data points represent mean ± standard deviation, unless otherwise indicated. Dose-response curves were made using non-linear regression, dose vs. normalised response (variable slope). Clonogenic survival was plotted with second order polynomial (quadratic) curve fitting.

CHAPTER 3. SYNTHESIS OF GOLD NANOPARTICLE RADIOPHARMACEUTICALS

3.1 Introduction

This chapter describes the chemical modifications of anti-hTR oligonucleotides (Table 3.1), as well as the synthesis and functionalisation of AuNP constructs. Here, three types of nanoparticles were synthesised (Fig. 3.1):

1. **ON-AuNP**: a 15.5 nm AuNP core with a monofunctional layer of Match or Scramble oligonucleotides (Fig. 3.1 A).
2. **ON-AuNP-Tat**: a 15.5 nm AuNP core with a multifunctional layer of Match or Scramble oligonucleotides, Tat, and PEG800-SH (Fig. 3.1 B).
3. **ON-uAuNP**: a 2.4 nm AuNP core with a monofunctional layer of Match or Scramble oligonucleotides (Fig. 3.1 C).

Oligonucleotides and AuNP constructs were characterised by UV-Vis spectrophotometry, TEM, radio-TLC, and DLS. The AuNP constructs described in this chapter were taken forward for testing in *in vitro* (Chapter 4) and *in vivo* (Chapter 5) systems.

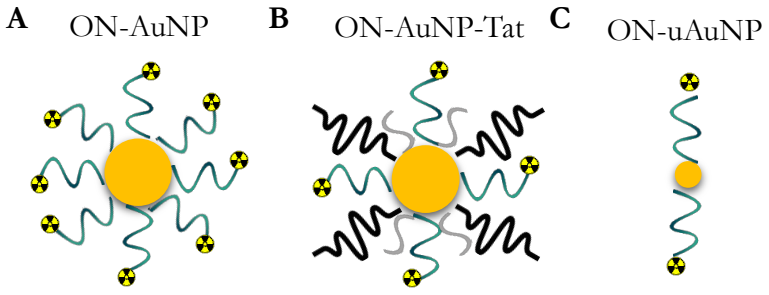


Figure 3.1 AuNP constructs. A) ON-AuNP consists of a 15.5 nm AuNP core with a monofunctional layer of Match/Scramble oligonucleotides. B) ON-AuNP-Tat consists of a 15.5 nm AuNP core with a multifunctional layer of Match/Scramble oligonucleotides, Tat, and PEG800-SH. C) ON-uAuNP consists of a 2.4 nm AuNP core with a monofunctional layer of Match/Scramble oligonucleotides.

3.1.1 Therapeutic oligonucleotides

Therapeutic oligonucleotides for the treatment of cancer have been under development for over 40 years (Khvorova and Watts, 2017). Oligonucleotide therapeutics are a class of drugs consisting of antisense oligonucleotides (ASOs) (Yamamoto et al., 2011), small-interfering RNAs (siRNAs) (Burnett and Rossi, 2012), aptamers (Keefe et al., 2010), microRNAs (Lindow and Kauppinen, 2012), and others (Sullenger and Nair, 2016). The promise of rational drug design for virtually any genetic target, based on sequence-dependent targeting with oligonucleotides, led to the establishment of an entire new field of research. Nonetheless, in the early days, these types of compounds suffered from poor outcomes *in vivo* and in the clinic due to unfavourable substrate availability, cellular uptake, endosomal escape and pharmacokinetics (See Chapter 1.4.1) (Lorenzer et al., 2015). Compounds were rushed into clinical trials with suboptimal chemical characteristics and delivery vehicles, which resulted in the need for very high doses to achieve a limited effect. Recent advances in chemical modifications and delivery strategies have reignited the field and opened up opportunities for novel treatments (Khvorova and Watts, 2017). One of these promising therapeutic oligonucleotides is the hTR inhibitor (Match) described by Herbert et al. (1999) (Table 3.1), which has been modified by Jackson et al. (2018) with a phosphorothioate (PS) backbone and a 2'OMe to improve uptake kinetics.

The PS backbone modification is the most widely used chemical modification to improve stability through resistance to the action of nucleases, cellular uptake and trafficking (Khvorova and Watts, 2017). Dr Mark Jackson, a former member of the Radiotherapeutics and Radioimaging Group at the Oxford Institute for Radiation Oncology, modified the Match and Scramble oligonucleotide sequences with a PS backbone and found that the modification led to

Table 3.1 hTR-targeting oligonucleotide sequences and 2'-O-methyl modifications.

Oligonucleotide	Sequence 5' - 3'	Modification	5'-end	3'-end
Match	CAGUUAGGGUUAG	2'OMeRNA	Amine (AmC6)	Thiol
Scramble	GCAGUGUGAUGAU	2'OMeRNA	Amine (AmC6)	Thiol

a sequence-independent reduction in telomerase activity (Jackson et al., 2018). Therefore, the development of this compound was seized. The second option involved addition of a methyl group to the 2' hydroxyl side of the nucleoside ribose moiety, resulting in a methoxy group (2'OMe). This modification is found in ribosomal RNA (rRNA) and small nuclear RNA (snRNA), and can lead to improved affinity, nuclease resistance and reduced immune stimulation (Khvorova and Watts, 2017). 2'OMe of the compound developed by Herbert et al. was found to inhibit telomerase activity in a sequence-dependent way. For this reason, 2'OMe-modified oligonucleotides were used in all subsequent studies (Table 3.1).

3.1.2 Radiolabelled oligonucleotides

Oligonucleotides can be labelled with metal and non-metal radionuclides for imaging or therapy (Liu et al., 2010). Labelling with a radiometal, such as ^{111}In, requires the covalent attachment of a chelator, a chemical structure that can bind the radionuclide in a claw-like fashion. DTPA, a well-characterised chelator, is an aminopolycarboxylic acid that consists of a diethylenetriamine backbone with five carboxymethyl groups (Ardestani et al., 2010). DTPA is a bifunctional chelator, and can be conjugated to an amine-containing molecule via a ring opening of one of its anhydride groups to create an amide bond linkage (Fig. 3.2) (Hermanson, 2010). Since in this study it was intended to radiolabel oligonucleotides, all were synthesised with 5'-end amino

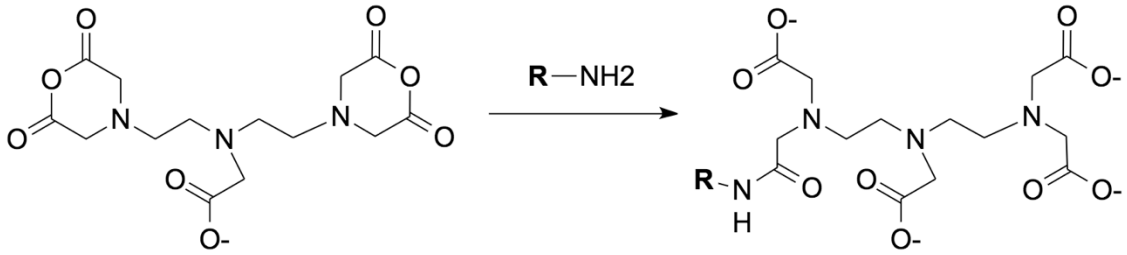


Figure 3.2 DTPA dianhydride conjugation. Amine containing molecules, such as proteins or modified oligonucleotides, can be conjugated to DTPA dianhydride via a ring opening that exposes an anhydride group to form an amide bond linkage.

groups (Table 3.1). Amino groups were attached to a 6-carbon linker to reduce autoradiolysis of the radiolabelled oligonucleotide.

3.1.3 Oligonucleotide-decorated gold nanoparticles

During the past decade, gold nanoparticles (AuNPs) have emerged as an attractive platform for oligonucleotide delivery (Ding et al., 2014). Biological compounds, such as oligonucleotides, can be anchored onto the AuNP surface through a terminal thiol since a strong interaction occurs between sulphur (S) and gold (Au) (Mirkin et al., 1996). This bond has been identified as partially covalent (ca. 35%) and partially electrostatic (ca. 65%) but is commonly referred to as the S-Au covalent bond (Pakiari and Jamshidi, 2010). To facilitate this interaction, all the oligonucleotides for this study were modified with a 3'-end thiol group addition (Table 3.1). As discussed in Chapter 1, AuNP decoration can lead to increased cellular uptake, resistance to endonuclease degradation and improved *in vivo* stability of oligonucleotides. AuNPs can be functionalised with different moieties, including targeting, cytotoxic and cell penetrating molecules. Furthermore, metallic nanoparticles have tuneable size and shape, which can influence cellular uptake, cytotoxicity, and biodistribution (Ding et al., 2014). Since nuclear uptake is restricted to constructs of a maximum diameter of ± 38 nm, constructs below this size are required for the targeting of intranuclear proteins (Eibauer et al., 2015). Therefore, it was considered that 2 and 15 nm AuNPs would provide suitable platforms for the delivery of hTR-targeting, ^{111}In-labelled oligonucleotides.

The type of reducing agent, gold salt to reducing agent ratio, and temperature play a critical role in determining the shape and size of AuNP. For 15 nm AuNP, one of the most commonly used approaches involves sodium citrate reduction, in which citrate acts as loosely bound capping agent that stabilises the AuNP. The group of Chad Mirkin has demonstrated that these citrate-stabilised AuNP can be functionalised with various oligonucleotides and peptides, and

this method was subsequently chosen for synthesis of ON-AuNP and ON-AuNP-Tat (Fig. 3.1) (Mirkin et al., 1996; Giljohann et al., 2007; Patel et al., 2008).

Ultra-small AuNP or nanoclusters have been explored more recently for their different pharmacokinetic and cellular localisation properties (Kumar et al., 2013; Huang et al., 2012b). A quick and versatile synthesis method with Tetrakis as capping agent was developed by Kumar et al. (2013), and was used in this study (Fig. 3.1).

3.1.4 Cell-penetrating peptide – decorated gold nanoparticles

Cellular membranes limit the access of nanoparticles and smaller compounds to subcellular compartments, such as the nucleus. A common strategy to address this issue is the use of CPPs, short (<20 amino acids), cationic molecules that are biocompatible, easily synthesised and can be conjugated onto a range of substrates, such as AuNP (Todorova et al., 2014). A commonly used peptide is Tat, a naturally occurring CPP that is derived from the transactivator of transcription of HIV (Patel et al., 2008; Krpetić et al., 2011; Yi et al., 2012; de la Fuente and Berry, 2005). Full length mutational analysis of the HIV-tat protein revealed that an unstructured N-terminal sequence (GRKKRRQRRR) is essential and sufficient for cellular entry and nuclear delivery (Kauffman et al., 2015). Cornelissen et al. (2009, 2011, 2012) have previously shown that conjugation of an extended variant of Tat (GRKKRRQRRRPPQGYG) facilitated cellular penetration and nuclear localisation of radiolabelled antibodies (Cornelissen et al., 2009b, 2011, 2012). For the synthesis of ON-AuNP-Tat, the sequence was modified by addition of a cysteine (GRKKRRQRRRPQGYGCG) to enable formation of an S-Au bond (Fig. 3.1).

3.1.5 PEGylation of gold nanoparticles

Thiol-modified PEG chains are commonly used to decorate the surface of AuNPs to increase their *in vivo* stability and to avoid uptake by the RES, features that are attributed to reduced receptor binding and increased hydrophobicity (Manson et al., 2011). PEG forms tight

associations with water molecules via ethylene glycol units, which results in the formation of a hydrating layer. For the work presented in this thesis, PEG chains with an average molecular weight of 800 Da were used to functionalise ON-AuNP-Tat (Fig. 3.1).

3.1.6 Aims and outline

The aim of the studies described in this chapter was to synthesise and characterise ^{111}In-, Cy3, and Cy5-labelled anti-hTR oligonucleotide-decorated AuNP with diameter of 15 or 2 nm (schematically represented in Fig. 3.3). AuNP size and functionalisation were assessed with TEM, UV-Vis spectrometry, radio-TLC and DLS analysis.

3.2 Methods

For materials and methods, see Chapter 2.2.

3.3 Results

3.3.1 Oligonucleotide modifications

Match and Scramble oligonucleotides with 5'end amino-modification and 3'end thiol-modification were coupled to the fluorophore Cy3 for confocal microscopy and Cy5 for *in vivo* detection with IVIS. Reaction product and fluorophores were separated by SEC and analysed by UV-Vis spectrometry. The labelling efficiency was calculated by the ratio of the concentration of oligonucleotides (λ = 260 nm, ε = 138.8) and Cy3 / Cy5 (λ = 548 / 647 nm, ε = 150 / 250). The typical labelling yield for Cy3-conjugation was 50-60% and for Cy5-conjugation was 65-75%. Fig. 3.4 A and B represent typical UV-Vis spectra of Cy3-Match ($A_{260\ nm}$ = 0.562, $A_{548\ nm}$ = 0.358) and Cy5-Match ($A_{260\ nm}$ = 0.369, $A_{647\ nm}$ = 0.472). To label Match and Scramble with ^{111}In, oligonucleotides were conjugated to DTPA at the 5'end amino site (Fig. 3.2). Reaction product and unreacted DTPA were separated by SEC as described earlier, and the efficiency of the reaction was tested by labelling of the compound with a tracer amount of ^{111}In.

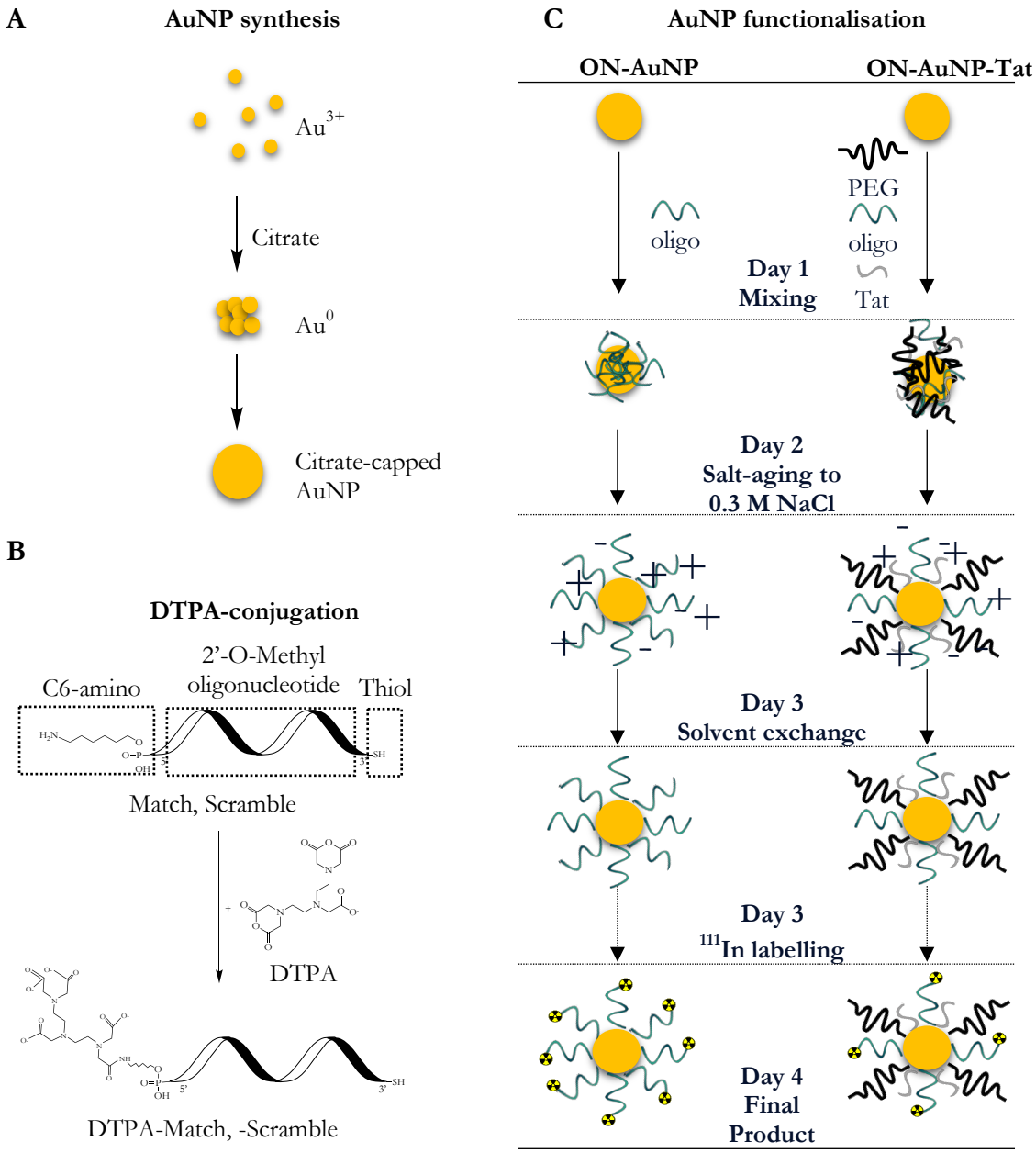


Figure 3.3 Schematic representation of the synthesis of hTR-targeting AuNP. A) AuNP synthesis. AuNP of 15.5 nm diameter are synthesised by citrate reduction. B) DTPA is conjugated to Match and Scramble oligonucleotides via a reaction with the 5'end C6-amino linker. C) The functionalisation of AuNP. Ligand shell compounds and AuNP were mixed on day 1 and incubated overnight. On day 2, both suspensions were salt-aged over an 8 h period to achieve a final NaCl concentration of 0.3 M and then shaken overnight. On day 3, the functionalised AuNP were purified by centrifugation, after which the pellet was resuspended in in sodium citrate (0.1 M, pH5.0). Subsequently, $^{111}InCl_3$ at the desired specific activity was added and incubated overnight. The next day, radiolabelling was confirmed by TLC, and AuNP were purified by centrifugation (See Chapter 2.2 for further details).

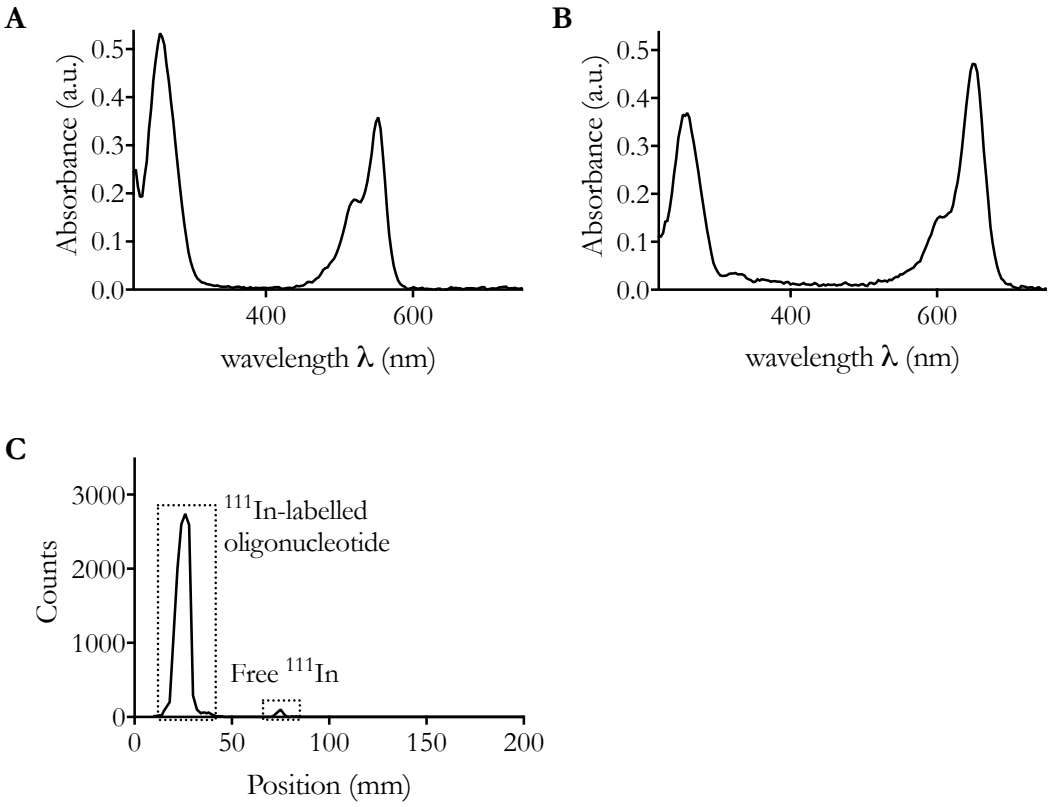


Figure 3.4 Oligonucleotide 5' end modifications. A) UV-Vis spectrum of Cy3-labelled Match oligonucleotides. Two distinct peaks are visible at λ = 260 nm (oligonucleotides) and at λ =548 nm (Cy3-probe), indicating successful conjugation. B) UV-Vis spectrum of Cy5-labelled Match oligonucleotides. A peak at λ = 260 nm (oligonucleotides) and at λ = 647 (Cy5-probe) demonstrate successful labelling of the sequence. C) TLC reading of ^{111}In-DTPA labelled Match oligonucleotides. A distinct peak at position = 25 mm, revealing the presence of ^{111}In-Match, covers the surface of 98% of the graph. At roughly 75 mm, a small amount of radioactivity is found, which indicates a trace amount of free ^{111}In.

A typical TLC for ^{111}In-labelling of DTPA-Match (hereafter called Match) with 0.8 MBq/μg (98% radiolabelling efficiency) is shown in Fig. 3 C. The labelling efficiency of Match and DTPA-Scramble (hereafter called Scramble), as calculated by the area under the curve (AUC) of the TLC peak at 20 mm, were routinely found to be between 90-95% of the total AUC for a maximum molar activity of 27 MBq/nmol.

3.3.2 Gold nanoparticle synthesis

AuNPs were routinely synthesised as described in Chapter 2.2.2 (Fig. 3.3 A).

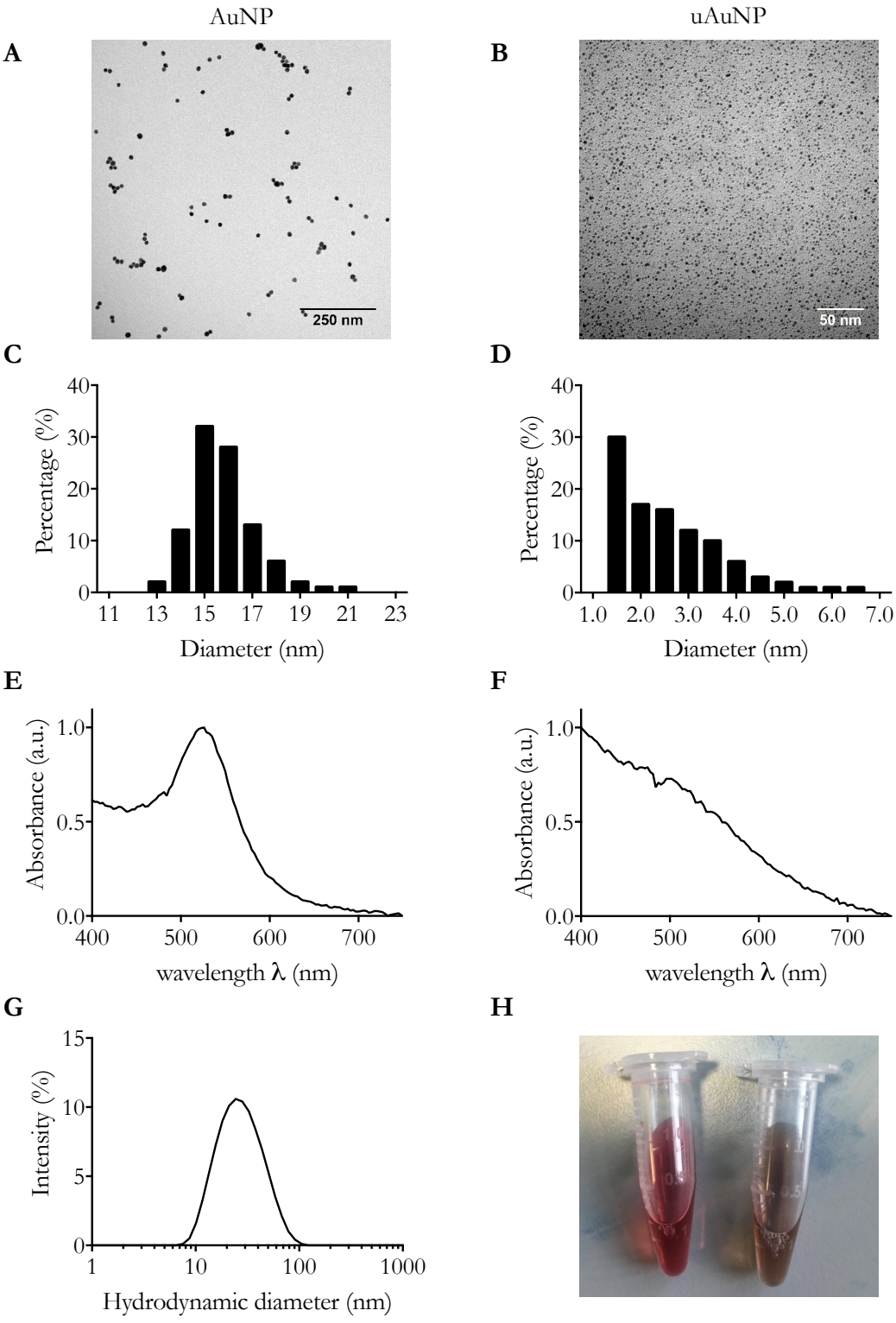


Figure 3.5 AuNP properties. A) TEM image of 15.5 nm AuNP. B) TEM image of 2.4 nm AuNP. C) Size distribution of 15.5 nm AuNP. D) Size distribution of 2.4 nm AuNP. E) UV-Vis spectrum of 15.5 nm AuNP in water. A distinct plasmon resonance peak is measured at λ = 525 nm. F) UV-Vis Spectrum of 2.4 nm AuNP in water. G) DLS measurement of 5 nM 15.5 nm AuNP in water. The overall hydrodynamic diameter was determined to be 25.3 nm. H) Image of Eppendorf tubes with 15.5 nm (left) and 2.4 nm (right) AuNP.

Citrate reduction of $HAuCl_4$ resulted in the formation of spherical AuNP with an average diameter of 15.5 ± 1.9 nm and a narrow size distribution as determined by TEM (Fig. 3.5 A and C).

AuNP solutions were analysed with UV-Vis spectrometry (Fig. 3.5 E) and the concentration was determined by the method of Lambert-Beer and extinction coefficients from Haiss et al. (2007). Typically, synthesis of an AuNP batch resulted in 200 mL of concentration 10-15 nM. The plasmon resonance peak was found at the characteristic wavelength of 524 nm, which is expected for AuNP of this size. DLS analysis confirmed that the solution consisted of particles of uniform size (polydispersity index (PDI): 0.247). The overall hydrodynamic diameter was 25.3 nm (Fig. 3.5 G).

uAuNP were synthesised by THPC reduction of $HAuCl_4$ as described in Chapter 2.2.2. TEM images showed that most particles are roughly spherical and between 1.5 and 3.5 nm in diameter with an average diameter of 2.4 ± 1.2 nm (Fig. 3.5 B and D). The uAuNP solution was filtered with a 30 kDa filter unit to remove larger aggregates. UV-Vis spectrometry demonstrated a leftward shift of the plasmon resonance peak (λ = 510-520 nm) in comparison to 15.5 nm AuNP (Fig. 3.5 F). This resulted in a difference in colour (burgundy for 15.5 nm AuNP, brown for 2.4 nm AuNP), which is illustrated in Fig. 3.5 H. A typical synthesis resulted in a 10 mL solution of 2 μM.

Table 3.2 Characteristics of AuNP constructs.

Size	Construct	Number of Oligonucleotides	Hydrodynamic diameter (nm)	PDI
15.5 nm	Match-AuNP	76	33.3	0.232
	Scramble-AuNP	67	33.3	0.218
	Match-AuNP-Tat	14	38.3	0.332
	Scramble-AuNP-Tat	16	37.7	0.263
2 nm	Match-uAuNP	1	-	
	Scramble-uAuNP	1	-	

3.3.3 Gold nanoparticle functionalisation

3.3.3.1 ON-AuNP

15.5 nm AuNPs were functionalised with Match and Scramble oligonucleotides as described in Chapter 2. UV-Vis spectrophotometry revealed no shift in plasmon resonance peak or other changes in the spectrum for Match- or Scramble-functionalised AuNP (Fig. 3.6 A). DLS analysis demonstrated that functionalised particles were monodisperse (PDI = 0.232 (Match-AuNP) and 0.218 (Scramble-AuNP)) (Fig. 3.6 B). The hydrodynamic diameter of the constructs increased from 25.4 for AuNP to 33.3 nm when decorated with either Match or Scramble oligonucleotides, which is consistent with an increase in size due to oligonucleotide functionalisation. Labelling of Match and Scramble with ^{111}In prior to AuNP-functionalisation allowed for determination of the number of oligonucleotides on the surface of each nanoparticle (Match-AuNP: 76, Scramble-AuNP: 67) (Table 3.2). This number indicates an oligonucleotide labelling efficiency between 33 - 38%.

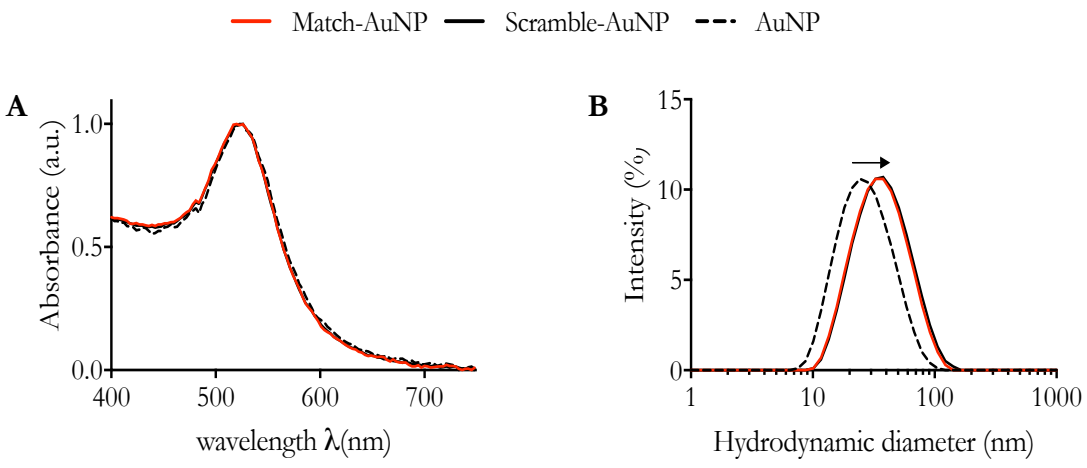


Figure 3.6 Functionalisation of Match-AuNP and Scramble-AuNP. A) UV-Vis spectrum of ON-AuNP in water. The overlapping of the curves between AuNP, Match-AuNP and Scramble-AuNP suggests no aggregation, since a rightward shift is associated with an increase in particle size. B) DLS of Match-AuNP and Scramble-AuNP in water. A rightward shift (from 25.4 nm to 33.3 nm) of Match-AuNP and Scramble-AuNP indicates surface functionalisation.

3.3.3.2 ON-AuNP-Tat

To synthesise ON-AuNP-Tat, several mixing strategies and concentrations were tested. Direct mixing of oligonucleotides and Tat with 15.5 nm AuNP resulted in aggregation after salt-aging (Fig. 3.7 A, No PEG). To mitigate this effect, PEG800-SH was tested by adding increasing concentrations prior to the addition of Match or Scramble oligonucleotides and Tat. It was found that an AuNP : PEG800-SH mixing ratio of 1 : 3000 was sufficient to avoid aggregation after addition of 0.3 M NaCl (Fig. 3.7 A). The UV-Vis spectra of Match-AuNP-Tat and Scramble-AuNP-Tat showed clear peaks at the plasmon resonance wavelength (Fig. 3.7 B). DLS demonstrated that the PDI was 0.332 and 0.263 for Match-AuNP-Tat and Scramble-AuNP-Tat, indicating little aggregation (Fig. 3.7 C). The hydrodynamic diameter after functionalisation increased from 25.4 nm (AuNP) to 38.4 nm (Match-AuNP-Tat) and 37.7 nm

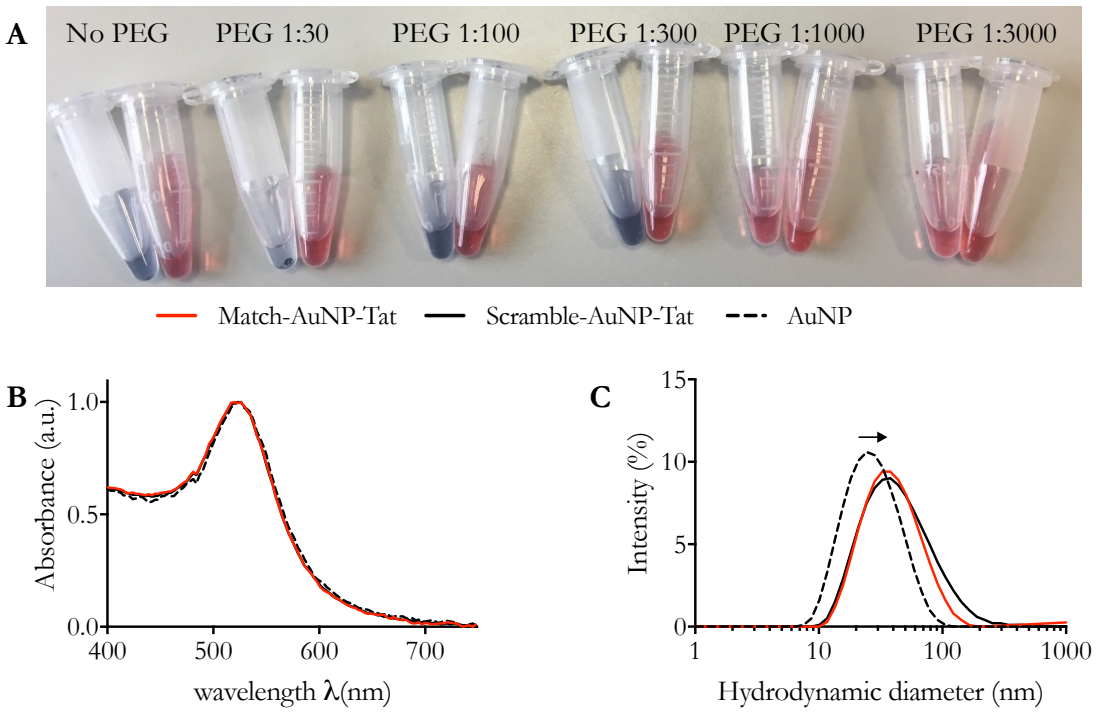


Figure 3.7 Functionalisation of Match-AuNP-Tat and Scramble-AuNP-Tat. A) Photograph of the effect of PEG800-SH mixing ratios on 0.3 M NaCl-induced aggregation. B) UV-Vis spectrum of ON-AuNP-Tat in water. The overlapping curves between AuNP, Match-AuNP-Tat and Scramble-AuNP-Tat indicate stable particles with little or no aggregation. C) DLS of Match-AuNP-Tat and Scramble-AuNP-Tat in water. A rightward shift from 25.4 nm to 38.4 nm (Match-AuNP-Tat) and 37.7 nm (Scramble-AuNP-Tat) indicates surface functionalisation.

(Scramble-AuNP-Tat). The total number of oligonucleotides per AuNP were 14 for Match-AuNP-Tat and 16 for Scramble-AuNP-Tat (Table 3.2), corresponding to labelling efficiencies of 14 and 16%, respectively.

3.3.3.3 ON-uAuNP

ON-uAuNP were synthesised as described in Chapter 2.2. After synthesis of uAuNP, Match and Scramble oligonucleotides were attached to the surface via an S-Au bond. The obtained colloidal suspensions were analysed using a Nanodrop. The spectra are presented in Fig. 3.8 and show a plasmon resonance peak at λ = 510-520 with an increased absorbance in comparison to unmodified uAuNP. uAuNP were below the detection limit of the Zetasizer, and therefore DLS was not possible. On average, one oligonucleotide attached per uAuNP.

3.3.4 Gold nanoparticle radiolabelling

ON-AuNP, ON-AuNP-Tat and ON-uAuNP were labelled with ^{111}In and purified by centrifugation. The molar activity for ON-AuNP, ON-AuNP-Tat and ON-uAuNP were 27, 18 and 13.5 MBq/nmol oligonucleotide, respectively. The radiochemical purity after centrifugation was consistently between 90 and 95% for ON-AuNP and ON-AuNP-Tat but remained limited to 40-60% for ON-uAuNP. Labelling did not occur when ^{111}In was added to unmodified 15.5 nm or 2.4 nm AuNP (data not shown). Typical radiochemical purity data for each nanoconstruct is represented in Fig. 3.9.

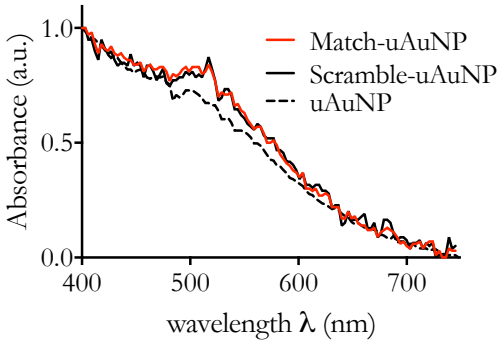


Figure 3.8 Functionalisation of Match-uAuNP and Scramble-uAuNP in water. Functionalisation resulted in an increased absorbance at λ = 510-520, which may suggest aggregation of particles.

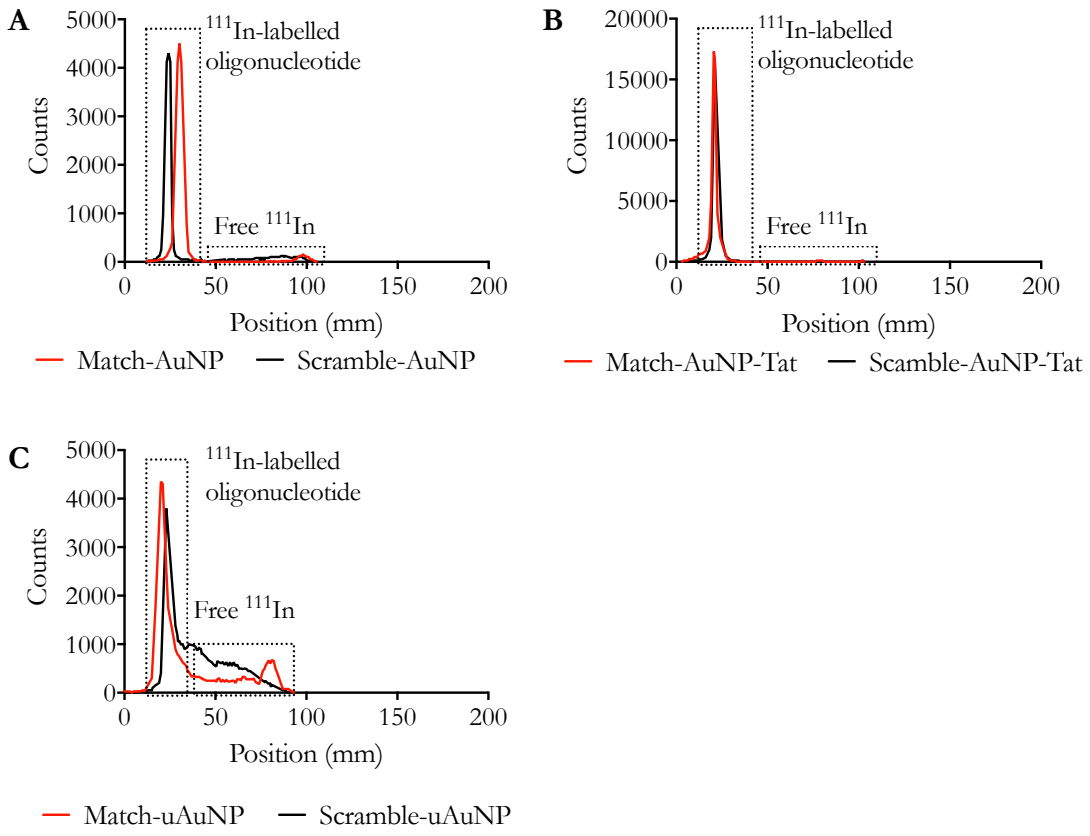


Figure 3.9 TLC data for ON-AuNP, ON-AuNP-Tat, and ON-uAuNP after purification. A) A typical TLC for Match-AuNP and Scramble-AuNP (Radiochemical purity 95% and 90%, respectively) B) A typical TLC for Match-AuNP-Tat and Scramble-AuNP-Tat (Radiochemical purity 98% and 99%, respectively). C) A typical TLC for Match-uAuNP and Scramble-uAuNP (Radiochemical purity 58% and 40%, respectively).

3.3.5 Gold nanoparticle stability

The stability of Match-AuNP and Match-AuNP-Tat was measured as a change in Z-average or change in peak 1 percentage (the AUC percentage of particles that is covered by the first peak of the DLS spectrum). The DLS measurement was performed over time at 4 and 37 °C (Fig. 3.10). Z-average and peak 1 percentage for Match AuNP are stable for at least two weeks at 4 and 37 °C. For Match-AuNP-Tat, there is a 3% change in Z-average after 24 h at 37 °C, and 8% after 72 h, indicating slight aggregation. At 4 °C, there is a slight increase in Z-average size after 72 h, which remained constant over time. Peak 1 percentage fluctuated around 100% for both constructs at 4 and 37 °C.

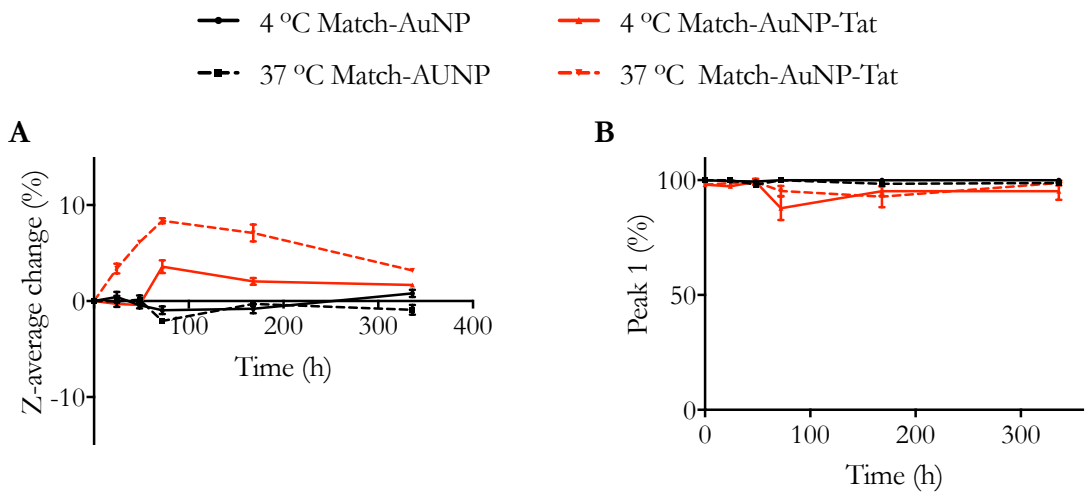


Figure 3.10 AuNP stability. A) the Z-average change of Match-AuNP and Match-AuNP-Tat in water was monitored over time at 4 and 37 °C. B) The peak 1 percentage of Match-AuNP and Match-AuNP-Tat in water was monitored over time at 4 and 37 °C.

3.4 Discussion

Oligonucleotides are promising ligands for therapeutic targets involved in cancer pathways, such as proteins, mRNA, and DNA. In contrast to many small-molecule drugs, oligonucleotides require alternative nucleic acid chemistry and drug delivery vectors for protection against nuclease degradation and hydrolysis, as well as to improve cellular and nuclear uptake. Furthermore, chemical modifications may facilitate the labelling with fluorophores and radionuclides for therapeutic and diagnostic ends (Khvorova and Watts, 2017).

3.4.1 Oligonucleotides were modified with 5'end fluorophores and ^{111}In-DTPA

To enable detection of ON-AuNP and ON-AuNP-Tat by laser-scanning confocal microscopy (Chapter 4) and IVIS imaging (Chapter 5), oligonucleotides were successfully labelled with Cy3 and Cy5 fluorophores, respectively. The free amine-group at the 5'end of oligonucleotides provided a reactive group for EDC/NHS conjugation of both fluorophores (50-60% (Cy3), 65%-75% (Cy5)). Fluorophore labelling yield was found to be consistent with data provided by the dye manufacturer. Partial labelling should be sufficient for detection by earlier mentioned

methods, given that each nanoparticle has 67 – 76 (ON-AuNP) and 14-16 (ON-AuNP-Tat) oligonucleotides, and therefore at least 35 and 7 fluorophores per particle, respectively.

Oligonucleotides were conjugated to DTPA and labelled with ^{111}In. TLC analysis revealed that the maximum molar activity was 27 MBq/nmol, which corresponded with the previously obtained maximum molar activity by Jackson et al. (2018). In the Jackson study, Match and Scramble oligonucleotides without 3'-end thiol modification were used for radiolabelling. Given that this modification was not expected to interfere with the reaction, radiolabelled oligonucleotides in this study were considered to have the same properties. Jackson showed that the radiolabelling of 2'OMeRNA oligonucleotides was dependent on DTPA-labelling and resistant against autoradiolysis after 24 h. The latter is attributed to the hexyl-linker that separates the chelator from the oligonucleotide sequence. We can therefore expect a similar result for these oligonucleotides.

3.4.2 Gold nanoparticles were synthesised for drug delivery

AuNP with diameters of 15.5 and 2.4 nm were synthesised as vectors for oligonucleotide stabilisation and cellular internalisation. The narrow size distribution of 15.5 nm AuNP and the typical plasmon resonance peak at 524 nanometres wavelength were an indication of successful synthesis with little or no aggregation (Patel et al., 2008). The difference between the hydrodynamic diameter as measurement by DLS (25.3 nm) and the diameter as measured by TEM (15.5 nm) is commonly described in the literature (Zheng et al., 2016; Fissan et al., 2014; Domingos et al., 2009; Bootz et al., 2004). Whereas TEM measures the core of the nanoparticle, DLS also considers the stabiliser-solvent (citrate and Tween-20). Moreover, TEM is a number-based analysis, whereas DLS is in this instance used as an intensity-based method. In the latter case, this can skew the results to an increased diameter average when a few large aggregates are present in the solution (Fissan et al., 2014). Particles remained stable at 4 °C for at least 6 months (results not shown).

The size distribution of 2.4 nm AuNP was wider, and had a tail of larger aggregates, requiring the use of a filter unit to separate the particles above 5 nm. The UV-Vis spectrum is less distinct than the spectrum of the 15.5 nm AuNP, but still demonstrated a plasmon resonance peak at a wavelength of 510-520 nm, as described previously by Kumar et al. (2013). Because of Ostwald ripening of the suspension, a process in which small nanoparticles in suspension grow over time (Kumar et al., 2013), particles were made up fresh prior to every experiment. Although this is feasible in a laboratory setting, this requires optimisation for eventual translation to the clinic.

3.4.3 Gold nanoparticles were functionalised with oligonucleotides

It has been shown previously that 15.5 nm AuNP can be functionalised with PEG2000-SH and ^{111}In-labelled hEGF (Song et al., 2016, 2017). In this chapter, it is demonstrated that AuNP can be decorated with a monofunctional layer of ^{111}In-labelled Match or Scramble oligonucleotides, or a multifunctional layer consisting of ^{111}In-labelled Match or Scramble oligonucleotides, PEG800-SH and Tat. For ON-AuNP, between 67 and 76 oligonucleotides were covalently bound to the surface of the AuNP. This number is roughly the same as found previously by Hurst et al. (2006) for same size AuNP, and correlates with the hydrodynamic diameter shift from 25.4 to 33.3 nm, which is indicative of oligonucleotides binding to the AuNP. Match-AuNP has been demonstrated to be stable for at least two weeks at 4 and 37 °C (Fig. 3.10). In this chapter, successful radiolabelling for ON-AuNP is demonstrated by TLC. The maximum specific activity of ON-AuNP matched the maximum molar activity of non-conjugated Match and Scramble oligonucleotides (27 MBq/nmol), indicating that all DTPA groups were available for labelling.

Following on from the successful functionalisation and radiolabelling described in this chapter, ON-AuNP were further characterised in *in vitro* experiments (Chapter 4).

3.4.4 Gold nanoparticles were functionalised with oligonucleotides and Tat

Since the electrostatic interaction between Tat and oligonucleotides resulted in unstable AuNP when mixed, a novel strategy was tested. Several approaches have been described in the literature. Patel et al. (2008) added 0.2 M NaCl to 15 nm AuNP in a buffered solution of 0.1% Tween-20 prior to ligand addition to screen the electrostatic attraction between the oligonucleotides and peptides, which led to the formation of stable particles. De la Fuente and Berry (2005) functionalised 3 nm AuNP using the reactivity of the free carboxyl group of the capping agent tiopronin with the free amines of Tat to form an ester bond. Krpetić et al. (2011) premixed CALNN-Tat with PEG prior to addition to AuNP to mitigate aggregation, and found that this was sufficient for stable AuNP. Since PEG can also function as an agent to increase the *in vivo* stability and to prolong the circulation time, it was decided to work with a similar approach as Krpetić et al. This resulted in heavily PEGylated particles with an average number of 14 (Match) and 16 (Scramble) copies of the oligonucleotides present on the surface. This is five- to six-fold less than was found by Patel et al., and can likely be attributed to PEGylation on the surface of ON-AuNP-Tat, resulting in less space available for attachment of oligonucleotides. The hydrodynamic size of the particles increased from 25.4 nm (AuNP) to 38.4 nm (Match-AuNP-Tat) and 37.7 nm (Scramble-AuNP-Tat). Compared to ON-AuNP (33.3 nm), this is a size increase of roughly 5 nm, and is consistent with Tat/PEG800-SH conjugation to the surface of the NP. This provides indirect evidence for Tat conjugation and further indirect evidence of the presence of Tat on the surface of AuNP (in the form of PCR inhibition) is presented later in Chapter 4. To directly measure the number of Tat molecules on the AuNP future work includes the detection of radioactivity via radio-iodination of the tyrosine in the Tat sequence. This would allow quantification of the number of Tat molecules with high sensitivity by correlating concentration to CPM, as has been done for ^{111}In-labelled oligonucleotides.

ON-AuNP-Tat were stable at 4 °C and were stored for a maximum of 2 weeks prior to each experiment. At 37 °C, a slight increase in Z-average size (3%) after 24 hours was observed, which indicates the formation of a number of aggregates. After 72 hours this increase had risen to 8%. Given the electrostatic interactions between the surface ligands, aggregation at higher temperatures was expected. *In vitro* experiments at 37 °C were conducted for a maximum of 24 h, and therefore it is hypothesised that the impact of aggregation of particles is minimal. ON-AuNP-Tat had a molar specific activity of 18 MBq/nmol, suggesting that not all DTPA groups were accessible. This is potentially the result of shielding by the more complex ligand shell, which includes PEG800-SH and Tat.

As a result of the successful radiolabelling and synthesis of ON-AuNP-Tat, the constructs were trialled *in vitro* to test their potential therapeutic effect (Chapter 4).

3.4.5 Ultra-small gold nanoparticles were functionalised with oligonucleotides

Ultra-small AuNP are of increasing interest to the research community due to their differential pharmacokinetic profile in comparison to larger AuNP. Whereas larger AuNP are cleared hepatically, uAuNP have been found to be cleared renally, allowing for different targeting strategies. Several functionalisation methods are described in the literature, including the use of PEG-linkers (Kumar et al., 2013), tiopronin linkers (Huo et al., 2014), or direct covalent attachment via ligand exchange (Ackerson et al., 2010). In this thesis, we opted for direct covalent attachment, which resulted in the addition of 1 oligonucleotide per 2.4 nm AuNP. This number can likely be increased by using PEG-linkers to increase the flexibility, and there with the number of available sites of the ligand shell, as done previously by Kumar et al. (2013). Furthermore, a PEG-shell may reduce the aggregation that underlies the upward shift in the plasmon resonance peak when 2.4 nm AuNP are conjugated to Scramble or Match oligonucleotides. ON-uAuNP did not produce a clean TLC, which indicated poor radiochemical purity. The maximum molar activity was estimated to be 13.5 MBq/nmol.

The results in this paragraph indicate that synthesis of ON-uAuNP requires further optimisation before proceeding to *in vitro* characterisation. The potential of the construct is demonstrated in a confocal microscopy experiment in Chapter 4, but further development was halted due to the impurity of the radiolabelled construct and the rapid aggregation after functionalisation.

3.4.6 Concluding remarks

The aim of the studies described in this chapter was to synthesise and characterise ^{111}In-, Cy3, and Cy5-labelled anti-hTR oligonucleotide-functionalised AuNP. The replication of the fluorophore- and radiolabelling of Match- and Scramble oligonucleotides described by Jackson et al. provided a starting point for the development of an AuNP-based delivery system. AuNP of diameter 2.4 and 15.5 nm were successfully synthesised. AuNP (15.5 nm) were decorated with a fluorophore- or radio-labelled monofunctional oligonucleotide layer (ON-AuNP) and a multifunctional oligonucleotide/peptide/PEG layer (ON-AuNP-Tat). AuNP (2.4 nm) were functionalised with oligonucleotides, but radiolabelling failed to give a high radiochemical purity. Based on these results, ON-AuNP and ON-AuNP-Tat were further developed *in vitro* (Chapter 4), and the development of ON-uAuNP was ceased.

CHAPTER 4. *IN VITRO* CHARACTERISATION OF GOLD NANOPARTICLE RADIOPHARMACEUTICALS

4.1 Introduction

This chapter demonstrates the *in vitro* properties of the AuNP constructs described in Chapter 3. ON-AuNP and ON-AuNP-Tat were evaluated by TRAP assays, internalisation and fractionation assays, confocal microscopy, TEM, clonogenic survival assays, and γH2AX assays. The results of this chapter form the basis for *in vivo* testing of fluorophore- and radiolabelled AuNP constructs (Chapter 5).

4.1.1 Telomerase inhibition with radiolabelled oligonucleotides

The role of telomerase in the DDR and genomic stability offers the opportunity for simultaneous therapeutic exploitation of the interaction between telomerase inhibition and ionising radiation (Wu et al., 2017b; Yu et al., 2015). Previously, it has been demonstrated that incubation with 2'OMeRNA hTR-binding oligonucleotides (Match) resulted in a dose-dependent inhibition of telomerase activity (IC_{50}: 147 nM), whereas non-complimentary oligonucleotides (Scramble) did not have a demonstrable effect. Furthermore, ^{111}In-labelling of DTPA-conjugated constructs did not significantly change affinity in comparison to constructs that were unlabelled, indicating the radiolabel did not interfere with the binding site (Jackson et al., 2018).

To assess the effect of AuNP conjugation on the telomerase-inhibiting potential of Match oligonucleotides, ON-AuNP and ON-AuNP-Tat were tested in the TRAP assay. The TRAP assay is a commonly used protocol to assess telomerase activity in cells and tissues (Fajkus, 2006). It is a PCR-based technique, in which a telomerase substrate (TS) primer is incubated with a test cell lysate sample to enable extension with hexanucleotide telomeric repeats in the presence of active telomerase. The extended TS primers associate with reverse primers, enabling

the formation of a product that can be amplified by conventional PCR. The reverse primer can be labelled with a fluorophore and quenching sequence, which causes the fluorophore to be active only if bound to TS extended primers (Tyagi and Kramer, 1996). The signal can be normalised against an internal PCR amplification control and a telomerase-independent template (TSR8) to give a quantitative measure of telomerase activity (Uehara et al., 1999).

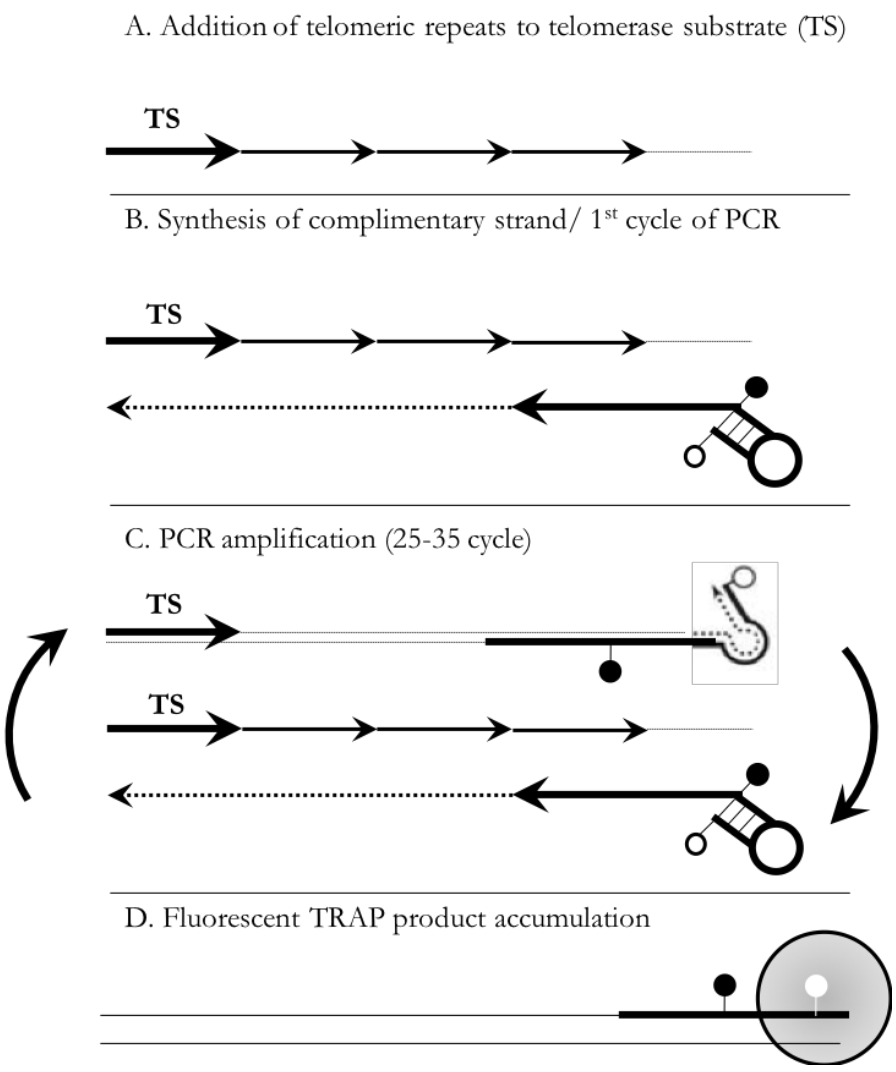


Figure 4.1 TRAP assay steps. A) In the presence of active telomerase, the TS primer can be elongated with hexanucleotide telomeric repeats. B) During the first PCR cycle, the complimentary strand, which can be labelled with a fluorophore and quenching moiety, is synthesised. The quenching moiety enables detection only when incorporated into a PCR product. C) The PCR amplification cycle enables the synthesis and accumulation of fluorescent TRAP product, which D) can be measured using a plate reader.

4.1.2 Subcellular distribution of gold nanoparticle constructs

hTR binds several proteins, including dyskerin, NOP10, NHP2, and GAR1, that stabilise the RNA and promote assembly of hTR with the enzymatic TERT subunit of telomerase in the Cajal bodies. Importantly, the dyskerin–NOP10–NHP2–NAF1 complex causes nuclear retention of hTR, requiring nuclear localisation of targeting probes (Kiss et al., 2010). Jackson et al. (2018) studied the effect of ^{111}In-labelled hTR targeting oligonucleotides by using a transfection agent to shuttle the fluorophore-tagged oligonucleotides over the cell membrane into the cytosol and nucleus. Using this method, it was demonstrated that oligonucleotides were taken up readily after 2.5 h and showed foci in the nuclei after 4 h. This signal overlapped with Cajal bodies in multiple instances, suggesting binding of Match to hTR at the site of telomerase assembly. However, transfection agents are not suited for use in the clinical setting due to low systemic stability, and therefore the use of AuNP delivery of oligonucleotides was explored.

In this chapter, the subcellular distribution of AuNP constructs is assessed with internalisation and fractionation assays. Cellular fractions can be separated by centrifugation in various buffers, and the radioactive emission can be measured with a gamma-counter, making it possible to obtain a highly quantitative measure of the relative uptake per subcellular compartment. Several researchers have demonstrated this approach, including Gill et al. (2018), Cai et al. (2010), and Ngo Ndjock Mbong et al. (2015). Although this technique is excellent for describing the average internalisation for cell populations, spatial information is lost. Furthermore, it provides a population average distribution and does not take into account the large variation of uptake on an individual cell level. For this reason, TEM and laser-scanning confocal microscopy were performed. TEM can detect the cellular localisation of AuNP due to their high Z-number in comparison to tissue, enabling detection of constructs with high spatial resolution (Chithrani et al., 2006). Combined with laser-scanning confocal microscopy to detect of Cy3-labelled oligonucleotides *in vitro*, this approach can give a quantitative and qualitative measure of the subcellular distribution of ON-AuNP and ON-AuNP-Tat (Bavelaar et al., 2018).

4.1.3 Telomerase and gold nanoparticle radiosensitisation

In this thesis, AuNP are used as delivery vehicles for radiotoxic compounds in telomerase-positive cancer cells. Several studies have demonstrated that sufficient AuNP constructs can be delivered into target organelles to exert cellular effects. Pioneering work by the Mirkin group has shown that introduction of AuNP constructs functionalised with siRNA against luciferase or enhanced green fluorescent protein (EGFP) RNA could suppress protein expression (Giljohann et al., 2009; Rosi et al., 2006). Furthermore, Song et al. (2016) showed that ^{111}In-EGF-labelled AuNP accumulated in the perinuclear space, and lead to a significant reduction in clonogenic survival. A similar result was demonstrated for AuNP functionalised with ^{111}In-labelled trastuzumab to target the cell surface receptor Her2 (Cai et al., 2016).

The anticipated mechanism of cell killing by ^{111}In-Match-AuNP and ^{111}In-Match-AuNP-Tat involves concomitant radiation delivery via ^{111}In and hTR inhibition-related radiosensitisation, as discussed in Chapter 1. Jackson et al. (2018) demonstrated that ^{111}In-labelled oligonucleotides against hTR reduced the survival of telomerase-positive cancer cells, but not of telomerase-negative cancer cells, and that this correlated with a significant upregulation in DNA damage. For this reason, we hypothesised that ^{111}In-Match-AuNP and ^{111}In-Match-AuNP-Tat would also exert a specific effect on telomerase-positive tumours.

Interestingly, in addition to hTR inhibition-dependent radiosensitisation, reports have indicated that AuNPs can act as radiosensitisers independent of their payload (Her et al., 2017). Several authors describe that photons can interact with AuNP via the Compton or photoelectric effect, leading to the formation of Auger electrons that can ionise the immediately adjacent cellular environment. Therefore, we postulated that hTR-targeting AuNP might also enhance the effect of external beam radiation.

To study these effects, clonogenic survival and γH2AX assays are performed in telomerase-positive and negative cell lines. Clonogenic survival assays are the gold standard in radiation

biology research, and test the capacity of radiation or drugs to cause reproductive cell death (Franken et al., 2006). A common cause of reproductive cell death is the induction of DNA DSBs (Rogakou et al., 1998). An early step in the repair of DNA DSBs is the phosphorylation by P13K-like kinases, ATR, ATM or DNA-PKcs of histone H2AX on serine S-139 which leads to the accumulation of γH2AX near DSBs. γH2AX forms foci, recruits DNA repair proteins, and plays a role in DNA end re-joining and error-free repair (Nakamura et al., 2010). A significant induction of γH2AX foci follows cellular exposure to genotoxic treatment such as external beam radiation or TRT. Foci can be visualised *in vitro* by using a widely used immunofluorescence assay, that gives an indication of the number of DNA DSBs (Cornelissen et al., 2011). Because it is theorised that ^{111}In-Match-AuNP and ^{111}In-Match-AuNP-Tat radiosensitise the cell whilst concomitantly delivering a radiation dose, clonogenic survival and γH2AX assays were used to provide an insight into the cellular and molecular effects of these constructs.

4.1.6 Aims and outline

The aim of the studies described in this chapter was to characterise the *in vitro* properties of ^{111}In-labelled anti-hTR oligonucleotide-decorated AuNPs. AuNP constructs were tested in TRAP, internalisation and fractionation assays, confocal microscopy and TEM studies, and clonogenic and γH2AX assays.

4.2 Methods

For materials and methods, see Chapter 2.3 – 2.8.

4.3 Results

4.3.1 Telomerase inhibition

Telomerase activity was tested in TRAP assays with and without inhibitors. To determine which cell lines to use in subsequent *in vitro* studies, the telomerase activity in MDA-MB-435 and U2OS

was assessed (Fig. 4.2 A). It was found that MDA-MB-435 cells contained active telomerase (for 200 ng cell lysate, 68 ± 2% of the positive control TSR8 signal, n = 2). Telomerase activity was absent in U2OS (200 ng cell lysate, 1 ± 1% of TSR8 signal, n = 2). After determining telomerase activity in MDA-MB-435, Match and Scramble oligonucleotides were incubated with the cell lysate to determine the inhibitory effect of both sequences (Fig. 4.2 B). A clear dose-response effect was observed for Match oligonucleotide ($logIC_{50}$ -6.93 ± 0.072, Hill slope – 0.67 ± 0.074 (n = 2)). The telomerase activity in samples incubated with Scramble oligonucleotide did not differ significantly from that in untreated (control) cell lysate samples (One-Way ANOVA, Multiple Comparison, P=0.1355, n = 2).

4.3.1.1 ON-AuNP

After validation of the system, ON-AuNPs were tested in TRAP assays (Fig. 4.2 C). As for free Match oligonucleotides, Match-AuNP inhibited telomerase activity in a dose-dependent manner ($logIC_{50}$ -7.49 ± 0.04, Hill slope -1.46 ± 0.19). Scramble-AuNP did not significantly alter telomerase activity for concentrations in the range 0.1 - 100 nM.

An assay using the pre-elongated primer TSR8 instead of MDA-MB-435 lysate was performed to determine whether the inhibition of the telomerase signal was dependent on a non-specific reaction with one of the components of the reaction mix or product. Fig. 4.2 E shows that the TSR8 signal (100 ± 8.8%) was not significantly altered by AuNP-PEG (82.7 ± 5.4 %), Scramble-AuNP (90.0 ± 4.4%), or Match-AuNP (88.5 ± 6.0%) (One-Way ANOVA, Multiple Comparison, P = 0.1938, n = 2). This confirmed that Match-AuNP inhibited telomerase activity, rather than another compound of the reaction mix.

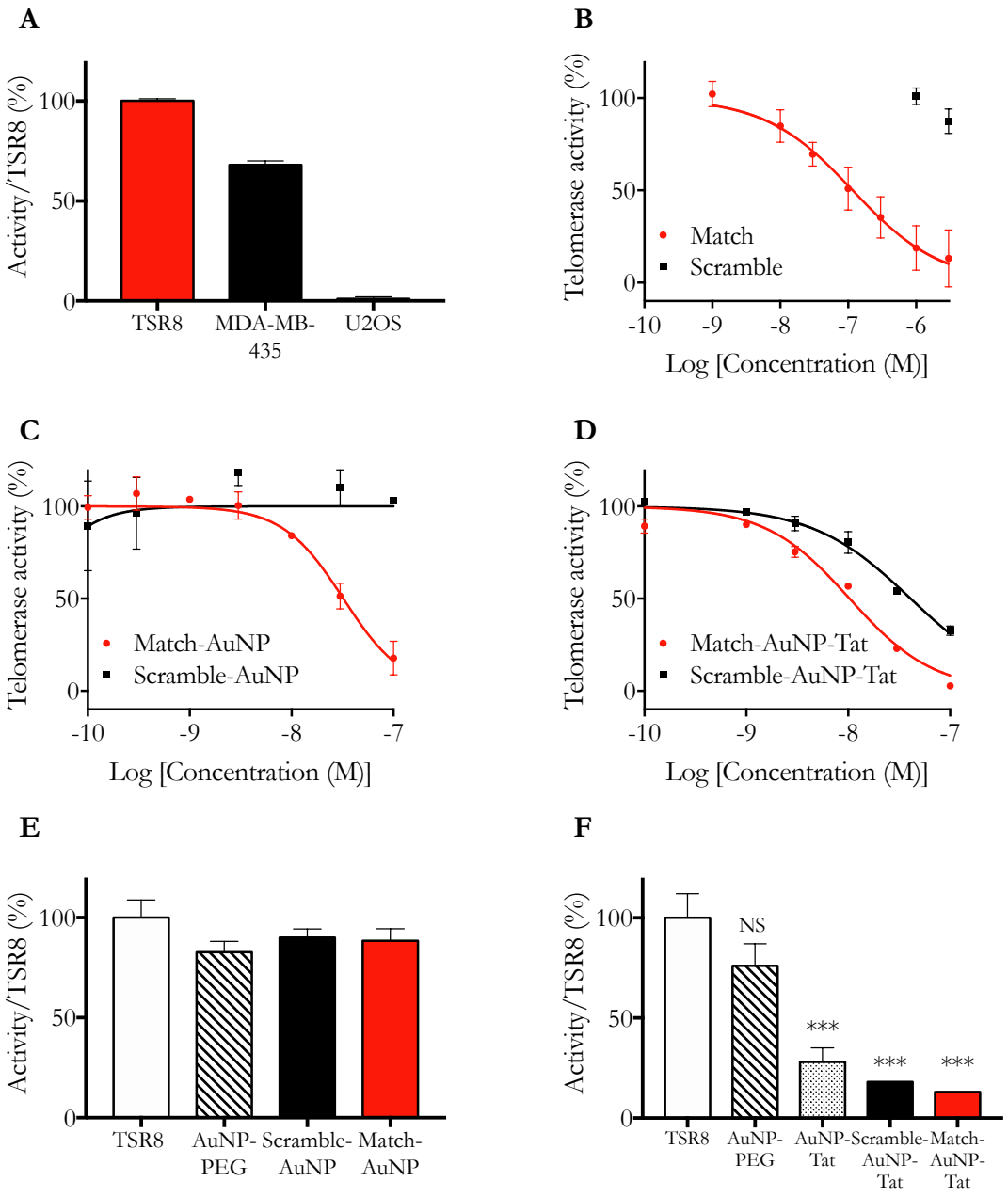


Figure 4.2 Telomerase activity inhibition with oligonucleotides and AuNP. A) Telomerase activity in MDA-MB-435 and U2OS cell lines. The y-axis represents the telomerase activity relative to the signal of 0.2 amole of TSR8 telomerase-independent pre-elongated primer. (n = 2). B) The dose-effect of oligonucleotides on telomerase activity. The y-axis represents the telomerase activity signal relative to the signal of untreated cells. The x-axis the logarithm of the concentration (M). The plotted data points are the results for Match and Scramble (n = 2). C) Dose-response curve of ON-AuNP versus telomerase activity. D) Dose-response curve of ON-AuNP-Tat versus telomerase activity. E) Influence of ON-AuNP constructs on TSR8 signal. F) Influence of ON-AuNP-Tat on TSR8 signal. Dose-response curves were plotted using GraphPad Prism. NS = not significant, *** = P < 0.001.

4.3.1.2 ON-AuNP-Tat

Similarly, the TRAP assay was conducted following exposure of cells to ON-AuNP-Tat constructs (Fig. 4.2 D). Match-AuNP-Tat inhibited telomerase activity in a dose-dependent manner ($logIC_{50}$ -7.99 ± 0.05, Hill slope -1.05 ± 0.27, n = 2). However, Scramble-AuNP-Tat also demonstrated a dose-dependent relationship ($logIC_{50}$ -7.39 ± 0.03, Hill slope –0.90 ± 0.06), although the $LogIC_{50}$s were statistically significantly different ($P < 0.0001$). These results raised the possibility that Scramble-AuNP-Tat was interfering with the measurement system rather than specifically inhibiting telomerase activity. Therefore, a control experiment with TSR8 was performed. Figure 4.2 F shows clearly that all compounds that were loaded with Tat reduced the signal of TSR8 significantly, indicating a non-specific interaction of Tat with one or more of the constituents of the TRAP assay (Untreated 100.0 ± 12.0%; AuNP-PEG 76.3 ± 11.2% ($P > 0.05$); AuNP-Tat 28.0 ± 7.0% ($P < 0.001$); Scramble-AuNP-Tat 18.0 ± 2.0% ($P < 0.001$); Match-AuNP-Tat 13.0 ± 3.5% ($P < 0.001$). One-Way ANOVA, Multiple Comparison, n = 2).

4.3.2 Subcellular distribution of gold nanoparticle constructs

4.3.2.1 Internalisation assays

To assess the cellular uptake of AuNP constructs, a 24 h internalisation assay was performed and the uptake as a percentage of the total added radioactivity was measured and calculated (Fig. 4.3 A). The uptake of oligonucleotides was dramatically improved by linking them to AuNPs (^{111}In-Match: 0.30 ± 0.01% vs ^{111}In-Match-AuNP: 3.62 ± 0.20% ($P < 0.005$), ^{111}In-Scramble: 0.26 ± 0.02% vs ^{111}In-Scramble-AuNP: 4.17 ± 0.39% ($P < 0.0001$)). Moreover, the addition of Tat and PEG800-SH to the nanocomplex further improved uptake after 24 h (^{111}In-Match-AuNP: 3.62 ± 0.20% vs ^{111}In-Match-AuNP-Tat: 5.61 ± 0.969% ($P=0.0005$), ^{111}In-Scramble-AuNP: 4.17 ± 0.39% vs ^{111}In-Scramble-AuNP-Tat: 5.67 ± 1.34% ($P=0.0095$)). (One-Way ANOVA, Multiple Comparison, n = 3, 2 independent repeats).

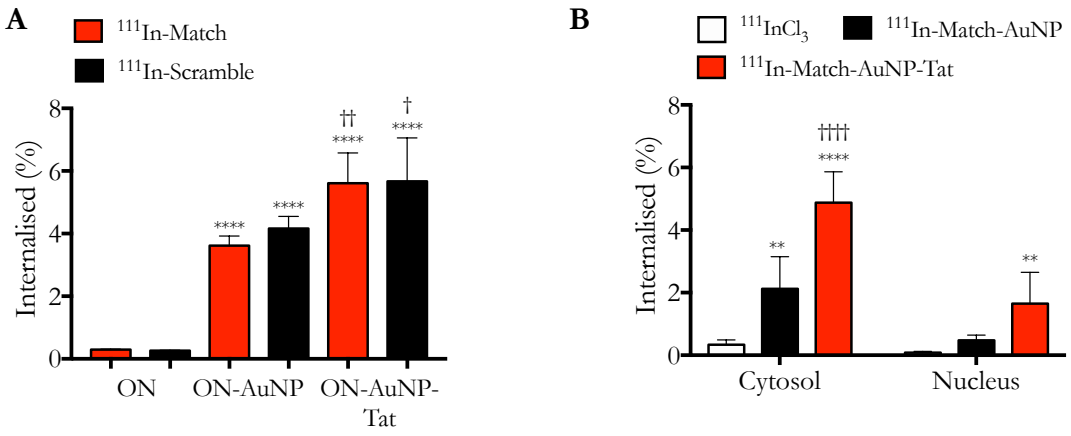


Figure 4.3 Internalisation and fractionation of AuNP constructs after 24 h. A) Internalisation of ON-AuNP and ON-AuNP-Tat. '*': significant difference compared to oligonucleotides (ON); '†': significant difference compared to ON-AuNP. B) Fractionation assays of AuNP, ^{111}In-Match-AuNP and ^{111}In-Match-AuNP-Tat. '*': significant difference with $^{111}InCl_3$; '†': significant difference with ^{111}In-Match-AuNP. One symbol: P < 0.05; Two symbols: P < 0.01, Three symbols: P < 0.001; Four symbols: P < 0.0001.

To further investigate the subcellular distribution of internalised AuNP constructs, fractionation assays were performed (Fig. 4.3 B). It was observed that ^{111}In-Match-AuNP-Tat (4.88 ± 0.99 %) was taken up in the cytosol at a significantly higher rate than ^{111}In-Match-AuNP (2.13 ± 1.03 %) (P < 0.0001), and both were taken up more than $^{111}InCl_3$ (0.34 ± 0.15 %) (P < 0.0001, P = 0.0024, respectively). The nuclear uptake of ^{111}In-Match-AuNP-Tat (1.65 ± 1.00 %) was also significantly higher than $^{111}InCl_3$ (0.08 ± 0.044 %) (P = 0.0071), but no statistical difference was found between the two AuNP constructs (^{111}In-Match-AuNP: 0.48 ± 0.17) in this subcellular compartment (P = 0.06). (Two-Way ANOVA, Multiple Comparison, n = 3, 4 independent repeats).

4.3.2.2 Confocal microscopy

Cy3-labelled oligonucleotides were used to facilitate imaging of AuNP localisation with confocal microscopy. Subsequently, MDA-MB-435 cells were treated with medium only, Match-AuNP, Match-AuNP-Tat, or Match-uAuNP for 2.5 h (Fig. 4.4) or 24 h (Fig. 4.5). After exposure to Match-AuNP for 2.5 h (Fig. 4.4 C, D), several intracellular Cy3 foci were observed in the cells, corresponding to modest cellular uptake. A greater Cy3 signal was seen for Match-AuNP-Tat,

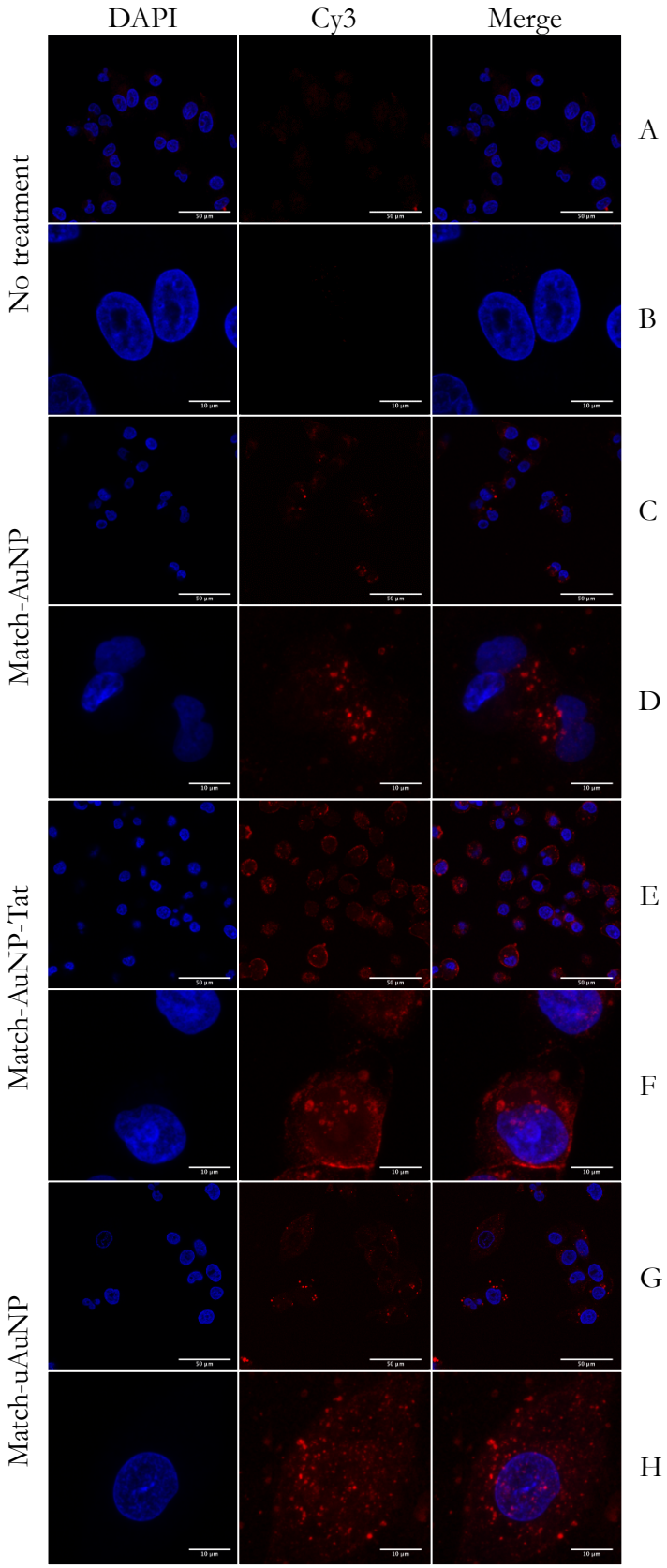


Figure 4.4 Subcellular distribution of AuNP constructs in MDA-MB-435 cells after incubation for 2.5 h. Cells were untreated (A, B) transfected with 500 nM Cy3-Match-AuNP (C, D), 500 nM Cy3-Match-AuNP-Tat (E, F), or 500 nM Cy3-Match-uAuNP (G, H). Images were acquired using a 63 x/1.4 objective lens (A,C,E,G) with an additional 4 x zoom (B,D,F,H). Nuclei were stained with DAPI. Scale bar A,C,E,G is 50 µm, scale bar B,D,F,H is 10 µm.

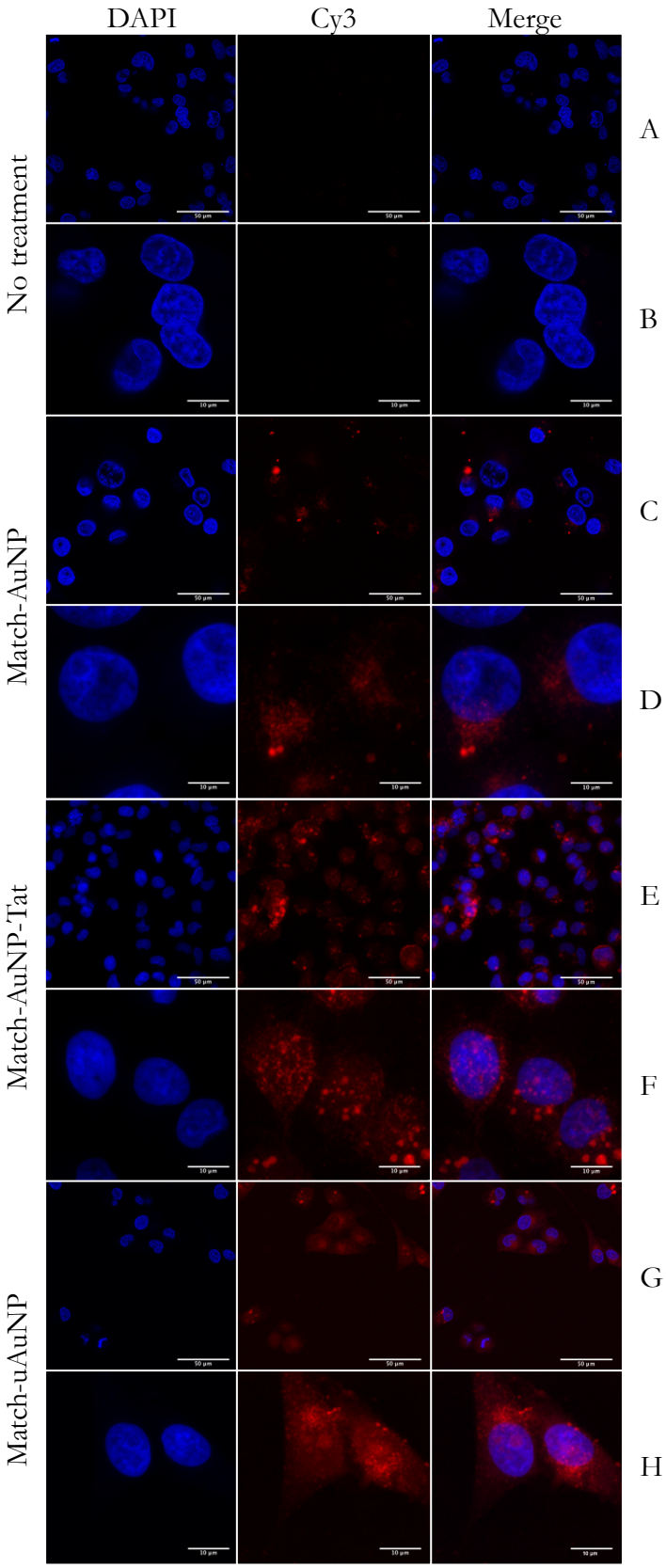


Figure 4.5 Subcellular distribution of AuNP constructs in MDA-MB-435 cells after incubation for 24 h. Cells were untreated (A, B) or transfected with 500 nM Cy3-Match-AuNP (C, D), 500 nM Cy3-Match-AuNP-Tat (E, F), or 500 nM Cy3-Match-uAuNP (G, H). Images were acquired using a 63 x/1.4 objective lens (A,C,E,G) with an additional 4 x zoom (B,D,F,H). Nuclei were stained with DAPI. Scale bar A,C,E,G is 50 µm, scale bar B,D,F,H is 10 µm.

in particular near the cell membrane (Fig. 4.4 E, F). Small foci of fluorescence were also observed in the perinuclear region. Match-uAuNP was observed throughout the cell, including the cytoplasm and nucleus (Fig. 4.4 G, H). After incubation for 24 h, the Cy3-signal in Match-AuNP-treated cells was predominantly in large cytoplasmic foci (Fig. 4.5 C, D). Some perinuclear foci were noted, but no fluorescence was observed in the nucleus. Match-AuNP-Tat-treated cells emitted a high Cy3-signal in the perinuclear region in contrast to the appearance at 2.5 h when the signal was mainly membranous (Fig. 4.5 E, F). Moreover, signal was located in the nucleus. A similar pattern was seen for Match-uAuNP, though the signal was less focal than for Match-AuNP-Tat (Fig. 4.5 G and H).

4.3.2.3 Transmission electron microscopy

To further investigate subcellular distribution, TEM was employed to visualise cells treated for 24 h with Match-AuNP and Match-AuNP-Tat (Fig. 4.6). Figure 4.6 A represents a typical image of the subcellular distribution of Match-AuNP. Black dots (AuNPs) were present in endosomal vesicles in the cytosol (4.6 B and C), consistent with confocal images. Panel B shows a large lysosome-like vesicle that contains several AuNP. Panel C highlights a relatively smaller endosomal vesicle with clustered AuNP. The AuNPs were in most cases individual particles, suggesting that Match-AuNP did not aggregate intracellularly. No particles were observed in the nucleus. Figure 4.6 D shows a representative cell treated with Match-AuNP-Tat. Most particles were located in endosomal vesicles in the perinuclear area (Fig. 4.6 E), but individual particles were also observed in the nucleus (Fig. 4.6 F).

4.3.3 Clonogenic survival

The clonogenic survival of cells exposed to ON-AuNP and ON-AuNP-Tat was evaluated using the linear-quadratic model (n = 4-6, 3 replicate samples per experiment) (Fig. 4.7). MIDs were calculated and are displayed in Table 4.1. ^{111}In-labelled ON-AuNP constructs had no significant impact on clonogenic survival (Fig. 4.7 A). ^{111}In-Match-AuNP, ^{111}In-Scramble-AuNP, Match-

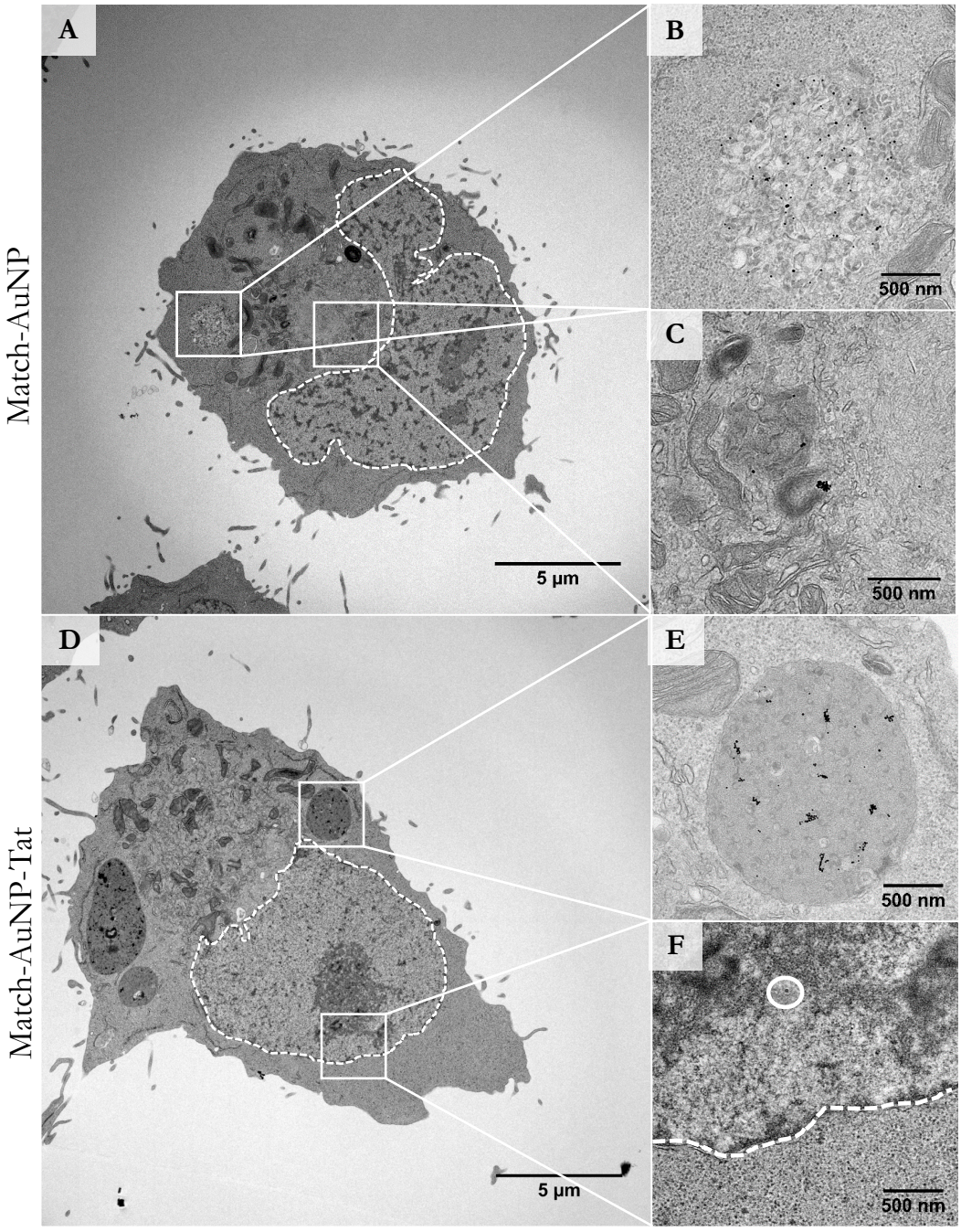


Figure 4.6 Subcellular distribution of AuNPs in MDA-MB-435 cells after incubation for 24 h with TEM. Cells were transfected with 500 nM Match-AuNP (A-C) or 500 nM Match-AuNP-Tat (D-F). A) Whole cell image of Match-AuNP treated cells. B) Lysosome-like vesicle with Match-AuNP. C) Endosomal vesicle with Match-AuNP. D) Whole cell image of Match-AuNP-Tat treated cell. E) Large lysosomal vesicle with Match-AuNP-Tat. F) Nuclear Match-AuNP-Tat.

AuNP, and Scramble-AuNP demonstrated MIDs of 0.21 ± 0.04, 0.18 ± 0.02, 0.21 ± 0.04, and 0.22 ± 0.02, respectively, which did not significantly differ between groups (P = 0.23, One-way ANOVA, Multiple Comparison). In contrast, ^{111}In-Match-AuNP-Tat significantly reduced clonogenic survival ($SF_{210\ nM}$: 0.20 ± 0.11) and displayed a greater cell-killing effect in comparison to ^{111}In-Scramble-AuNP-Tat, indicating a sequence-specific effect of ON-AuNP-Tat (Fig. 4.7 B) (MID: 0.11 ± 0.02 vs 0.15 ± 0.02, P = 0.03, One-way ANOVA, Multiple Comparison). Furthermore, ^{111}In-Match-AuNP-Tat was significantly different from non-radiolabelled controls, which did not display an effect on clonogenic survival (MID: Match-AuNP-Tat: 0.20 ± 0.014 (P = 0.006), MID Scramble-AuNP-Tat 0.22 ± 0.02 (P = 0.002)). ^{111}In-Scramble-AuNP-Tat showed a similar, though less pronounced, difference compared to controls (P= 0.0237 (Match-AuNP-Tat), P = 0.0037 (Scramble-AuNP-Tat). $^{111}InCl_3$, ^{111}In-Match, and ^{111}In-Scramble did not significantly alter clonogenic survival (Fig. 4.7 C). A control

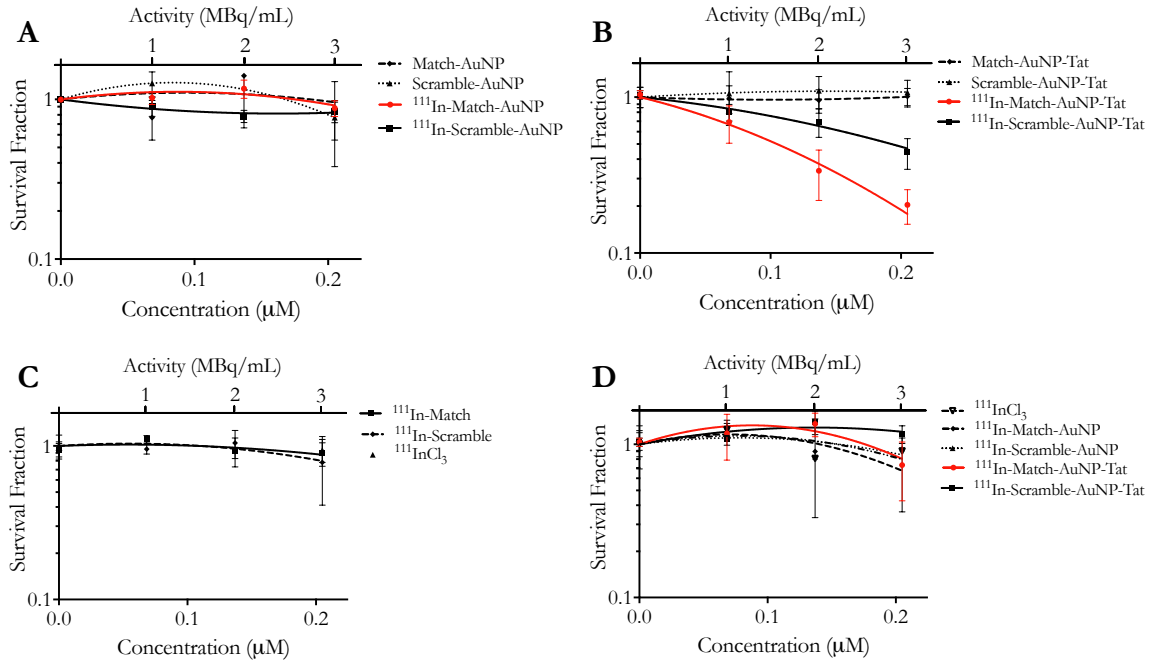


Figure 4.7 Clonogenic survival of cell lines after treatment for 24 h with AuNP constructs. A) Clonogenic survival of MDA-MB-435 cells after treatment with ON-AuNP constructs. B) Clonogenic survival of MDA-MB-435 cells after treatment with ON-AuNP-Tat constructs. C) Clonogenic survival after treatment with $^{111}InCl_3$, ^{11}In-Scramble and ^{111}In-Match. D) Clonogenic survival of U2OS after treatment with radiolabelled ON-AuNP and ON-AuNP-Tat. Curves were plotted using the linear-quadratic model. N = 4-6, 3 repeats per experiment. Data points represent averages ± SEM.

experiment in the non-telomerase expressing cell line U2OS demonstrated a reduction in clonogenic survival following treatment with ^{111}In-Match-AuNP-Tat and ^{111}In-Scramble-AuNP at the highest concentration (SF 0.73 ± 0.53, 1.17 ± 0.26, 0.73 ± 0.37, respectively), but there was no significant difference between groups (Fig. 4.7 D), indicating a telomerase-independent effect. MIDs did not significantly differ from each other.

4.3.4 Radiosensitisation assays

To investigate whether AuNPs and AuNP-mediated inhibition of hTR was sufficient to sensitise cells to external ionising radiation (IR), MDA-MB-435 cells were treated with non-radiolabelled ON-AuNP-Tat, exposed to external beam IR, and assessed in clonogenic survival assays (Fig. 4.8). Cells treated with 210 nM Match-AuNP-Tat plus 2, 4 or 6 Gy IR exhibited a survival fraction of 0.38 ± 0.25, 0.17 ± 0.06, and 0.08 ± 0.04, respectively. Cells treated with

Table 4.1 MIDs and survival fractions for AuNP constructs and controls.

Cell line	Treatment group	MID	Sign.	$SF_{3\ MBq/mL}$
MDA-MB-435	***^{111}In-Match-AuNP***	0.214 ± 0.023	No	0.88 ± 0.24
	^{111}In-Match-AuNP-Tat	0.113 ± 0.023	*, †	0.20 ± 0.11
	$^{111}InCl_3$	0.199 ± 0.018	No	0.94 ± 0.16
	^{111}In-Match	0.202 ± 0.023	No	0.89 ± 0.31
	^{111}In-Scramble	0.198 ± 0.018	No	0.78 ± 0.37
	^{111}In-Scramble-AuNP	0.178 ± 0.020	No	0.84 ± 0.30
	Match-AuNP	0.212 ± 0.041	No	0.84 ± 0.46
	Scramble-AuNP	0.216 ± 0.022	No	0.77 ± 0.21
	^{111}In-Scramble-AuNP-Tat	0.153 ± 0.020	*	0.44 ± 0.20
	Match-AuNP-Tat	0.201 ± 0.014	No	1.01 ± 0.13
	Scramble-AuNP-Tat	0.219 ± 0.025	No	1.07 ± 0.21
U2OS	***^{111}In-Match-AuNP***	0.2339 ± 0.043	No	0.73 ± 0.37
	^{111}In-Match-AuNP-Tat	0.208 ± 0.032	No	0.73 ± 0.53
	$^{111}InCl_3$	0.2058 ± 0.012	No	0.91 ± 0.00
	^{111}In-Scramble-AuNP	0.2453 ± 0.024	No	0.94 ± 0.00
	^{111}In-Scramble-AuNP-Tat	0.214 ± 0.005	No	1.17 ± 0.26

*: significant difference compared to controls. †: Significant difference compared to ^{111}In-Scramble-AuNP-Tat.

Table 4.2 Radiosensitisation and MIDs for Match-AuNP-Tat and Scramble-AuNP-Tat.

Cell line	Treatment group	MID	Sign.	SER
MDA-MB-435	Untreated	3.23 ± 0.56	-	-
	Match-AuNP-Tat	2.02 ± 0.26	Yes	1.60 ± 0.12
	Scramble-AuNP-Tat	3.48 ± 0.66	No	0.93 ± 0.06

Scramble-AuNP-Tat plus IR showed a survival fraction of 0.60 ± 0.43, 0.29 ± 0.17, and 0.12 ± 0.09. For cells that only received 2, 4, 6 Gy IR, a survival fraction of 0.67 ± 0.32, 0.44 ± 0.20, and 0.19 ± 0.19, respectively, was observed. The MID of Match-AuNP-Tat (2.02 ± 0.26) was significantly lower than that of the untreated group (3.23 ± 0.56, P = 0.022) and Scramble-AuNP-Tat (3.48 ± 0.66, P = 0.008). This resulted in a sensitiser enhancement ratio (SER) of 1.60 ± 0.12 for Match-AuNP-Tat and a SER of 0.93 ± 0.06 for Scramble-AuNP-Tat (Table 4.2).

4.3.5 γH2AX assays

To elucidate the effect of treatment with ^{111}In-ON-AuNP-Tat on DNA, MDA-MB-435 and U2OS cells were treated with radiolabelled AuNP constructs or external beam IR, and subsequently stained with antibodies against γH2AX. Differences in treatments were analysed with One-Way ANOVA, Multiple Comparison (n = 65 – 125). A strong γH2AX induction was noted following 4 Gy of IR in MDA-MB-435 cells (foci/NSA: 0.13 ± 0.04 μm^{-2}) (Fig. 4.9 A). No foci were found following immunostaining with a non-specific antibody (data not shown).

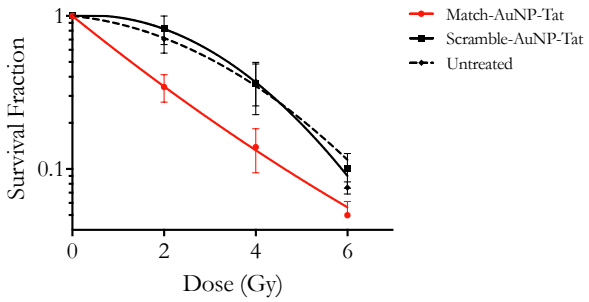


Figure 4.8 Effect of ON-AuNP-Tat on radiosensitivity. ON-AuNP-Tat (210 nM) was added to MDA-MB-435 cells for 24 h prior to exposure to external IR and plated for clonogenic survival. Curves were plotted using the linear-quadratic model. n = 4, 3 repeats per experiment. Data points represent averages ± SEM.

After treatment with medium only, cells displayed 0.07 ± 0.03 μm^{-2} foci/NSA. Treatment with ^{111}In-Scramble-AuNP-Tat caused no increase in the number of foci/NSA (0.07 ± 0.03 μm^{-2}) compared to the control group (P = 0.5701). ^{111}In-Match-AuNP-Tat on the other hand, caused a highly significant upregulation of foci in comparison to untreated control (0.12 ± 0.04 μm^{-2}; P < 0.0001) and ^{111}In-Scramble-AuNP-Tat (P < 0.0001). Furthermore, this number was not significantly different from the 4 Gy treated positive control cells (P = 0.303).

The same assay was performed in the telomerase-negative cell line U20S (Fig. 4.9 B). As with MDA-MB-435, robust expression of foci was observed after treatment with 4 Gy IR (foci/NSA 0.15 ± 0.04 μm^{-2}). No foci were found following immunostaining with a non-specific antibody (data not shown). The positive control (4 Gy IR) showed a significantly higher number of foci than the untreated control (0.10 ± 0.05; P < 0.0001) and ^{111}In-Scramble-AuNP-Tat (0.13 ± 0.04; P = 0.0373), but not ^{111}In-Match-AuNP-Tat (0.13 ± 0.13; P = 0.1057). Both AuNP constructs had a significantly higher number of foci/NSA than the untreated control (^{111}In-Scramble-AuNP-Tat: P = 0.0017; ^{111}In-Match-AuNP-Tat: P = 0.0004) but did not show a difference between each other (P = 0.9818).

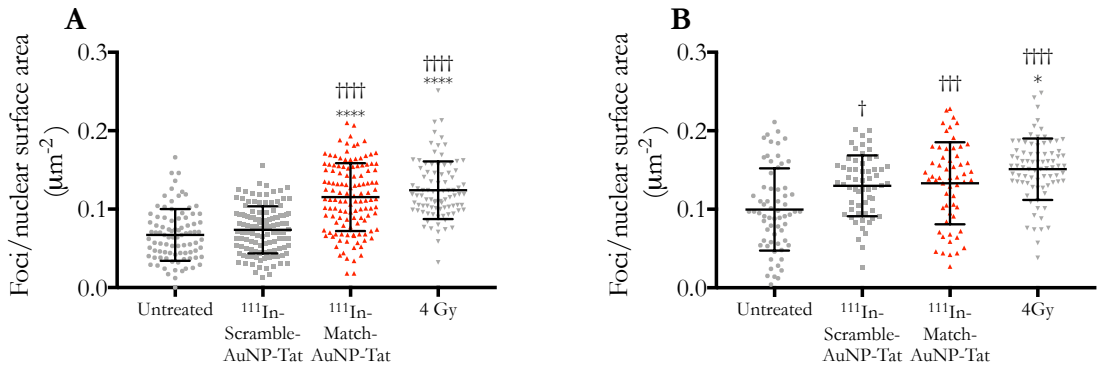


Figure 4.9 γH2AX foci after treatment of A) MDA-MB-435 and B) U2OS cells with ^{111}In-labelled ON-AuNP-Tat. Cells were treated with ^{111}In-ON-AuNP-Tat (210 nM) or control for 24 h before fixation and staining for γH2AX. '†': significant difference with untreated. '*': significant difference with ^{111}In-Scramble-AuNP-Tat. One symbol: P < 0.05; Two symbols: P < 0.01, Three symbols: P < 0.001; Four symbols: P < 0.0001. Bars represent mean ± SD.

4.4 Discussion

Since the discovery of telomerase and the finding that it is expressed abundantly in malignant cells, telomerase-inhibiting strategies have been of great interest to the cancer research community. Several studies have reported that optimal tumour control has been gained when telomerase inhibition is combined with either external beam radiation or chemotherapy (Koziel and Herbert, 2015; Agarwal et al., 2008; Yu et al., 2015; Williams, 2013). It was therefore hypothesised that the combination of telomerase inhibition with TRT can be of therapeutic benefit in the treatment of neoplastic disease. To establish this, ^{111}In-labelled anti-hTR oligonucleotide-functionalised AuNP constructs were synthesised and tested for their anticancer potential *in vitro*.

4.4.1 Dose-dependent inhibition of telomerase by gold nanoparticle constructs

The short-term inhibition of hTR has been a topic of intense research over the past two decades. In correspondence with data found previously by other researchers (Jackson et al., 2018; Waghorn et al., 2017), it was shown that MDA-MB-435 cells have a high expression of telomerase activity, and that this activity can be inhibited by anti-hTR 2'-O-methylation (2'OMe)RNA oligonucleotides in a dose-dependent manner. The $\log IC_{50}$ of -6.93 ± 0.072 was in agreement with the $\log IC_{50}$ described by Jackson et al. (2018) (-6.994 ± 0.056), indicating that the 3' end thiol modification did not significantly alter the affinity of the ligand. Furthermore, the Scramble sequence did not exert an effect in the range 1 – 1000 nM.

After validation of oligonucleotides through comparison to previous results, AuNP were synthesised and tested for their effect on telomerase activity. Initial measurements were hampered due to the quenching effect of AuNPs on fluorescence, so a centrifugation step had to be performed to remove AuNP from the solution prior to plate reader measurements (Dulkeith et al., 2002). Interestingly, the $\text{Log}IC_{50}$ of Match-AuNP (-7.49 ± 0.04) was half a log below free Match oligonucleotide. This is a phenomenon that was observed earlier by Rosi et

al. (2006), who showed that AuNP-bound ASOs against EGFP had a higher affinity for their target than unbound antisense oligonucleotides, and that this affinity increased with oligonucleotide loading density. This effect is described by the cooperative binding model, that defines the interplay between nanoparticle surface density, particle size, interparticle distance, and salt concentration as key parameters in oligonucleotide hybridization (Jin et al., 2003). If the oligonucleotide molecular density is low, complementary binding is non-cooperative and the binding curve obeys the classical Langmuir isotherm. However, when the density is high enough, as occurs on the surface of an AuNP, cooperative binding or hybridisation can occur. Cooperative hybridisation arises because of intermolecular oligonucleotide interactions, such as hydration repulsion, electrostatic repulsion, and osmotic pressure from ions in the ligand shell. The main contributor to cooperative binding is orientational attraction, which reduces free energy by aligning surface-bound oligonucleotides in the same direction, enabling binding of the complementary strand (Lei et al., 2015). Since the result for the TSR8 control demonstrated that the constructs do not interference with the TRAP measurement system, the explanation for the observed increase in affinity being the result of AuNP quenching of the system is ruled out. Scramble-AuNP did not interfere with telomerase activity, and it can therefore be concluded that Match-AuNP inhibits telomerase activity in a sequence-dependent manner, which is likely potentiated by cooperative hybridisation.

Addition of Match-AuNP-Tat resulted in inhibition of the TRAP assay with an even higher affinity ($LogIC_{50}$ -7.99 ± 0.05). However, whereas Scramble-AuNP did not exert an effect on telomerase enzymatic activity, the Scramble-AuNP-Tat induced a dose-dependent reduction in telomerase binding ($logIC_{50}$ -7.39 ± 0.03). This phenomenon was also observed for AuNPs that were loaded with PEG800-SH and Tat only (AuNP-Tat) (data not shown). This result suggested that the AuNP-Tat constructs had a non-specific effect on either telomerase activity or one or more of the components of the TRAP assay. When the TRAP assay was performed in the presence of the pre-elongated positive control, TSR8, there was significant inhibition of the

signal for all Tat-containing AuNP constructs, indicating non-specific assay inhibition by the Tat peptide, rather than non-specific telomerase inhibition. The results of this assay led to the hypothesis that there was an interaction between Tat, which is highly positively charged, and one of components of the reaction mix. This was confirmed by an experiment, in which Tat was added on its own to the reaction mix with TSR8. It was found that the fluorescence signal was again inhibited (data not shown). Interference of the TRAPeze XL assay by compounds is a phenomenon that has been reported in the literature (Piotrowska et al., 2005), and makes the result of the TRAP assay hard to interpret in the presence of Tat. However, it is interesting to point out that the affinity of Match-AuNP-Tat is significantly higher than Scramble-AuNP-Tat. This suggests that Match-AuNP-Tat may have a specific effect on telomerase which is detectable even when the sensitivity of the assay is impaired due to the inhibitory effect of Tat, but this has not been definitively proven. Incidentally, this result provides further evidence that Tat is conjugated to the particle, since it has the ability to interfere with the assay.

One approach to study the effect of this compound further would be to use a modification of the TRAP assay that reduces its proneness to non-specific interference. An option would be to use a method developed by Xiao et al. (2010), who coupled the reaction primers of the TRAP assay to AuNPs, and showed that interference was significantly reduced. It would be interesting to explore this assay for ON-AuNP-Tat to investigate whether it is possible to distinguish the sequence-dependent effect of the oligonucleotides from the non-specific effect of Tat.

4.4.2 Cellular and nuclear uptake of gold nanoparticle constructs

Oligonucleotide delivery for cancer therapy presents two major problems: the first is to deliver the oligonucleotide construct to the right tissue, whilst sparing normal tissue. This is issue will be dealt with in Chapter 5. The second is to deliver the oligonucleotide therapeutic to the right subcellular compartment (Juliano, 2016). Cells can take up unmodified or unconjugated oligonucleotides, but the total uptake is very low, and several delivery strategies have been

developed to overcome this problem (Koller et al., 2011; Juliano et al., 2012). One of these approaches involves the use of AuNP. The uptake of AuNP constructs in cells is a heavily researched field. A complex interplay of factors influences the kinetics of cell entry, including particle shape and size, ligand density and functionality, protein corona, complex charge, and cell type (Dykman and Khlebtsov, 2014). It was recently shown by Choi et al. (2013) that the uptake of spherical oligonucleotide-decorated 10 nm AuNP was initiated via class A scavenger receptors and a lipid-raft-dependent, caveolae-mediated endocytic pathway. After internalisation, nanoparticle endocytosis involves transport via trafficking vesicles to sorting endosomes, late endosomes, and ultimately lysosomes (Canton and Battaglia, 2012).

The dramatic effect that AuNP can have on the cellular delivery of oligonucleotides is illustrated in Fig. 4.3. Both constructs delivered their payload into the cells with a roughly 10 to 20 times higher efficiency than free oligonucleotides. Although Match-AuNP-Tat was internalised significantly more than Match-AuNP, the main difference was found in their fate after internalisation. As shown in Figure 4.4 C and D, Match-AuNP were concentrated in small foci around the cell membrane and in the cytoplasm, consistent with their association with trafficking vesicles. After 24 h, these foci are more prominent, indicating clustering of AuNP in late endosomes and lysosomes, which was confirmed by TEM (Fig. 4.6 A-C). Notably, particles were not observed outside endosomal vesicles in TEM images, which is in agreement with earlier research by Brandenberger et al. (2010).

The addition of PEG800-SH and Tat to the AuNP ligand shell changed the uptake kinetics of the particle markedly. The published literature with regards to the cell entry mechanism of Tat-decorated AuNPs is inconsistent. Investigators have variously described conventional endocytosis with endosomal escape (Nativo et al., 2008), lipid-raft-dependent macropinocytosis (Wadia et al., 2004), and direct translocation over the cell membrane (Lin and Alexander-Katz, 2013). In our study, the internalisation of Match-AuNP-Tat after 2.5 h resulted in the formation

of high density foci, indicating clustering in endosomal vesicles, but a lower continuous signal was also found in the cytosol and nucleus. This was more profound after 24 h, with high density Cy3 focal spots in the perinuclear area, and a more uniform signal through the cytosol and nucleus. On TEM, AuNP dots were found in endosomal vesicles, as well as in the nucleus and cytosol, although this was not to the same extend as was found in confocal studies or the fractionation assay (Fig. 4.3 B). A similar phenomenon was observed by de la Fuente and Berry (2005), although the AuNPs used had a smaller diameter than those in this study (2.4-8.2 nm). Furthermore, Nativo et al. (2008) found that AuNP loaded with PEG-SH, Tat and two other NLS exhibited a distribution pattern around the nucleus after internalisation. The investigators suggested that the accumulation of Tat-functionalised AuNPs in unusual perinuclear membranous structures is the result of the disruption of the endosomal membrane. Although our study also found perinuclear accumulation, TEM revealed no evidence of endosomal disruption.

The high nuclear uptake that was found in the fractionation assay for Match-AuNP-Tat (1.65 ± 1.00% of total added radioactivity), and to a lesser extent for Match-AuNP (0.48 ± 0.17%), is not fully reflected in the TEM images. Although there is clear optical nuclear uptake of AuNPs, it seems that the uptake percentage does correlate between both experiments. We developed two hypotheses to explain this. In the first place, since the fractionation assay measures the location of the oligonucleotide, and TEM the location of the AuNP, the discrepancy in the relative nuclear uptake may be caused by intracellular oligonucleotide-detachment from the AuNP surface, resulting in free cytosolic and nuclear anti-hTR oligonucleotides, that can readily enter the nucleus, whereas AuNP remains predominantly cytosol-bound. This view is supported by confocal images, which also rely on oligonucleotide imaging via Cy3, and show a subcellular distribution which corresponds with the results of the fractionation assay. The possibility of oligonucleotide-dissociation as a result of intracellular glutathione, an abundant antioxidant involved in various redox reactions in the cell, was raised

by Rosi et al. (2006). It can reduce thiol bonds formed between oligonucleotides and AuNP by serving as an electron donor, and may therefore be the underlying cause of the observed phenomenon.

A second explanation may be that the results of the fractionation experiment are erroneous due the centrifugation steps that are involved in the separation of the different fractions, resulting in accumulation of nanoparticles in the lower, nuclear fraction. The centrifugal speed of 500 g is low, but it can't be excluded as a factor, since AuNP are relatively heavy constructs. Some fractionation studies performed with radiolabelled nanoparticles by others have used centrifugation speeds that exceeded this speed greatly (3000 g), and reported high nuclear uptake (Lee et al., 2010). At these speeds, nanoparticles may be spun down in to the nuclear fraction, and therefore the observed results may be inflated. In our scenario, it may mean that the results are overstated in comparison to the TEM and confocal microscopy images, but since Match-AuNP and Match-AuNP-Tat have a molecular weight in the same range, this may not explain the difference between the two constructs.

Besides the two core constructs described in this thesis (Match-AuNP and Match-AuNP-Tat), confocal images were acquired for Match-uAuNP. These images show that size can have a profound effect on the subcellular distribution of NPs and has an obvious effect on nuclear localisation after 2.5 and 24 h, as shown previously by Huo et al. (2014). However, both Cy3-labelled Scramble- and Match-uAuNP resulted in high cell kill (data not shown). Because of the non-specific mechanism of cell kill, as well as the difficulties with synthesising a single radiospecies (Chapter 3), the development of this particle was halted. Reducing the size of AuNP constructs is, however, still a viable option to change *in vitro* and in vivo kinetics, and further recommendations with regards to the use of ultra-small AuNP (2-4 nm) will be made in Chapter 6.

4.4.3 ^{111}In-Match-AuNP-Tat induces cytotoxic DNA double-strand breaks

Radiosensitisation by hTR inhibition is the topic of debate in literature, and several potential mechanisms have been described. These mechanisms are reviewed in Chapter 1 and will be linked to the results of this study in Chapter 6. In this section, the discussion will focus on the strengths and limitations of the experiments, the relationship between subcellular distribution and cytotoxicity, and the comparison of the data with results from previous studies.

Jackson et al. demonstrated that ^{111}In-labelled anti-hTR oligonucleotides have a telomerase-specific anti-proliferative and cytotoxic effect via the induction of DNA DSBs in three telomerase-positive cell lines. In line with this, ^{111}In-Match-AuNP-Tat had a significant, dose-dependent effect on the reduction of clonogenic survival of MDA-MB-435 cells. ^{111}In-Scramble-AuNP-Tat also led to a reduction in proliferative capacity, although this construct was significantly less effective. The effect of the latter compound is likely the result of the nuclear importation of radiotoxic ^{111}In. The difference in effect between ^{111}In-Match-AuNP-Tat and ^{111}In-Scramble-AuNP-Tat can be explained by the difference in oligonucleotide sequence in the ligand shell of the two constructs and is consistent with targeting telomerase. Crucially, there is no effect difference between sequences in cells that don't express telomerase. Furthermore, when these constructs are non-radiolabelled, they have a minimal effect on clonogenic survival when treated for this time duration, which is in line with previous research (Chen et al., 2003; Gellert et al., 2006; Hochreiter et al., 2006). Chen et al. reported that a treatment time of two weeks was enough to exert a telomerase-specific effect on clonogenic survival. Interestingly, this time would be too short to induce critical telomere shortening, indicating a potential for a non-canonical effect of telomerase. This correlates with the direct induction of DNA damage observed in this study, which is proposed to be the cause behind the reduction in clonogenic survival.

In this research, we show a correlation between the cytosolic and nuclear uptake of particles and their capacity to reduce clonogenic survival of the telomerase-positive cell line MDA-MB-435. Both Match-AuNP and Match-AuNP-Tat inhibit telomerase activity in a cell-free system, but only ^{111}In-labelled Match-AuNP-Tat has a significant and telomerase-specific effect on clonogenic survival. There is a discrepancy in the subcellular distribution of both constructs, which is hypothesised to be the result of the difference in ligand shell. For the constructs to inhibit the hTR, they must reach the nucleus. Furthermore, the effect of ^{111}In is most profound in an 11 nm range from the DNA (Falzone et al., 2015). Since Match-AuNP-Tat is present in the nucleus at higher concentrations than Match-AuNP, this may be a likely explanation for the greater reduction in clonogenic survival.

To further investigate the apparent radiosensitising effect that was observed in the clonogenic survival experiments, cells were incubated with non-radiolabelled Match-AuNP-Tat and Scramble-AuNP-Tat and exposed to increasing doses of external beam radiation. The result of this experiment showed a SER for Match-AuNP-Tat of 1.6, which is in line with results earlier recorded by Wu et al. (2017). Wu et al. showed that treatment with imetelstat prior to irradiation of Kyse410 and Kyse520 cells led to SERs of 1.9 and 1.6, respectively. However, whereas Wu et al. pre-treated cells for 40 days prior to irradiation, our results suggest that a 24 h treatment is sufficient to elucidate a similar effect, further establishing the hypothesis that telomere shortening is not the sole explanation of hTR inhibition-induced radiosensitisation.

In this experiment, Scramble-AuNP-Tat did not cause a significant effect, demonstrating that 15.5 nm AuNP did not radiosensitise cells in their own right. Initially, this seems to be discordant with the literature, since various studies have shown that these particles can sensitise cells to radiation (Cui et al., 2017). On closer inspection, however, the relatively low energy of the beam (661 keV) from the available ^{137}Cs source may only lead to the Compton effect, a process that occurs for AuNP with photons of energy between 0.5 and 1.02 MeV. This means

that the energy of an incident photon is partly absorbed by an electron in the outer shell of an atom in the AuNP, and the additional energy is emitted as relatively harmless photons. To cause more harm, the energy of an incident photon must be greater than 1.02 MeV to result in pair production, which leads to full absorption of the energy by atomic nuclei, subsequently causing emission of a cytotoxic pair of electrons and positrons (Cui et al., 2017). External beam photons of this and higher energy are more frequently used in the clinical setting, and it is therefore recommended to test the compounds in a set up where higher photon energies can be generated. Besides this difference, it is shown that the concentrations of AuNP used to treat these cells was roughly 10-fold higher than the concentrations used in our studies (Wang et al., 2015). It is therefore possible that the radiosensitising effect of AuNP would become more profound at a higher photon energy beam and Scramble-AuNP-Tat concentration.

The combined data of a sequence-specific and radiolabel-dependent effect leads to the suggestion that short-term hTR inhibition results in sensitisation to the radiotoxic effects of Auger electrons from ^{111}In and 661 keV photon irradiation. In agreement with this, we observed a strong upregulation of γH2AX foci after treatment with ^{111}In-Match-AuNP-Tat, but not after treatment with ^{111}In-Scramble-AuNP-Tat in telomerase-positive cells. Furthermore, there was a modest upregulation of γH2AX foci in telomerase-negative cells, but this was sequence independent, and likely the result of intranuclear ^{111}In. The results shown here are in accordance with previously recorded results by Jackson et al, who found that treatment with transfected ^{111}In-Match led to the dose-dependent induction of γH2AX foci in MDA-MB-435 cells. These results suggest that ^{111}In-Match-AuNP-Tat either causes more DNA DSBs than ^{111}In-Scramble-AuNP-Tat or inhibits the repair of such damage in telomerase-positive cells. In Chapter 6, suggestions for further research on this topic will be proposed.

4.4.4 Concluding remarks

In this chapter, promising steps have been made towards the realisation of an AuNP construct for the delivery of ^{111}In-labelled hTR-targeting oligonucleotides. AuNP constructs functionalised with a multivalent ligand shell of PEG800-SH, Tat and ^{111}In-labelled oligonucleotides exhibited a superior subcellular distribution profile in comparison to AuNP constructs with a monovalent ligand shell of ^{111}In-labelled oligonucleotides. The reduction in clonogenic survival caused by ^{111}In-Match-AuNP-Tat was sequence- and telomerase-dependent, underlining the potential as a specific anticancer agent. Match-AuNP-Tat was demonstrated to be a radiosensitising agent with a SER of 1.6. Despite ambiguous TRAP assay results, ^{111}In-Match-AuNP-Tat was considered more promising than ^{111}In-Match-AuNP and was therefore taken forward to *in vivo* biodistribution studies (Chapter 5).

CHAPTER 5. *IN VIVO* ASSESSMENT OF GOLD NANOPARTICLE RADIOPHARMACEUTICALS

5.1 Introduction

The *in vivo* characterisation of Match-AuNP-Tat, with an emphasis on ultrasound-mediated tumour delivery, is presented in this chapter. ON-AuNP-Tat was evaluated by SPECT (^{111}In-labelled) and IVIS (Cy5-labelled), as well as in an *in vitro* agarose gel-based water bath that is designed to simulate ultrasound-mediated extravasation (Chapter 2.8). The results of this chapter provide a stepping stone for further *in vivo* development of AuNP-based radiopharmaceuticals.

5.1.1 In vivo delivery of gold nanoparticles

There has been much interest in harnessing the potential of nucleic acid-based therapeutics for the treatment of malignant conditions (Juliano, 2016). However, when administered via the blood stream, unmodified naked RNA can be degraded by serum nucleases and can trigger a response by the innate immune system (Layzer et al., 2004; Heil et al., 2004; Forsbach et al., 2008). Furthermore, due to the high solubility and small size of most oligonucleotides, they are cleared rapidly from the blood stream via the kidneys (Huang et al., 2011). Therefore, unaltered oligonucleotides must be modified or linked to carriers to reach their intended site of action. Ideally, carriers will protect oligonucleotides against serum nucleases, to avoid recognition by the immune system and non-specific interaction with serum proteins and non-targeted cells, to reduce the rate of renal clearance and to enable tumour uptake and cancer cell internalisation (Kanasty et al., 2013).

Nanoparticle-based delivery systems have emerged as fitting carriers to overcome the pharmacokinetic limitations that are associated with conventional oligonucleotides. Nanoparticles, such as AuNP, can be beneficial since they prolong oligonucleotide circulation

time and improve tumour uptake via the enhanced permeability and retention (EPR) effect (Blanco et al., 2015). EPR results from differences in the vasculature between most normal tissues and that of tumours. Whereas normal tissue is vascularised by capillaries with tightly sealed endothelium, the tumour-associated capillaries have fenestrations in the endothelial lining, resulting in relatively large pores (0.1-3 μm). This difference causes an increased vascular permeability and hydraulic conductivity, which can be exploited for nanoparticle therapy (Nakamura et al., 2016). The first to demonstrate the potential of this effect were Matsumura and Maeda in 1986, who showed that nanoparticles were able to extravasate through the leaky vasculature and reach the tumour space.

However, recent reports indicate that drug delivery resulting from the EPR effect is relatively limited in most tumours, since the vessel leakage rate is slow and the nanoparticulate formulation may either be excreted or sequestered by clearance organs before therapeutic accumulation takes place. Indeed, it has been demonstrated that the EPR effect provides less than a 2-fold increase in delivery to tumours compared to normal organs, which is in general insufficient for a clinically relevant effect on the tumour (Nakamura et al., 2016). However, this number is an average, and various studies have demonstrated higher uptake levels, including a study from our group (Song et al., 2017). For this reason, we hypothesised that ^{111}Match-AuNP-Tat may have an advantageous pharmacokinetic profile.

To test this, a murine xenograft model of the cell line MDA-MB-435 was generated. These mice were injected with a therapeutic dose of radiolabelled AuNP constructs and imaged using a SPECT scanner. SPECT is a versatile nuclear medicine tomography technique that uses γ-rays to provide information about the localisation and concentration of γ-emitting radionuclides, such as ^{111}In. SPECT imaging is a useful technique to determine the pharmacokinetics and tumour uptake of experimental drugs, as well an excellent tool for the determination of clinical effects (Bailey and Willowson, 2013). In the experiments described here organs were harvested

for the determination of organ distribution of radioactivity by gamma-counter following the last imaging session.

5.1.2 Ultrasound-mediated drug delivery

Several techniques have been established to enhance nanoparticle tumour uptake. An interesting development in the past decade has been the use of ultrasound to activate cavitation agents for nanomedicine tumour delivery through biological barriers (Zhang et al., 2016b; Mo et al., 2012). Cavitation agents can be used for direct delivery via the incorporation of drugs in their ligand shell/core, or indirectly through the use of released cavitation forces to open up biological barriers. The prototypical cavitation agent is a microbubble, a 1 – 5 μm-sized gas-filled vesicle that is stabilised by a ligand shell of phospholipids, polymers or proteins (Dasgupta et al., 2016). Mechanical stimuli, such as ultrasound, can compress microbubbles, which results in oscillation (stable cavitation) or implosion (inertial cavitation) (Fig. 5.1 A). Stable cavitation results in effects on the endothelial layer and blood content, such as push/pull and radiation force processes, as well as microstreaming. Inertial cavitation causes more forceful events, such as microjet and shockwave formation. These phenomena can be exploited to deliver drugs at a selected site, such as a tumour. This active form of transport over the endothelial layer has provided higher and more rapid levels of tumour accumulation of therapeutics than the EPR effect alone (Dasgupta et al., 2016). Several researchers have exploited this phenomenon for delivery of nanoparticles, such as polymers (Zhang et al., 2016; Mo et al., 2012), AuNP (Mo et al., 2015) and liposomes (Graham et al., 2014). Particularly relevant to the work in this thesis is the study by Mo et al., in which ultrasound-activated cavitation agents and nanoparticle clusters led to a significant improvement in tumour uptake of AuNP modified-adenoviruses. For this reason, it was hypothesised that cavitation agents may improve the tumour delivery of Match-AuNP-Tat.

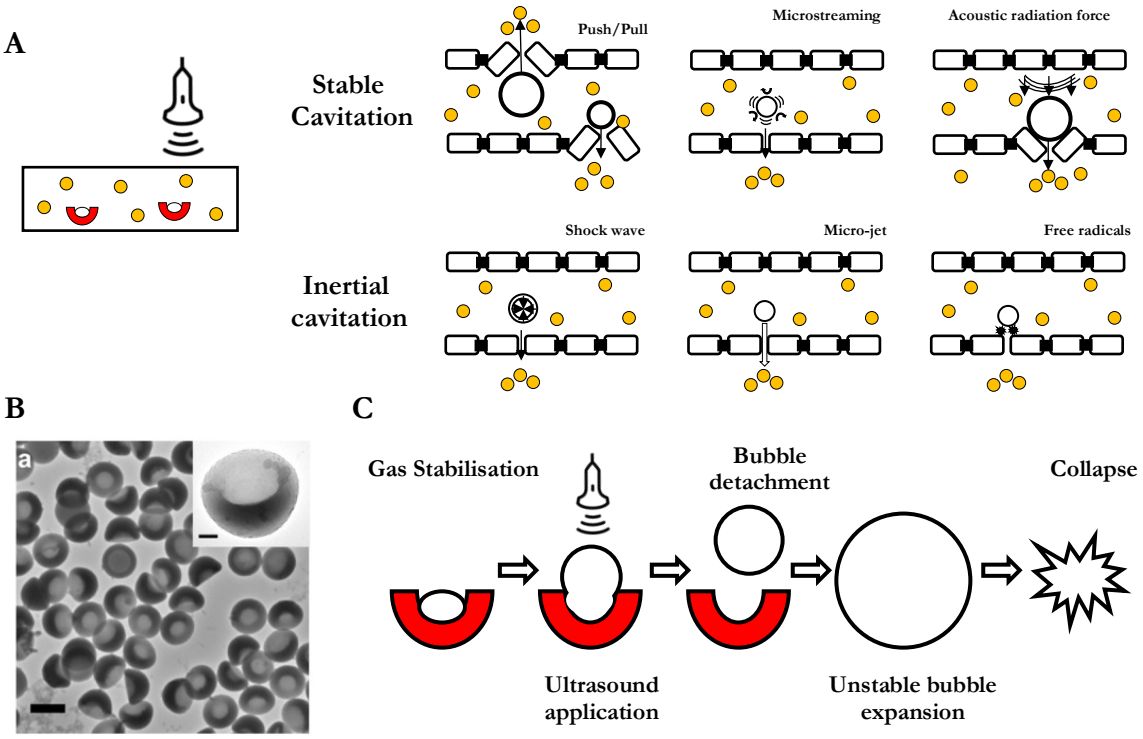


Figure 5.1 Ultrasound-mediated drug delivery. A) A schematic representation of the biophysical mechanisms that contribute to blood vessel permeabilisation after ultrasound application with cavitation agents. Activation by ultrasound can lead to stable and inertial cavitation of cavitation agents. Stable cavitation can lead to push (rarefaction) and pull (compression) effects, which can open up the membrane. It can also result in microstreaming, which is the result of rapid expansion and contraction of the cavitation agent. The created vortical bulk fluid flow can result in shear stress on the endothelial membrane causing sonoporation and nanoparticle extravasation. Third, acoustic radiation forces can displace cavitation agents towards the endothelial layer, which can permeabilise it by pushing and massaging. When acoustic pressure reaches a threshold, inertial cavitation occurs with significant frequency-independent expansion, followed by a collapse. This collapse leads to the generation of shock waves and microjets that can propel nanoparticles into the tumour. Furthermore, it can result in the formation of free radicals, which can permeabilise the endothelial layer to let through nanoparticles. B) TEM image of nanocups (Scalebar: 500 nm, Inset scalebar: 100 nm). Image adapted with permission from Kwan et al. (2015). C) Nanocup activation as a result of ultrasound exposure. The rarefactional pressure phase of the ultrasound wave leads to nanobubble growth and detachment. After release, the bubble expands uncontrollably until the compressional phase of the ultrasound, which results in bubble collapse.

However, progress with conventional microbubbles has been impeded by their short half-life and lability under ultrasound exposure, requiring repeated injections or continuous infusion to be effective (Kwan et al., 2015). To mitigate the short half-life and lability, a next generation of cavitation agents has been developed (Fig. 5.1 B, C) (Kwan et al., 2015).

Nanocups are polymeric 'cup' shaped nanoparticles that are able to stabilise gas on their surface. They are composed of a hydroxyethylmethyl methacrylate (HEMA) and methyl methacrylate (MMA) copolymer bound to a poly(styrene-co-divinylbenzene) (DVB) copolymer core in a 10:1:6 ratio (MMA:HEMA:DVB) that is formed around a 300 nm polystyrene bead (Kwan et al., 2015). Nanocups can sustain cavitation activity for a prolonged time (several minutes) after triggering by therapeutic ultrasound systems or diagnostic transducers. Nanocups are designed to entrap a nanobubble on their surface that can detach and collapse after ultrasound exposure, resulting in the phenomena described in Fig. 5.1 A.

To measure the effects of these particles in combination with Match-AuNP-Tat, *in vitro* and *in vivo*, experimental techniques designed at IBME were used (Chapter 2.8-2.9). The agarose gel model is an established model that can measure the potential of nanocups to propel AuNP constructs into tissue. By labelling the particles with a fluorophore, such as Cy5, the transit of NPs into the agarose medium can be imaged to give a qualitative and quantitative output on cavitation agent mediated delivery (Mannaris et al., 2018). For *in vivo* delivery, a cone set-up for delivery of US, similar to a previously described method by Bhatnagar et al. (2016), was used. The system allows for ultrasound delivery via a cone applied to the tumour site via ultrasound-transducing coupling gel, allowing for nanocup activation. The effect can be imaged by IVIS in the case of fluorescently labelled nanoparticles, or by SPECT in the case of radiolabelled particles.

5.1.3 Aims and outline

The aim of the studies described in this chapter was to test the biodistribution and tumour uptake of ^{111}In-labelled anti-hTR oligonucleotide-decorated AuNPs with and without ultrasound-activatable cavitation agents. AuNP constructs were tested in MDA-MB-435 xenografts and analysed by SPECT, IVIS images and gamma-counter measurement of radioactivity.

5.2 Methods

For methods, see Chapter 2.7 – 2.9.

5.3 Results

5.3.1 Xenograft model

The MDA-MB-435 cell line was used to generate xenografts in female athymic nude mice to test the tumour-targeting potential of ^{111}In-Match-AuNP-Tat and ^{111}In-Scramble-AuNP-Tat. Following subcutaneous injection, tumour volume measurements were performed over eight weeks to assess the growth pattern (Fig. 5.2). All mice developed visible tumours within ten days after MDA-MB-435 inoculation. Growth rate was linear for most mice from day 10 (1.2 ± 0.1 GMD/day), although outliers grew faster/slower tumours. No signs of distress or weight loss were recorded during xenograft development.

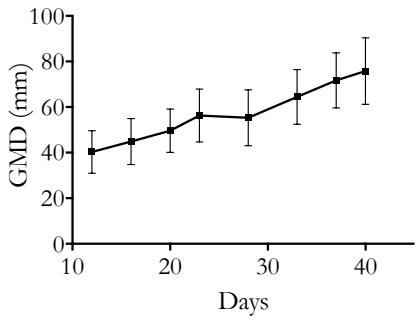


Figure 5.2 Tumour growth curve of MDA-MB-435 xenografts. Female athymic nude mice received subcutaneous inoculations of MDA-MB-435 cells, and tumour volume measurements were acquired over 40 days. Data points represent the mean ± SD (n = 10). GMD = geometric mean diameter.

5.3.2 In vivo and ex vivo biodistribution of ^{111}In-Match-AuNP-Tat

MDA-MB-435 xenograft bearing mice were injected with 10 MBq (15 MBq/nmol oligonucleotides) ^{111}In-Match-AuNP-Tat and ^{111}In-Scramble-AuNP-Tat and imaged by SPECT 24, 48 and 72 h post-injection (p.i.) (Fig. 5.3 A). A strong signal was observed in the liver from 24 hours onwards, indicating AuNP particle uptake by the RES system. Further accumulation was found in the anatomical region of the spleen, as well as in the bladder and to a lesser extend in the bones. No tumour uptake was measured, even after gating at the tumour to increase sensitivity (data not shown). After 72 hours, mice were sacrificed, and organs were harvested for measurement by gamma-counter (Fig. 5.3 B, C). This analysis confirmed results observed by SPECT. Tumour uptake was low: less than 0.1% of the administered nanoparticles accumulated in the tumour (^{111}In-Match-AuNP-Tat: 0.07 ± 0.01; ^{111}In-Scramble-AuNP-Tat: 0.09 ± 0.02 %I.D./g) (Fig. 5.3 C). A high concentration of both ^{111}In-Match-AuNP-Tat and ^{111}In-Scramble-AuNP-Tat was found in the liver (39.75 ± 2.61 and 38.58 ± 7.04 %I.D./g, respectively) and the spleen (8.33 ± 0.31, 7.37 ± 0.51 %I.D./g, respectively). Interestingly, little activity was found in the kidneys (< 0.5 %I.D./g), and combined with high liver sequestration, this result indicated that ^{111}In-Match-AuNP-Tat and ^{111}In-Scramble-AuNP-Tat were cleared hepatically. No significant accumulation was observed in other organs. Since a very low percentage of Match-AuNP-Tat and Scramble-AuNP-Tat was found in the blood (< 0.03 %I.D./g) and heart (< 0.01 %I.D./g) at 72 h, it can be concluded that complete blood clearance occurs within this timespan. No significant differences were found in the uptake pattern of the two AuNP constructs, suggesting equivalent pharmacokinetic properties.

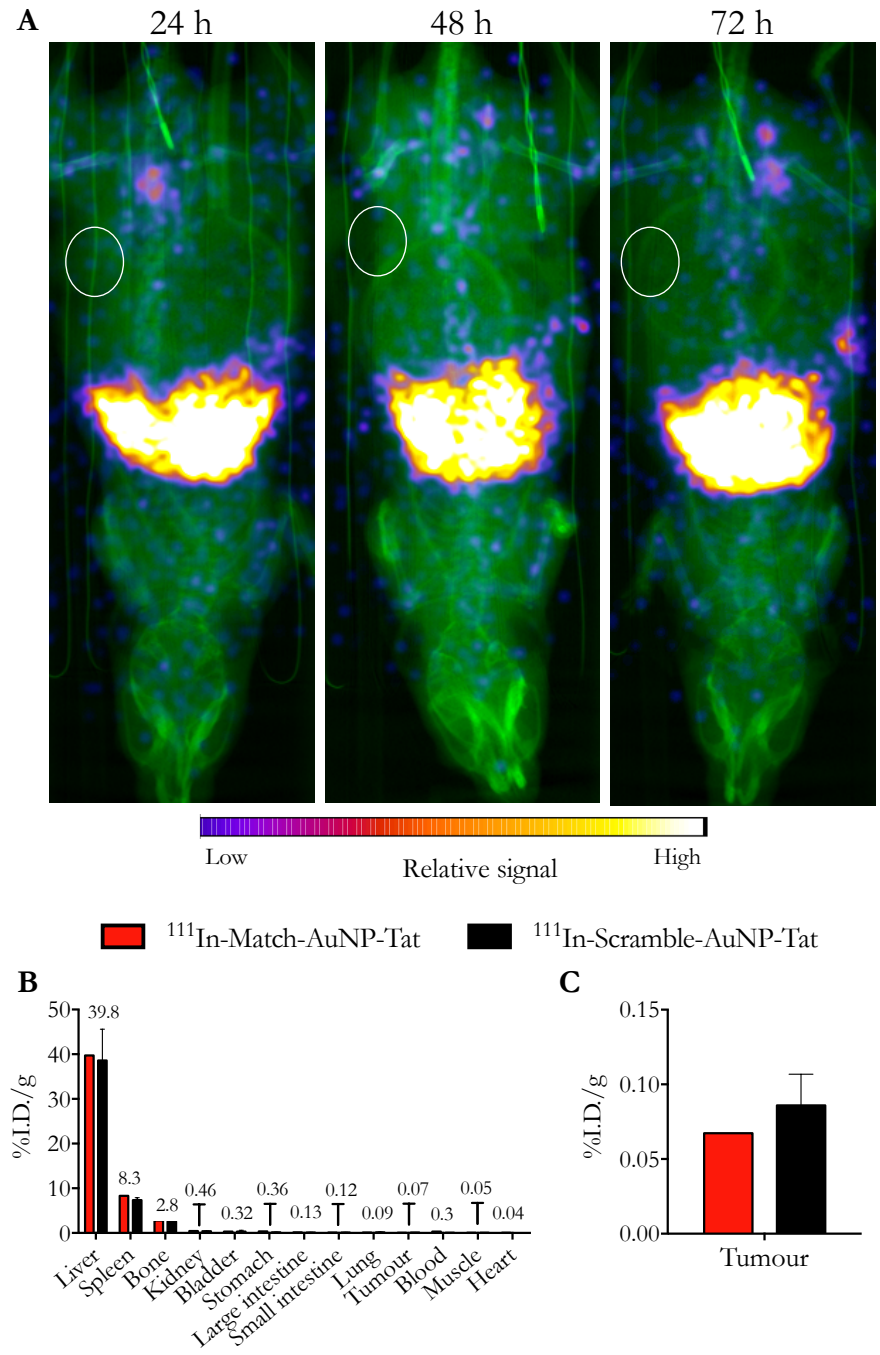


Figure 5.3 SPECT imaging and ex vivo biodistribution of ^{111}In-ON-AuNP-Tat. A) Whole-body SPECT showing biodistribution of ^{111}In-Match-AuNP-Tat in MDA-MB-435 xenografts. Images of the same mouse acquired at 24, 48 and 72 hours p.i. are shown and are representative of the cohort. B + C) Ex vivo analysis was performed 72 h post-injection. The amount of radioactivity in selected tissues/organs (B) and tumours (C) was measured and data expressed as %I.D./g. Error bars represent mean ± SD (n=3/group). Numbers above bars indicate the average of ^{111}In-Match-AuNP-Tat. A Two-Way ANOVA was performed: there was no statistically significant difference between ^{111}In-Match-AuNP-Tat and ^{111}In-Scramble-AuNP-Tat. %I.D./g: Percentage of the injected dose per gram of tissue.

5.3.3 In vitro ultrasound-mediated delivery of gold nanoparticle constructs

To mitigate the low tumour uptake of AuNP constructs, the use of ultrasound-activatable nanocups was tested *in vitro* for their potential to propel Cy5-Match-AuNP-Tat into a tissue-surrogate, agarose gel (Fig. 5.4). Figure 5.4 A showed that when Cy5-Match-AuNP-Tat flowed through an agarose gel channel without ultrasound or nanocups, very limited extravasation was observed. Similarly, there was minimal transit of Cy5-Match-AuNP-Tat into the agarose medium when ultrasound was applied to Cy5-Match-AuNP-Tat alone or to Cy5-Match-AuNP-Tat plus inactivated nanocups (iNC). However, when ultrasound was applied to a mixture of Cy5-Match-AuNP-Tat and nanocups (NC) a significant increase in peak penetration depth <.0001) (Fig. 5.4 C) is observed in comparison to the control groups. This is accompanied by a high but variable mean cavitation power (0.8003 ± 2.568) (Fig. 5.4 D).

5.3.4 IVIS detection of gold nanoparticle constructs

To test the detection limit of the IVIS system for AuNP, 0.5% and 1% of the anticipated injected dose for *in vivo* ultrasound experiments was injected directly into MDA-MB-435 xenograft tumours. These amounts of AuNP were selected to reflect the predicted range of tumour uptake following systemic administration. It was found that both injected quantities of AuNP were readily detected by IVIS in a relatively linear fashion (0.5% I.D.: 4.6 a.u. vs 1% I.D.: 11.7 a.u) (Fig. 5.5). Tumours were extracted and disaggregated, and fluorescence was measured by plate reader (data not shown). However, it was found that there was no linear correlation, and this measure was therefore discarded as a quantification method.

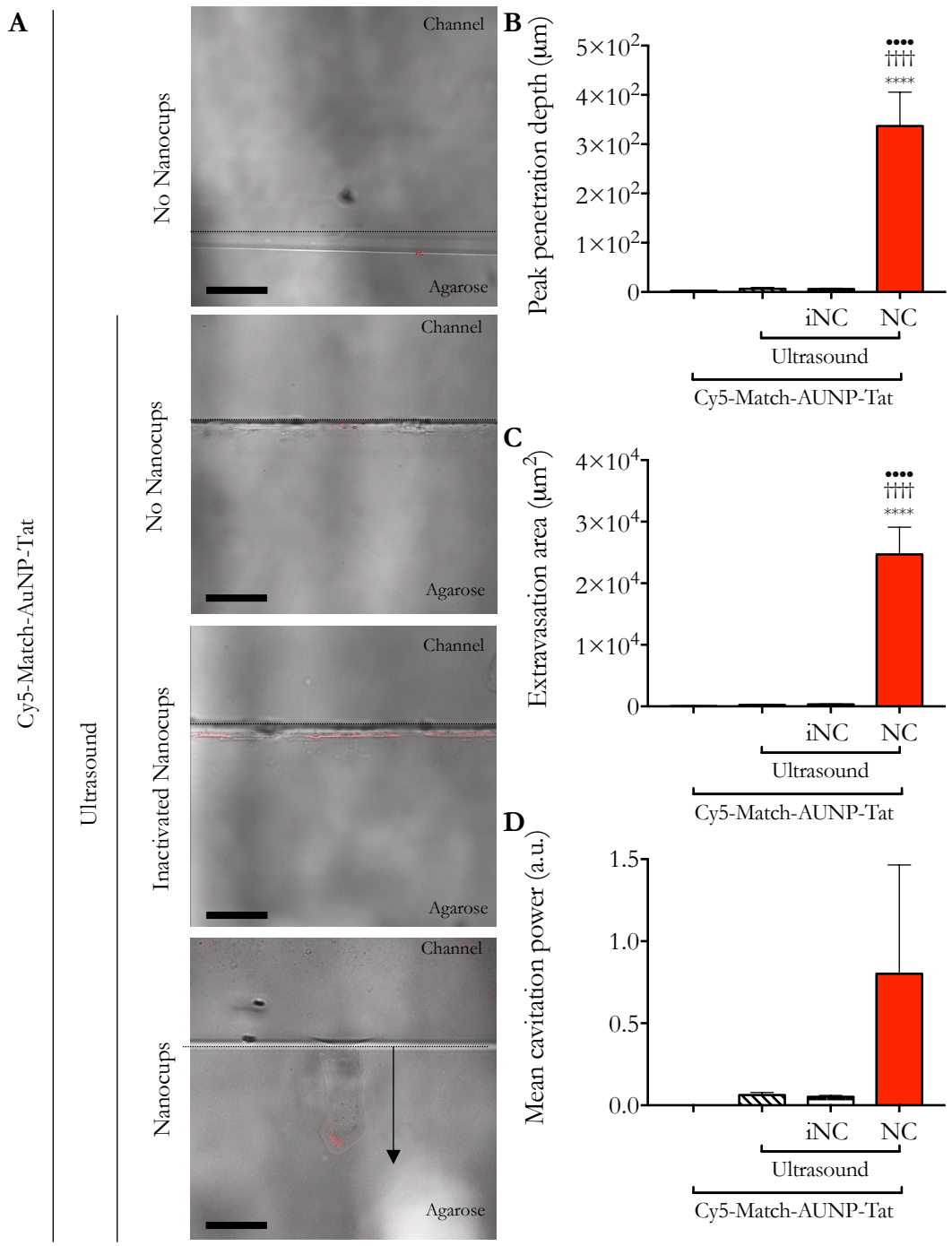


Figure 5.4 *In vitro* ultrasound-mediated extravasation of Cy5-Match-AuNP-Tat. A) Confocal microscopy images of agarose gel channels with different treatment regimens. The scale bar represents 100 µm. B) Peak penetration depth in agarose gel after treatment with and without ultrasound. C) Extravasation area in in agarose gel after treatment with and without ultrasound. D) Mean cavitation power in the channel as measured by PCD. Bars represent mean ± SEM. Data is based on n = 5-12 confocal images. Data were compared using One-Way ANOVA, multiple comparisons. US: ultrasound. ●: Significant difference with Cy5-Match-AuNP-Tat. †: Significant difference with Cy5-Match-AuNP-Tat and ultrasound. *: Significant difference with Cy5-Match-AuNP-Tat, ultrasound and iNC. Four symbols represent P < 0.0001. (In collaboration with H. Lea-Banks)

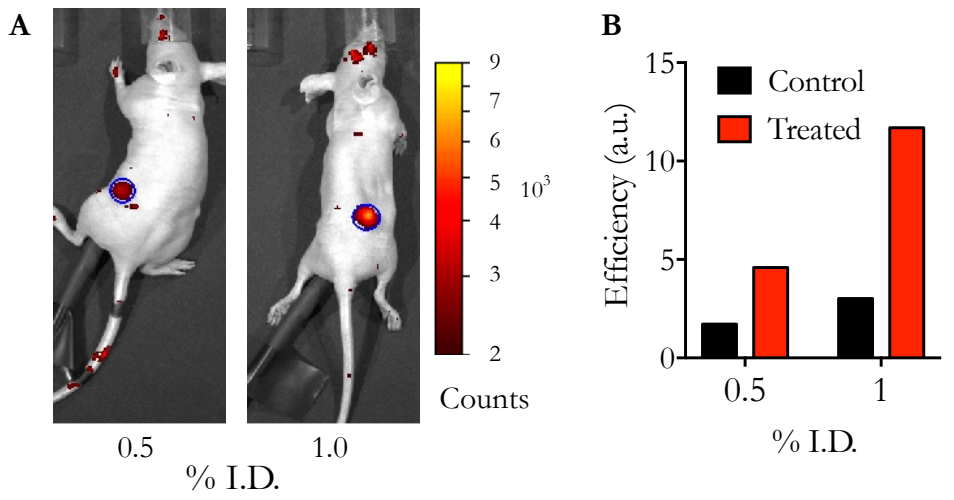


Figure 5.5 ***In vivo*** **Cy5-Match-AuNP-Tat detection with IVIS. A) IVIS images of MDA-MB-435 xenograft-bearing mice following intratumoural injection of Cy5-Match-AuNP-Tat (0.5% and 1% of the amount of AuNP to be used for intravenous delivery). B) ROI measurements of the efficiency of injected and control tumour for 0.5% and 1% of the intravenous I.D. Cy5-Match-AuNP-Tat. Bars represent the ROI of each mouse. (n=1).**

5.3.5 In vivo ultrasound-mediated delivery of gold nanoparticle constructs

After the successful *in vitro* experiment that showed penetration of AuNP into agarose when co-injected with ultrasound activated nanocups, the effect of ultrasound-mediated delivery of Cy5-Match-AuNP-Tat was tested in an MDA-MB-435 xenograft model. For these experiments xenografts were generated on each flank of the mice. Mice were cannulated and injected with 0.2 nmol oligonucleotide-bound AuNP constructs, followed by 2 mg nanocups and ultrasound applied to the tumour site (Cy5-Match-AuNP-Tat/NC/ultrasound group (Group 1)) or ultrasound only (Cy5-Match-AuNP-Tat/ultrasound group (Group 2)).

Mice were imaged by IVIS 30 min pre-injection, and 15 min and 4 h post-injection (Fig. 5.6 A). At baseline (30 min pre-injection), no significant differences were observed between Groups 1 and 2 in fluorescence efficiency ($8.4 \times 10^{-6} \pm 1.5 \times 10^{-6}$, $7.6 \times 10^{-6} \pm 6.0 \times 10^{-7}$, respectively) or in tumour/background (T:B) ratio (0.93 ± 0.26, 1.10 ± 0.13, respectively). Similarly, at 15 min p.i., no observable difference was found in efficiency either (Group 1: $6.4 \times 10^{-6} \pm 5.7 \times 10^{-7}$, Group 2: $7.8 \times 10^{-6} \pm 4.0 \times 10^{-7}$), although the T:B ratio showed a non-significant increase for the control group (Group 1: 0.94 ± 0.18, Group 2: 1.36 ± 0.53).

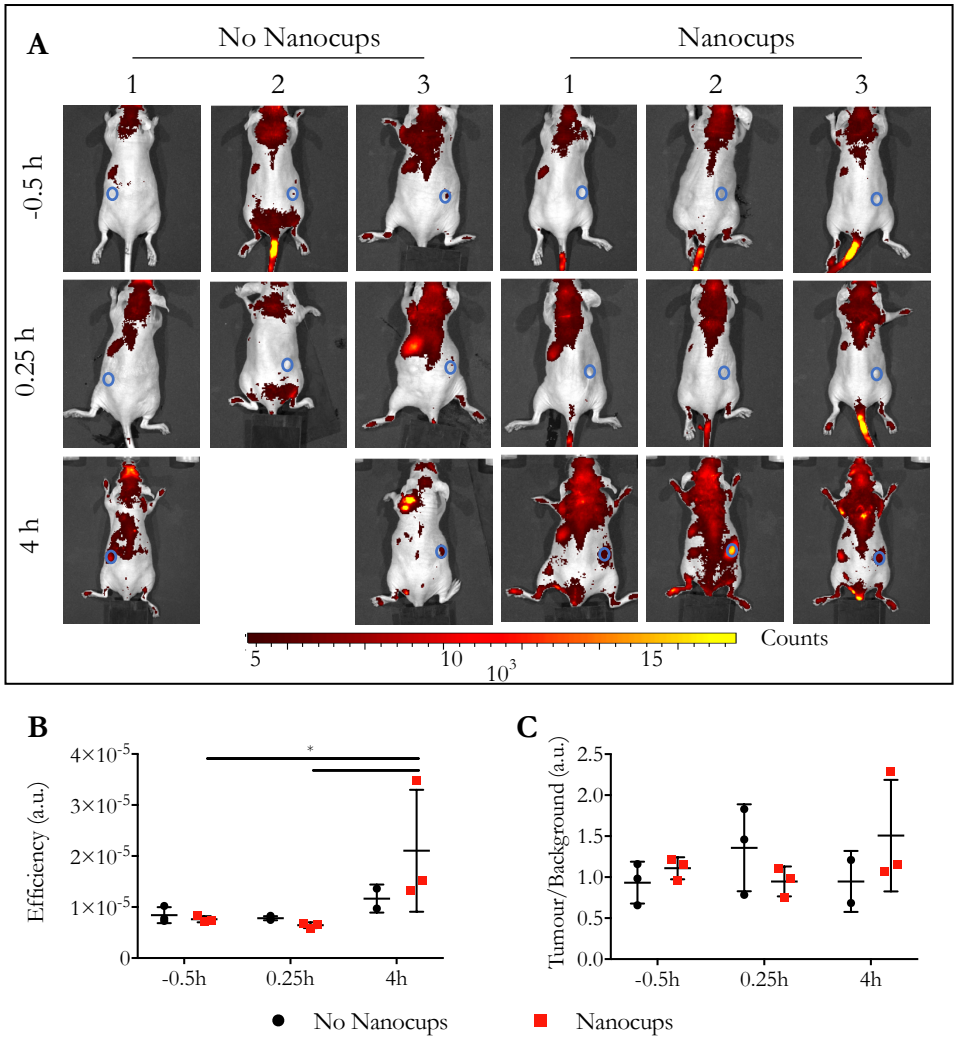


Figure 5.6 *In vivo* imaging of the effect of ultrasound-activatable nanocups on tumour uptake of Cy5-Match-AuNP-Tat in MDA-MB-435 xenografts. A) IVIS images of mice treated with Match-AuNP-Tat, Ultrasound and ± nanocups (Group 1 and 2) 0.5 h pre-injection and 0.25 h and 4 h post-injection. B) ROI efficiency analysis of Group 1 and 2 at indicated timepoints. C) T:B ratio analysis of Group 1 and 2 at indicated timepoints. Symbols represent values for individual mice. Horizontal lines represent the group mean, vertical lines represent the SD. Groups were statistically compared using One-Way ANOVA, Multiple Comparison. *: P < 0.05.

4 h post-injection, the average efficiency had increased (Group 1: 2.1 x 10^{-5} ± 1.2 x 10^{-5}, Group 2: 1.2 x 10^{-5} ± 2.8 x 10^{-6}), resulting in a significant difference within Group 1 between the earlier time points (30 min pre-injection vs 4 h post-injection: P=0.0233, 15 min vs 4 h post-injection: P = 0.145). However, no difference was found between the Groups 1 and 2 (P = 0.209). Furthermore, when the values were plotted as a T:B ratio, the difference between time points were not significant. On closer inspection of the data, the difference seems to be due to an increase in tumour fluorescence in mouse 2 of the NC-treated group. This experiment was repeated, but no significant differences were found.

5.3.6 In vivo ultrasound-mediated delivery of gold nanoparticle constructs in CT26 xenografts

Due to the variability in uptake in the MDA-MB-435 xenograft model, a pilot study was performed using CT26 xenografts (n = 2), a well-studied model for ultrasound-mediated delivery (Kwan et al., 2015). CT26 xenografts were generated by IBME staff in female Balb-c mice, as described previously by Kwan et al., and an i.v. injection of a Cy5-Match-AuNP-Tat/NC mixture then carried out. In one mouse, the xenograft was exposed to ultrasound (Mouse 2), whereas the other mouse received sham ultrasound (Mouse 1). Mice were imaged by IVIS 15 min pre- and post-injection (Fig. 5.7 A), and the ROI was measured (Fig. 5.7 B, C). Pre-injection, little difference in efficiency was found between the two mice (Mouse 1: 2.86 x 10^{-5}, Mouse 2: 2.09 x 10^{-5}). However, post-injection and ultrasound application, fluorescence signal increased to 1.34 x 10^{-4} in the ultrasound group, whereas no change occurred in the sham ultrasound group (1.96 x 10^{-5}), accounting for a fold change of 4.7 and 0.9 compared to baseline, respectively. Due to the low number of mice per group (n = 1), no statistical analysis was performed.

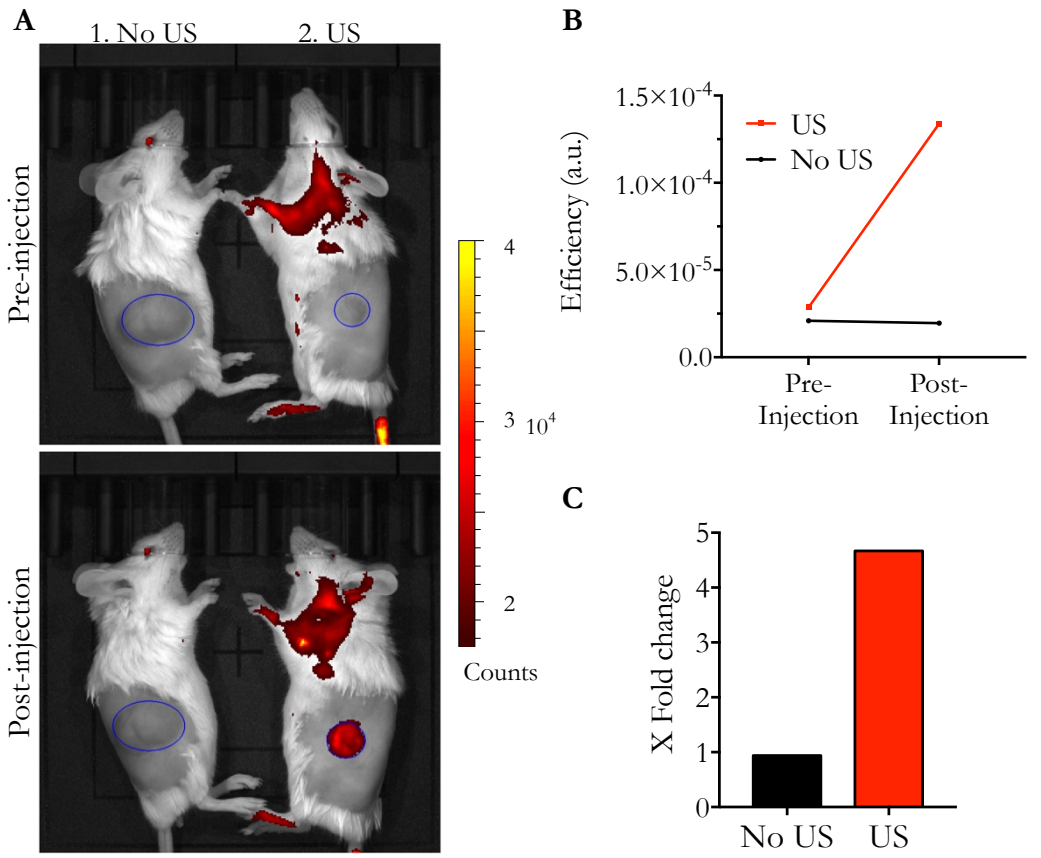


Figure 5.7 *In vivo* imaging of the effect of ultrasound-activatable nanocups on tumour uptake of Cy5-Match-AuNP-Tat in CT26 xenografts. A) IVIS images of mice following intratumoural injection of Match-AuNP-Tat, nanocups ± ultrasound (Mouse 1 and 2) 0.25 h pre-injection and 0.25 h post-injection. B) ROI efficiency analysis of mouse 1 and 2 at indicated timepoints. C) Fold change between efficiency pre- and post-injection.

5.4 Discussion

The potential of functionalised AuNP that selectively target and kill cancer cells has been heralded in the literature as a game-changing drug delivery concept. The unique physicochemical properties enable the intracellular delivery of the payload at high concentrations. Many studies have shown the capabilities of AuNP *in vitro*, but until recently problematic tumour delivery and pharmacokinetic properties have been underreported. In this chapter, the biodistribution and tumour uptake of Match-AuNP-Tat is studied in MDA-MB-435 xenografts with and without ultrasound-activatable cavitation agents.

5.4.1 Match-AuNP-Tat accumulates in liver and spleen

The first biodistribution study with ^{111}In-Match-AuNP-Tat and ^{111}In-Scramble-AuNP-Tat demonstrated that the particles were sequestered in the liver and spleen after 24 hours with low tumour uptake (^{111}In-Match-AuNP-Tat: 0.07 ± 0.01; ^{111}In-Scramble-AuNP-Tat: 0.09 ± 0.02 %I.D./g). It is expected that the clinical effect of the drug will be minimal at this percentage of uptake.

The poor biodistribution profile of these AuNP constructs is not unexpected. Although it is now 15 years since their use for biological purposes, the pharmacokinetic profile of AuNPs has been fairly understudied and underreported, despite the indication of the frequently observed unfavourable uptake in the liver. In the past few years, several critical studies showing that the major hurdle to clinical translation of nanoparticles is low tumour uptake and poor pharmacokinetic profile (Blanco et al., 2015; Wilhelm et al., 2016; Nakamura et al., 2016) have received attention. Wilhelm et al. conducted a systematic review of the literature published between 2005 and 2015, and found that the median tumour uptake for AuNP was 0.7% I.D./g. This low median uptake means that a large injected dose would be required to achieve a beneficial clinical outcome. Such a high dose is likely to cause off-target effects and high costs per treatment. In this study, less than 0.1% I.D./g reached the tumour, which is 7-fold lower than the median number quoted by Wilhelm et al. This phenomenon can be explained by several factors, including high liver sequestration and poor blood vessel fluid dynamics of the AuNP constructs, as well as xenograft model limitations such as poor vascularisation and a low EPR effect. In this thesis, the problem of reducing the uptake of the AuNPs in the liver has not been explored. Several previous studies have demonstrated that NP are primarily taken up by the Kupffer cells, specialised macrophages in the liver, which are part of the RES (Tsoi et al., 2016). Counterintuitive to the high liver accumulation, radiotoxicity may therefore be limited with these NP, since Kupffer cells are generally radioresistant (Tsutsui and Nishiguchi, 2014).

However, to mitigate the effect of potential poor fluid dynamics and a low EPR, a strategy was developed utilising ultrasound-activatable cavitation agents to cause AuNP extravasation.

5.4.2 Ultrasound-activated nanocups resulted in extravasation of Match-AuNP-Tat in vitro

Various reports have demonstrated the potential use of ultrasound-activatable cavitation agents for tumour delivery of nanoparticles, such as lipid coated quantum dots (Lin et al., 2010), liposomal doxorubicin (Lin et al., 2012), and AuNP (Lea-Banks et al., 2016). To test the potential of this approach to enhance delivery of Match-AuNP-Tat, AuNP constructs were labelled with Cy5 and tested in a purpose-built *in vitro* experimental setup. Previously, a study by Lea-Banks et al. (2016) showed that AuNP 200 nm in diameter were propelled in agarose gel by SonoVue, an ultrasound-activatable cavitation and contrast agent, a result that corresponds well with the findings in the current study.

In this study, it was shown that the combination of ultrasound and nanocups led to extensive *in vitro* extravasation in terms of peak penetration depth and total area, which correlated with an increase in mean cavitation emission power. The observed pattern of extravasation had a typical deep and narrow penetration, which may indicate microjet formation (Tezel and Mitragotri, 2003). Nanocups are relatively recently developed cavitation agents that are designed to overcome some of the pharmacokinetic disadvantages of other agents in this class. Earlier studies showed that ultrasound-activated nanocups caused extravasation of molecules such as antibodies (Kwan et al., 2015) and virus particles (Myers et al., 2016). The results here are the first indication that nanocups can cause extravasation of nanoparticles as well.

The agarose tissue model provided an indication of the potential to activate nanocups to cause AuNP extravasation. However, the question remains whether this effect is biologically relevant. Agarose gel may not be fully representative of tumour tissue, and the blood flow and blood concentration may differ *in vivo* from the closely controlled parameters in the *in vitro* set up.

5.4.3 Ultrasound-activated nanocups have a mixed effect in vivo

After the successful *in vitro* experiments, ultrasound-mediated delivery of Match-AuNP-Tat was tested in an MDA-MB-435 xenograft model. Due to Home Office license restrictions at the time of the experiments, it was not possible to combine SPECT with ultrasound-mediated delivery. For this reason, Cy5-Match-AuNP-Tat was tested and detected using IVIS. Initial studies focussed on the optimisation of the IVIS settings and the determination of the detection limits. These experiments clearly demonstrated that the probe is detectable at biologically relevant concentrations in tissue.

After this validation step, a pilot experiment was carried out in MDA-MB-435 xenografts. It was found that there was statistically significant greater tumour uptake in mice 4 h after administration of Cy5-Match-AuNP-Tat plus nanocups and ultrasound, in comparison to the same group pre-ultrasound and 15 min post-ultrasound exposure. This effect, however, was attributable to the result for one mouse, that showed a high increase of fluorescent signal in the tumour region. Despite this, the difference between the control group (no nanocups) was not significant, which is likely to be caused by the high variation. This variation can be caused by biological factors, such as the tumour model, or physical factors, such as the ultrasound setup.

To test whether the xenograft model was the cause of the observed variation and poor tumour uptake results, a further pilot study with two CT26 xenograft Balb-c mice was conducted. The CT26 xenograft model is known to be densely vascularised and characterised by a marked EPR effect, potentially providing a better profile for ultrasound-mediated drug delivery (Kwan et al., 2015). In this pilot study, the combination of ultrasound and nanocups led to a 4.7-fold higher uptake after exposure. In contrast, there was no change in tumour fluorescence in the group that received sham US. Since this was a pilot study, a small number of animals was used, and so no conclusions can be made based on this result. However, it supports the use of a well-

vascularised tumour model to test the combination of AuNP constructs and ultrasound-activatable cavitation agents.

Although the focus of this thesis has been to optimise the particle and tumour delivery conditions, it is acknowledged that the tumour model is relatively underexplored. The decision to use he MDA-MB-435 cell line as xenograft model was based on the extensive *in vitro* data with this cell line. However, this does not do justice to the variations in tumour biology between different xenograft models (Sulheim et al., 2018; Ehling et al., 2014). After several experiments with this xenograft model, there are indications that MDA-MB-435 tumours are often not well-vascularised, which may be a reason behind the low and variable tumour uptake. In an important study by Sulheim et al. (2018), it was demonstrated that vascularisation is of crucial importance to the successful uptake of nanoparticles. For this reason, it is recommended to further characterise the vascularisation of the MDA-MB-435 xenograft model with high frequency ultrasound imaging, contrast agent MRI, or immunohistochemistry. Furthermore, it is intended to repeat the current study with a known well-vascularised xenograft tumour. CT26 is a mouse colorectal cancer cell line, and is therefore not suited for further study of anti-hTR targeting drugs, since mice have a different sequence TR. A suitable alternative may be the frequently used hTR-expressing epidermoid carcinoma cell line A431 (Asai et al., 2003). This cell line can be used to generate fast-growing and well-vascularised xenografts, which may be more suitable for testing the effects of AuNP (Ehling et al., 2014).

Besides the biological factors that can play a role, the *in vivo* ultrasound may require optimisation to reduce the variation. Improvements may include better tumour alignment with laser-guidance, degassing of coupling gel to avoid ultrasound reflection in the gel, and better maintenance of temperature to reduce vasoconstriction in the tumour.

5.4.4 Concluding remarks

This study provides the first indication that nanocups plus US can be used for the tumour delivery of Match-AuNP-Tat. The *in vitro* data in a phantom model have shown the clear potential of extravasation under the influence of cavitation agents. Although the *in vivo* results have been variable, and will therefore require further experimentation, the data for individual mice and conditions have been remarkable. For future studies, it is recommended to reduce the variation by altering the xenograft model and optimising the ultrasound setup. When the tumour uptake of the construct is improved, tumour growth studies are recommended to investigate the therapeutic potential of ^{111}Match-AuNP-Tat.

CHAPTER 6. DISCUSSION

The primary aim of this DPhil thesis was the *in vitro* and *in vivo* delivery of ^{111}In-labelled hTR-targeting oligonucleotides for the treatment of telomerase-positive cancer. This was addressed by utilising AuNP-based oligonucleotide carriers with and without the CPP Tat and tested in cell- and xenograft-based systems. This work involved a multidisciplinary approach to answer research questions in the fields of radio- and nanoparticle chemistry, telomerase biology, and pharmacology. The emphasis of this chapter lies on the broader position of this work in literature, its limitations and potential avenues for future research.

6.1 hTR-targeting gold nanoparticle radiopharmaceuticals

Our aim to therapeutically target hTR with AuNP-based radiopharmaceuticals is, according to our best understanding, unique. Examples that include parts of our strategy are, however, present in the literature. An excellent study by Ma et al. (2016) showed the development of a molecular beacon-based drug delivery system for detection of telomerase activity in cancer cells and telomerase-triggered doxorubicin release for specific cancer targeting. Their construct was composed of an AuNP core that was densely packed with fluorescent FITC-labelled hairpin DNA sequences hybridized with telomerase primers, with doxorubicin intercalated into the stem region of the DNA sequence. Telomerase presence elongated the primers, resulting in inner chain substitution followed by FITC fluorescence and doxorubicin release. This study was later followed up with the design of a telomerase-responsive DNA icosahedron that precisely released caged platinum nanodrugs into cisplatin-resistant tumours (Ma et al., 2018). Liu et al. (2007) found that targeting mRNA of hTERT subunit with radiolabelled (Technicium-99m) oligonucleotides was effective as an in vivo marker of telomerase expression. Several groups have employed anti-hTR ASO-coated AuNP to develop sensitive detection methods for activity (Zong et al., 2013; Wang et al., 2012; Xiao et al., 2010). Doss et al. (2012) described the theoretical possibility of targeting the promoter region of the hTERT gene with ON-AuNP

constructs, but no research activity in this area has been pursued. ^{111}In has been conjugated to AuNPs by several researchers. Ng et al. (2014) directly attached ^{111}In to AuNPs for the in vivo detection of pharmacokinetic parameters. Melancon et al. (2008) labelled hollow anti-EGFR antibody-coated AuNPs with ^{111}In for similar reasons. From a therapeutic perspective, Song et al. (2016, 2017) demonstrated effective cell kill with anti-EGFR ^{111}In-labelled AuNPs.

6.2 In vitro perspectives and future work

6.2.1 Internalisation and uptake

Here, we describe the successful internalisation of three different AuNP constructs. The first two involve AuNP with a core diameter of 15 nm (ON-AuNP and ON-AuNP-Tat) whereas the third has a 2.4 nm diameter core (ON-uAuNP). It was found that both the size and functionalisation can have profound effects on the uptake kinetics in MDA-MB-435 cells.

The functionalisation with Tat caused a significantly higher uptake of AuNP, which resulted in telomerase-dependent cell kill. This work adds to the large body of data that shows that Tat can facilitate higher uptake level of the payload delivered via carrier systems (Berry et al., 2007; Morshed et al., 2016; Cesbron et al., 2015; Todorova et al., 2014; Krpetić et al., 2011; Torchilin, 2008). The mechanism by which this happens, remains, however, unclear, and further research may be required to find out which mechanism of uptake is involved. Various endocytic mechanisms are operative in mammalian cells, including clathrin-mediated endocytosis, caveolin-mediated endocytosis, clathrin- or caveolin-independent endocytosis, and macropinocytosis (Doherty and McMahon, 2009). To determine the mechanism of uptake, it is suggested to initiate an uptake experiment at 4 °C to confirm the internalisation is mediated via endocytosis (Fernando et al., 2010). Subsequently, immunofluorescent co-localisation studies with Texas red and lysosomal associated membrane protein-1 (LAMP-1 or CD107a) may be done to confirm the observation by TEM that AuNPs mainly reside in endosomes. Lastly, endocytic pathway-specific antagonists may identify the exact uptake mechanism, such as

chlorpromazine (clathrin-mediated endocytosis inhibitor), genistein (clathrin/caveolae-mediated endocytosis inhibitor) and wortmannin (macropinocytosis).

An interesting observation in this work was the confocal microscopy of ON-uAuNP, which demonstrated a profound nuclear and extra-endosomal presence of the construct. Unfortunately, due to difficulties to synthesise pure products, these AuNP constructs were not further developed. However, the initial data look promising, and it is therefore recommended to test different AuNP synthetic methods to obtain more pure products. An example mentioned in Chapter 3 may be the use of short PEG-linkers between the oligonucleotides and the uAuNP surface, as described by Kumar et al. (2013). Another approach may be the use of a method originally developed by Templeton et al. (1999), who utilised tiopronin as a capping agent. The carboxylic group of tiopronin can serve as a binding site for amino-modified oligonucleotides when reacted with an EDC/NHS reaction. uAuNP synthesised this way have shown profound nuclear uptake and a sequence dependent reduction in cell viability and gene expression (Huang et al., 2012a; Huo et al., 2014). This synthesis route may provide more pure constructs and may therefore be more suited to the conjugation of hTR-targeting ^{111}In-labelled oligonucleotides.

The options explored here are far from exhaustive, and other sizes, such as 5 nm AuNP may be investigated to determine a different in vitro profile. Additionally, different shapes of AuNP may contribute to different uptake mechanisms and endosomal escape. Examples are nanorods and nanostars, which have been recorded to internalise at different rates compared to spherical AuNP (Chithrani et al., 2006; Dykman and Khlebtsov, 2014). Furthermore, different types of functional groups may provide different options for (sub-)cellular targeting. The current approach involves non-specific uptake, but targeting ligands against overexpressed transmembrane receptors may provide a more specific method of delivery (Dreaden et al., 2012). An example would be functionalisation with a ligand targeting EGFR, a membrane-bound receptor that is overexpressed in various cancers, including malignancies of the breast,

bladder, and oesophagus. Song et al. (2016, 2017) demonstrated that EGF-functionalised AuNP are preferentially taken up by EGFR-expressing cells and localise in the perinuclear area. Addition of this compound to the ligand shell of Match-AuNP-Tat may provide an additional targeting and uptake mechanism.

6.2.2 Molecular biology and radiosensitisation

Here, it is described that telomerase activity can be inhibited by AuNP functionalised with ^{111}In-labelled anti-hTR oligonucleotides. This study provides further evidence of non-canonical roles of hTR and the telomerase holoenzyme. It is shown that concomitant inhibition of telomerase and intracellular radiation in the form of Auger electrons or external radiation in the form of 661 keV photons can result in the acute upregulation of DNA DSBs, suggesting a role in genome stability beyond telomere length maintenance. It is previously shown that hTR interacts with Ku70/80 resulting in the phosphorylation of hnRNP A1, which leads to RPA-to-POT1 switching and ATR abrogation in G2 and M phase (Ting et al., 2005, 2009; Sui et al., 2015). This function can be abrogated by the inhibition of hTR, inducing an upregulation of ATR at telomeric DNA and the induction of G2/M arrest. Combined with irradiation, this arrest can lead to cancer cell apoptosis (DiPaola, 2002). Although it is shown that the construct has a downstream effect of such inhibition on DNA DSBs and clonogenic cell survival, future work may focus on the determining on the proposed mechanism of action. It is therefore suggested to conduct immunoprecipitation and western analysis to determine the effect of ^{111}In-Match-AuNP-Tat on the phosphorylation of hnRNP A1, as well as the effects on the activation of Chk1 and p53 (Kedde et al., 2006).

6.2.3 Binding properties

In this work it is demonstrated that DTPA-labelled anti-hTR oligonucleotides retain the ability to inhibit telomerase activity in a sequence-specific manner when attached to the surface of an AuNP. Unfortunately, this effect was difficult to observe for the Match-AuNP-Tat construct

due to non-specific inhibition of the TRAPeze XL detection assay by Tat. In this study, it is nonetheless apparent that the effects of Match-AuNP-Tat are telomerase specific, but it is possible that inhibition of telomerase could be increased further. An option may be to add a PEG or base linker between the thiol group and the inhibiting sequence to avoid the steric hindrance that may be caused by PEG and Tat. Oishi et al. (2006) showed that this approach was successful and resulted in stable particles that were readily taken up by cancer cells. It is therefore proposed to investigate the effect of PEG-linkers on the inhibitory and cell-killing effect of ^{111}In-Match-AuNP-Tat.

6.3 In vivo perspectives and future work

Nanoparticles have long suffered from poor pharmacokinetics and tumour uptake, although this issue has been relatively neglected until recently. A critical review by Wilhelm et al. (2016) investigated the available literature, and found that the median tumour uptake was 0.7%, indicating that most studies fail to achieve clinically relevant tumour accumulation. Blanco et al. (2015) described that upon i.v. injection of AuNP, the constructs encounter seven sequential obstacles that hinder the site-specific and efficacious delivery to tumours: opsonisation and uptake by the mononuclear phagocyte system (MPS), nonspecific tissue distribution, blood vessel flow limitations, unfavourable tumour pressure gradients, poor cellular internalisation, endosomal and lysosomal entrapment, and drug efflux pumps. Different strategies may improve these characteristics to provide a better pharmacokinetic profile.

The primary limitation is identified as opsonisation by the MPS, which encompasses a network of phagocytic cells, including resident macrophages, in the lymph nodes, spleen, and predominantly the liver (Patel and Moghimi, 1998). AuNP are opsonised after surface adsorption of plasma proteins, such as albumin, complement components, immunoglobulins and apoliproteins (Tenzer et al., 2013). This protein corona, which forms dependent on size, charge, surface chemistry and hydrophobicity, interacts with phagocyte surface receptors,

resulting in spleen, liver and lymphatic internalisation (Nel et al., 2009). The liver uptake is further enhanced due to the non-continuous endothelium with vascular fenestrations (50–100 nm) in the liver, which results in non-specific accumulation of AuNP (Braet et al., 2007). In this work, there is a profound uptake of the AuNP construct by the MPS system, which hampers the tumour availability. The most common strategy for reducing rapid MPS uptake is the utilisation of PEG chains, as was done for this study (Harris and Chess, 2003). However, longer PEG-chains (±6000 MW) may increase circulation time and potential tumour uptake, although this may come at the price of reduced targeted binding due to steric hindrance (Song et al., 2016). This strategy is nonetheless recommended to determine whether the circulation time may be improved. Another interesting approach is to actively 'stealth' the particle. Rodriguez et al. (2013) explored this option by attaching the 'don't eat-me' marker CD47 'self' peptides to the nanoparticle surface and found that this improved circulation time and tumour uptake dramatically. Parodi et al. (2013) utilised biomimetic leukocyte membranes, which conferred cell-like properties to the nanoparticle and result in 75% less uptake by murine J774 liver macrophages. Strategies like this may reduce the ^{111}In-Match-AuNP-Tat liver sequestration and may be explored in future research.

Two other barriers, blood vessel flow limitations and unfavourable tumour pressure gradients, have been addressed in this work. Several factors, including size and geometry, have been shown to significantly increase vascular wall margination dynamics (Blanco et al., 2015). Spherical AuNP mitigate flow in a cell-free layer, which results in a considerable distance from endothelial surfaces, thereby reducing targeting strategies and passive accumulation via the EPR effect (Decuzzi et al., 2005). Furthermore, the high intratumoural pressure, which is the result of aggressive cellular growth, fibrosis, interrupted vasculature and lymphatics, and a dense extracellular matrix can form a formidable barrier for AuNP entry (Blanco et al., 2015). Ultrasound-activatable cavitation agents were used to locally direct AuNP constructs towards the endothelial layer and to overcome the outward intratumoural pressure which prevent a

higher tumour uptake. The partial success in this work paves the way for further research with ultrasound-mediated cavitation agents, and several future work options have been discussed in Chapter 5. Other options may also be explored, including the utilisation of different shaped AuNP. Discoidal AuNP may marginate to blood vessel walls more frequently than spherical and quasi-spherical AuNP (Gentile et al., 2008). Whereas the latter two constructs tend to stream parallel and away from the vessel wall, ellipsoidal AuNP tend to tumble and oscillate from one wall to the other. For this reason, it may be interesting to explore discoidal AuNP for delivery purposes.

6.4 Clinical perspectives

TRT has been utilised in the clinic for more than seventy years for indications such as thyroid cancer, liver metastases, neuroendocrine tumours, and neuroblastoma (Pouget et al., 2011). Despite their clinical success, widespread use has long been hampered by the logistical problem of working with open source radiation. With the rising availability of in-house radionuclide generators however, the application of TRT is rising rapidly (Gill et al., 2017). In the United Kingdom, the number of TRT-based treatments increased by 38% over the period 2007-2012 and is expected grow beyond this with the recent successful clinical trials with $^{223}RaCl_2$, ^{177}Lu-Dotatate, ^{177}Lu-PSMA (Rojas et al., 2015; Rahbar et al., 2017; Parker et al., 2013; Strosberg et al., 2017). Obstacles to the further proliferation of TRT remain, however, and include poor tumour vasculature and heterogenous expression of the targeted molecular marker. Furthermore, the relative radiosensitivity of the targeted cell plays a large role in cell-fate after irradiation, as well as the distribution of the radiopharmaceutical on a system, organ, tissue, cellular and subcellular level. Other important factions include the biological effectiveness of the particulate irradiation, as well as the induction of bystander response (Gill et al., 2017). This work was aimed to address these obstacles. The ubiquitously expressed malignant biomarker telomerase was chosen in an effort to reduce biomarker heterogeneity. This target is under

clinical development in separate studies, as discussed in Chapter 1 (Baerlocher et al., 2015; Tefferi et al., 2015). Furthermore, a delivery system was chosen that enabled rapid and substantial cellular uptake. Third, the Auger electron emitter ^{111}In was chosen to minimise the dose to non-targeted tissue. However, the poor pharmacokinetics, as described in the in vivo section, requires further development before this drug will reach clinical potential. Over the past decades, a vast amount of in vitro and in vivo data has come available on AuNPs (Dykman and Khlebtsov, 2012, 2014). Yet, an underwhelming number of clinical trials have been conducted so far, and include studies into a MRI contrast agent and a drug for atherosclerosis (Weissig and Guzman-Villanueva, 2015). By addressing the barriers that were mentioned in the in vitro and in vivo paragraphs this may improve. Further research in this field needs to focus on improving pharmacokinetic parameters in order to drive this concept from bench to bedside.

6.5 Summary and conclusion

This work has sought to develop and characterise a novel AuNP-based delivery system for hTR-targeting ^{111}In-labelled oligonucleotides for the selective treatment of telomerase-positive cancers. The synthesised AuNP constructs were found to greatly enhance the cellular uptake of radiolabelled oligonucleotides, whilst retaining the ability to inhibit telomerase activity. The addition of Tat on the AuNP surface resulted in increased nuclear localisation. This uptake caused a significant dose-dependent impact of ^{111}In-Match-AuNP-Tat on the clonogenic survival of a telomerase-positive cell line, but not telomerase-negative cells, and corresponded with an increase in DNA DSBs. Biodistribution studies found that the AuNP constructs accumulated in the liver with low tumour uptake. To mitigate this effect, nanocups, ultrasound-activatable cavitation agents, were used to direct the AuNP constructs to the tumour. Nanocups significantly increased extravasation of Cy5-Match-AuNP-Tat in an in vitro model and was therefore trialled in an in vivo setting. Despite a promising pilot study with high tumour uptake, subsequent larger studies failed to increase tumour uptake of the compound.

In conclusion, this study delivered a solution for the subcellular delivery of radiolabelled anti-hTR oligonucleotides by using an AuNP-based system. This novel approach of combined modality telomerase-targeting may be a start for future in vivo research with ultrasound-mediated delivery and the techniques described in this thesis may provide a building block for nucleic acid-based radiopharmaceutical research.

REFERENCES

Ackerson, C.J., P.D. Jadzinsky, J.Z. Sexton, D.A. Bushnell, and R.D. Kornberg. 2010. Synthesis and bioconjugation of 2 and 3 nm-diameter gold nanoparticles. *Bioconjug. Chem.* 21:214–218. doi:10.1021/bc900135d.

Agarwal, M., S. Pandita, C.R. Hunt, A. Gupta, X. Yue, S. Khan, R.K. Pandita, D. Pratt, J.W. Shay, J.-S.A. Taylor, and T.K. Pandita. 2008. Inhibition of telomerase activity enhances hyperthermia-mediated radiosensitization. *Cancer Res.* 68:3370–3378. doi:10.1158/0008-5472.CAN-07-5831.

Aghevlian, S., A.J. Boyle, and R.M. Reilly. 2017. Radioimmunotherapy of cancer with high linear energy transfer (LET) radiation delivered by radionuclides emitting α-particles or Auger electrons. *Adv. Drug Deliv. Rev.* 109:102–118. doi:10.1016/j.addr.2015.12.003.

Akiyama, M., O. Yamada, N. Kanda, S. Akita, T. Kawano, T. Ohno, H. Mizoguchi, Y. Eto, K.C. Anderson, and H. Yamada. 2002. Telomerase overexpression in K562 leukemia cells protects against apoptosis by serum deprivation and double-stranded DNA break inducing agents, but not against DNA synthesis inhibitors. *Cancer Lett.* 178:187–197.

Alcaraz-Pérez, F., J. García-Castillo, D. García-Moreno, A. López-Muñoz, M. Anchelin, D. Angosto, L.I. Zon, V. Mulero, and M.L. Cayuela. 2014. A non-canonical function of telomerase RNA in the regulation of developmental myelopoiesis in zebrafish. *Nat. Commun.* 5:3228. doi:10.1038/ncomms4228.

Ardestani, M.S., A.J. Arabzadeh, Z. Heidari, A. Hosseinzadeh, H. Ebrahimi, E. Hashemi, M. Mosayebnia, M. Shafiee-Alavidjeh, A. Alavi, M.H. Babaei, A. Rahmim, S.E.S. Ebrahimi, and M. Amanlou. 2010. Novel and facile methods for the synthesis of DTPA-mono-amide: a new completely revised strategy in radiopharmaceutical chemistry. *J. Radioanal. Nucl. Chem.* 283:447–455. doi:10.1007/s10967-009-0414-y.

Asai, A., Y. Oshima, Y. Yamamoto, T. Uochi, H. Kusaka, S. Akinaga, Y. Yamashita, K. Pongracz, R. Pruzan, E. Wunder, M. Piatyszek, S. Li, A.C. Chin, C.B. Harley, and S. Gryaznov. 2003. A novel telomerase template antagonist (GRN163) as a potential anticancer agent. *Cancer Res.* 63:3931–3939.

Baerlocher, G.M., E. Oppliger Leibundgut, O.G. Ottmann, G. Spitzer, O. Odenike, M.A. McDevitt, A. Röth, M. Daskalakis, B. Burington, M. Stuart, and D.S. Snyder. 2015. Telomerase inhibitor imetelstat in patients with essential thrombocythemia. *N. Engl. J. Med.* 373:920–928. doi:10.1056/NEJMoa1503479.

Bailey, D.L., and K.P. Willowson. 2013. An evidence-based review of quantitative SPECT imaging and potential clinical applications. *J. Nucl. Med.* 54:83–89. doi:10.2967/jnumed.112.111476.

Bavelaar, B.M., B.Q. Lee, M.R. Gill, N. Falzone, and K.A. Vallis. 2018. Subcellular targeting of theranostic radionuclides. *Front. Pharmacol.*

Beisner, J., M. Dong, S. Taetz, N. Nafee, E.-U. Griese, U. Schaefer, C.-M. Lehr, U. Klotz, and T.E. Mürdter. 2010. Nanoparticle mediated delivery of 2'-O-methyl-RNA leads to efficient

telomerase inhibition and telomere shortening in human lung cancer cells. *Lung Cancer* 68:346–354. doi:10.1016/j.lungcan.2009.07.010.

Berry, C.C., J.M. de la Fuente, M. Mullin, S.W.L. Chu, and A.S.G. Curtis. 2007. Nuclear localization of HIV-1 tat functionalized gold nanoparticles. *IEEE Trans. Nanobioscience.* 6:262–269.

Bhatnagar, S., J.J. Kwan, A.R. Shah, C.-C. Coussios, and R.C. Carlisle. 2016. Exploitation of sub-micron cavitation nuclei to enhance ultrasound-mediated transdermal transport and penetration of vaccines. *J. Controlled Release.* 238:22–30. doi:10.1016/j.jconrel.2016.07.016.

Blackburn, E.H., and K. Collins. 2011. Telomerase: an RNP enzyme synthesizes DNA. *Cold Spring Harb. Perspect. Biol.* 3:a003558. doi:10.1101/cshperspect.a003558.

Blanco, E., H. Shen, and M. Ferrari. 2015. Principles of nanoparticle design for overcoming biological barriers to drug delivery. *Nat. Biotechnol.* 33:941–951. doi:10.1038/nbt.3330.

Bootz, A., V. Vogel, D. Schubert, and J. Kreuter. 2004. Comparison of scanning electron microscopy, dynamic light scattering and analytical ultracentrifugation for the sizing of poly(butyl cyanoacrylate) nanoparticles. *Eur. J. Pharm. Biopharm. EV.* 57:369–375. doi:10.1016/S0939-6411(03)00193-0.

Braet, F., E. Wisse, P. Bomans, P. Frederik, W. Geerts, A. Koster, L. Soon, and S. Ringer. 2007. Contribution of high-resolution correlative imaging techniques in the study of the liver sieve in three-dimensions. *Microsc. Res. Tech.* 70:230–242. doi:10.1002/jemt.20408.

Brandenberger, C., C. Mühlfeld, Z. Ali, A.-G. Lenz, O. Schmid, W.J. Parak, P. Gehr, and B. Rothen-Rutishauser. 2010. Quantitative evaluation of cellular uptake and trafficking of plain and polyethylene glycol-coated gold nanoparticles. *Small.* 6:1669–1678. doi:10.1002/smll.201000528.

Burnett, J.C., and J.J. Rossi. 2012. RNA-based therapeutics: current progress and future prospects. *Chem. Biol.* 19:60–71. doi:10.1016/j.chembiol.2011.12.008.

Cai, Z., N. Chattopadhyay, K. Yang, Y.L. Kwon, S. Yook, J.-P. Pignol, and R.M. Reilly. 2016. ^{111}In-labeled trastuzumab-modified gold nanoparticles are cytotoxic in vitro to HER2-positive breast cancer cells and arrest tumor growth in vivo in athymic mice after intratumoral injection. *Nucl. Med. Biol.* 43:818–826. doi:10.1016/j.nucmedbio.2016.08.009.

Cai, Z., J.-P. Pignol, C. Chan, and R.M. Reilly. 2010. Cellular dosimetry of ^{111}In using Monte Carlo N-particle computer code: comparison with analytic methods and correlation with In vitro cytotoxicity. *J. Nucl. Med.* 51:462–470. doi:10.2967/jnumed.109.063156.

Canton, I., and G. Battaglia. 2012. Endocytosis at the nanoscale. *Chem. Soc. Rev.* 41:2718–2739. doi:10.1039/c2cs15309b.

Cao, Y.C., R. Jin, and C.A. Mirkin. 2002. Nanoparticles with Raman spectroscopic fingerprints for DNA and RNA detection. *Science.* 297:1536–1540. doi:10.1126/science.297.5586.1536.

Carlisle, R., J. Choi, M. Bazan-Peregrino, R. Laga, V. Subr, L. Kostka, K. Ulbrich, C.-C. Coussios, and L.W. Seymour. 2013. Enhanced tumor uptake and penetration of virotherapy using polymer stealthing and focused ultrasound. *J. Natl. Cancer Inst.* 105:1701–1710. doi:10.1093/jnci/djt305.

Castella, M., S. Puerto, A. Creus, R. Marcos, and J. Surralles. 2007. Telomere length modulates human radiation sensitivity in vitro. *Toxicol. Lett.* 172:29–36. doi:10.1016/j.toxlet.2007.05.012.

Cazenave, C., M. Chevrier, T.T. Nguyen, and C. Hélène. 1987. Rate of degradation of [alpha]- and [beta]-oligodeoxynucleotides in Xenopus oocytes. Implications for anti-messenger strategies. *Nucleic Acids Res.* 15:10507–10521.

Cesbron, Y., U. Shaheen, P. Free, and R. Lévy. 2015. TAT and HA2 facilitate cellular uptake of gold nanoparticles but do not lead to cytosolic localisation. *PLoS ONE*. 10. doi:10.1371/journal.pone.0121683.

Chen, Y., and Y. Zhang. 2016. Functional and mechanistic analysis of telomerase: An antitumor drug target. *Pharmacol. Ther.* 163:24–47. doi:10.1016/j.pharmthera.2016.03.017.

Chen, Z., K.S. Koeneman, and D.R. Corey. 2003. Consequences of telomerase inhibition and combination treatments for the proliferation of cancer cells. *Cancer Res.* 63:5917–5925.

Chithrani, B.D., A.A. Ghazani, and W.C.W. Chan. 2006. Determining the size and shape dependence of gold nanoparticle uptake into mammalian cells. *Nano Lett.* 6:662–668. doi:10.1021/nl052396o.

Choi, C.H.J., L. Hao, S.P. Narayan, E. Auyeung, and C.A. Mirkin. 2013. Mechanism for the endocytosis of spherical nucleic acid nanoparticle conjugates. *Proc. Natl. Acad. Sci. U. S. A.* 110:7625–7630. doi:10.1073/pnas.1305804110.

Console, S., C. Marty, C. García-Echeverría, R. Schwendener, and K. Ballmer-Hofer. 2003. Antennapedia and HIV transactivator of transcription (TAT) "protein transduction domains" promote endocytosis of high molecular weight cargo upon binding to cell surface glycosaminoglycans. *J. Biol. Chem.* 278:35109–35114. doi:10.1074/jbc.M301726200.

Cornelissen, B. 2014. Imaging the inside of a tumour: a review of radionuclide imaging and theranostics targeting intracellular epitopes. *J. Label. Compd. Radiopharm.* 57:310–316. doi:10.1002/jlcr.3152.

Cornelissen, B., S. Darbar, V. Kersemans, D. Allen, N. Falzone, J. Barbeau, S. Smart, and K.A. Vallis. 2012. Amplification of DNA damage by a γH2AX-targeted radiopharmaceutical. *Nucl. Med. Biol.* 39:1142–1151. doi:10.1016/j.nucmedbio.2012.06.001.

Cornelissen, B., V. Kersemans, S. Darbar, J. Thompson, K. Shah, K. Sleeth, M.A. Hill, and K.A. Vallis. 2011. Imaging DNA damage in vivo using gammaH2AX-targeted immunoconjugates. *Cancer Res.* 71:4539–4549. doi:10.1158/0008-5472.CAN-10-4587.

Cornelissen, B., V. Kersemans, K. McLarty, L. Tran, and R.M. Reilly. 2009a. ^{111}In-labeled immunoconjugates (ICs) bispecific for the epidermal growth factor receptor (EGFR) and cyclin-dependent kinase inhibitor, p27Kip1. *Cancer Biother. Radiopharm.* 24:163–173. doi:10.1089/cbr.2008.0553.

Cornelissen, B., V. Kersemans, K. McLarty, L. Tran, K.A. Vallis, and R.M. Reilly. 2009b. In vivo monitoring of intranuclear p27(kip1) protein expression in breast cancer cells during trastuzumab (Herceptin) therapy. *Nucl. Med. Biol.* 36:811–819. doi:10.1016/j.nucmedbio.2009.05.003.

Cornelissen, B., and K.A. Vallis. 2010. Targeting the nucleus: an overview of Auger-electron radionuclide therapy. *Curr. Drug Discov. Technol.* 7:263–279.

Cornelissen, B., A. Waller, S. Able, and K.A. Vallis. 2013. Molecular radiotherapy using cleavable radioimmunoconjugates that target EGFR and γH2AX. *Mol. Cancer Ther.* 12:2472–2482. doi:10.1158/1535-7163.MCT-13-0369.

Cui, L., S. Her, G.R. Borst, R.G. Bristow, D.A. Jaffray, and C. Allen. 2017. Radiosensitization by gold nanoparticles: Will they ever make it to the clinic? *Radiother. Oncol.* doi:10.1016/j.radonc.2017.07.007.

Darzacq, X., N. Kittur, S. Roy, Y. Shav-Tal, R.H. Singer, and U.T. Meier. 2006. Stepwise RNP assembly at the site of H/ACA RNA transcription in human cells. *J Cell Biol.* 173:207–218. doi:10.1083/jcb.200601105.

Dasgupta, A., M. Liu, T. Ojha, G. Storm, F. Kiessling, and T. Lammers. 2016. Ultrasound-mediated drug delivery to the brain: principles, progress and prospects. *Drug Discov. Today Technol.* 20:41–48. doi:10.1016/j.ddtec.2016.07.007.

Decuzzi, P., S. Lee, B. Bhushan, and M. Ferrari. 2005. A theoretical model for the margination of particles within blood vessels. *Ann. Biomed. Eng.* 33:179–190.

Deng, Y., S.S. Chan, and S. Chang. 2008. Telomere dysfunction and tumour suppression: the senescence connection. *Nat. Rev. Cancer.* 8:450–458. doi:10.1038/nrc2393.

Derossi, D., A.H. Joliot, G. Chassaing, and A. Prochiantz. 1994. The third helix of the Antennapedia homeodomain translocates through biological membranes. *J. Biol. Chem.* 269:10444–10450.

DeSombre, E.R., B. Shafii, R.N. Hanson, P.C. Kuivanen, and A. Hughes. 1992. Estrogen receptor-directed radiotoxicity with Auger electrons: specificity and mean lethal dose. *Cancer Res.* 52:5752–5758.

Dikmen, Z.G., G.C. Gellert, S. Jackson, S. Gryaznov, R. Tressler, P. Dogan, W.E. Wright, and J.W. Shay. 2005. In vivo inhibition of lung cancer by GRN163L: a novel human telomerase inhibitor. *Cancer Res.* 65:7866–7873. doi:10.1158/0008-5472.CAN-05-1215.

Ding, Y., Z. Jiang, K. Saha, C.S. Kim, S.T. Kim, R.F. Landis, and V.M. Rotello. 2014. Gold nanoparticles for nucleic acid delivery. *Mol. Ther. J. Am. Soc. Gene Ther.* 22:1075–1083. doi:10.1038/mt.2014.30.

DiPaola, R.S. 2002. To arrest or not to G2-M cell-cycle arrest. *Clin. Cancer Res.* 8:3311–3314.

Djojosubroto, M.W., A.C. Chin, N. Go, S. Schaetzlein, M.P. Manns, S. Gryaznov, C.B. Harley, and K.L. Rudolph. 2005. Telomerase antagonists GRN163 and GRN163L inhibit tumor growth and increase chemosensitivity of human hepatoma. *Hepatology.* 42:1127–1136. doi:10.1002/hep.20822.

Doherty, G.J., and H.T. McMahon. 2009. Mechanisms of endocytosis. *Annu. Rev. Biochem.* 78:857–902. doi:10.1146/annurev.biochem.78.081307.110540.

Domingos, R.F., M.A. Baalousha, Y. Ju-Nam, M.M. Reid, N. Tufenkji, J.R. Lead, G.G. Leppard, and K.J. Wilkinson. 2009. Characterizing manufactured nanoparticles in the environment:

multimethod determination of particle sizes. *Environ. Sci. Technol.* 43:7277–7284. doi:10.1021/es900249m.

Doss, C.G.P., C. Debajyoti, and S. Debottam. 2012. The impact of gold nanoparticles on hTERT gene expression leading to termination of malignant tumor. *Gene.* 493:140–141. doi:10.1016/j.gene.2011.11.020.

Dreaden, E.C., A.M. Alkilany, X. Huang, C.J. Murphy, and M.A. El-Sayed. 2012. The golden age: gold nanoparticles for biomedicine. *Chem. Soc. Rev.* 41:2740–2779. doi:10.1039/c1cs15237h.

Dulkeith, E., A.C. Morteani, T. Niedereichholz, T.A. Klar, J. Feldmann, S.A. Levi, F.C.J.M. van Veggel, D.N. Reinhoudt, M. Möller, and D.I. Gittins. 2002. Fluorescence quenching of dye molecules near gold nanoparticles: radiative and nonradiative effects. *Phys. Rev. Lett.* 89:203002.

Dykman, L., and N. Khlebtsov. 2012. Gold nanoparticles in biomedical applications: recent advances and perspectives. *Chem. Soc. Rev.* 41:2256–2282. doi:10.1039/c1cs15166e.

Dykman, L.A., and N.G. Khlebtsov. 2014. Uptake of engineered gold nanoparticles into mammalian cells. *Chem. Rev.* 114:1258–1288. doi:10.1021/cr300441a.

Ehling, J., B. Theek, F. Gremse, S. Baetke, D. Möckel, J. Maynard, S.-A. Ricketts, H. Grüll, M. Neeman, R. Knuechel, W. Lederle, F. Kiessling, and T. Lammers. 2014. Micro-CT imaging of tumor angiogenesis: quantitative measures describing micromorphology and vascularization. *Am. J. Pathol.* 184:431–441. doi:10.1016/j.ajpath.2013.10.014.

Eibauer, M., M. Pellanda, Y. Turgay, A. Dubrovsky, A. Wild, and O. Medalia. 2015. Structure and gating of the nuclear pore complex. *Nat. Commun.* 6:7532. doi:10.1038/ncomms8532.

von Eyben, F.E., G. Roviello, T. Kiljunen, C. Uprimny, I. Virgolini, K. Kairemo, and T. Joensuu. 2018. Third-line treatment and ^{177}Lu-PSMA radioligand therapy of metastatic castration-resistant prostate cancer: a systematic review. *Eur. J. Nucl. Med. Mol. Imaging.* 45:496–508. doi:10.1007/s00259-017-3895-x.

Fajkus, J. 2006. Detection of telomerase activity by the TRAP assay and its variants and alternatives. *Clin. Chim. Acta Int. J. Clin. Chem.* 371:25–31. doi:10.1016/j.cca.2006.02.039.

Falzone, N., J.M. Fernández-Varea, G. Flux, and K.A. Vallis. 2015. Monte Carlo evaluation of Auger electron-emitting theranostic radionuclides. *J. Nucl. Med.* 56:1441–1446. doi:10.2967/jnumed.114.153502.

Feng, J., W.D. Funk, S.S. Wang, S.L. Weinrich, A.A. Avilion, C.P. Chiu, R.R. Adams, E. Chang, R.C. Allsopp, and J. Yu. 1995. The RNA component of human telomerase. *Science.* 269:1236–1241.

Fernando, L.P., P.K. Kandel, J. Yu, J. McNeill, P.C. Ackroyd, and K.A. Christensen. 2010. Mechanism of cellular uptake of highly fluorescent conjugated polymer nanoparticles. *Biomacromolecules.* 11:2675–2682. doi:10.1021/bm1007103.

Ferrandon, S., C. Malleval, B. El Hamdani, P. Battiston-Montagne, R. Bolbos, J.-B. Langlois, P. Manas, S.M. Gryaznov, G. Alphonse, J. Honnorat, C. Rodriguez-Lafrasse, and D. Poncet. 2015. Telomerase inhibition improves tumor response to radiotherapy in a murine

orthotopic model of human glioblastoma. *Mol. Cancer*. 14:134. doi:10.1186/s12943-015-0376-3.

Fertil, B., H. Dertinger, A. Courdi, and E.P. Malaise. 1984. Mean inactivation dose: a useful concept for intercomparison of human cell survival curves. *Radiat. Res.* 99:73–84. doi:10.2307/3576448.

Fissan, H., S. Ristig, H. Kaminski, C. Asbach, and M. Epple. 2014. Comparison of different characterization methods for nanoparticle dispersions before and after aerosolization. *Anal. Methods*. 6:7324–7334. doi:10.1039/C4AY01203H.

Fittipaldi, A., A. Ferrari, M. Zoppé, C. Arcangeli, V. Pellegrini, F. Beltram, and M. Giacca. 2003. Cell membrane lipid rafts mediate caveolar endocytosis of HIV-1 Tat fusion proteins. *J. Biol. Chem.* 278:34141–34149. doi:10.1074/jbc.M303045200.

Flynn, R.L., R.C. Centore, R.J. O'Sullivan, R. Rai, A. Tse, Z. Songyang, S. Chang, J. Karlseder, and L. Zou. 2011. TERRA and hnRNPA1 orchestrate an RPA-to-POT1 switch on telomeric single-stranded DNA. *Nature*. 471:532–536. doi:10.1038/nature09772.

Forsbach, A., J.-G. Nemorin, C. Montino, C. Müller, U. Samulowitz, A.P. Vicari, M. Jurk, G.K. Mutwiri, A.M. Krieg, G.B. Lipford, and J. Vollmer. 2008. Identification of RNA sequence motifs stimulating sequence-specific TLR8-dependent immune responses. *J. Immunol. 1950*. 180:3729–3738.

Franken, N.A.P., H.M. Rodermond, J. Stap, J. Haveman, and C. van Bree. 2006. Clonogenic assay of cells in vitro. *Nat. Protoc.* 1:2315–2319. doi:10.1038/nprot.2006.339.

Fu, D., and K. Collins. 2003. Distinct biogenesis pathways for human telomerase RNA and H/ACA small nucleolar RNAs. *Mol. Cell.* 11:1361–1372. doi:10.1016/S1097-2765(03)00196-5.

de la Fuente, J.M., and C.C. Berry. 2005. Tat peptide as an efficient molecule to translocate gold nanoparticles into the cell nucleus. *Bioconjug. Chem.* 16:1176–1180. doi:10.1021/bc050033+.

Gazzaniga, F.S., and E.H. Blackburn. 2014. An antiapoptotic role for telomerase RNA in human immune cells independent of telomere integrity or telomerase enzymatic activity. *Blood*. 124:3675–3684. doi:10.1182/blood-2014-06-582254.

Gellert, G.C., Z.G. Dikmen, W.E. Wright, S. Gryaznov, and J.W. Shay. 2006. Effects of a novel telomerase inhibitor, GRN163L, in human breast cancer. *Breast Cancer Res. Treat.* 96:73–81. doi:10.1007/s10549-005-9043-5.

Gentile, F., C. Chiappini, D. Fine, R.C. Bhavane, M.S. Peluccio, M.M.-C. Cheng, X. Liu, M. Ferrari, and P. Decuzzi. 2008. The effect of shape on the margination dynamics of non-neutrally buoyant particles in two-dimensional shear flows. *J. Biomech.* 41:2312–2318. doi:10.1016/j.jbiomech.2008.03.021.

Ghosh, A., G. Saginc, S.C. Leow, E. Khattar, E.M. Shin, T.D. Yan, M. Wong, Z. Zhang, G. Li, W.-K. Sung, J. Zhou, W.J. Chng, S. Li, E. Liu, and V. Tergaonkar. 2012. Telomerase directly regulates NF-κB-dependent transcription. *Nat. Cell Biol.* 14:1270–1281. doi:10.1038/ncb2621.

Ghosh, P., G. Han, M. De, C.K. Kim, and V.M. Rotello. 2008. Gold nanoparticles in delivery applications. *Adv. Drug Deliv. Rev.* 60:1307–1315. doi:10.1016/j.addr.2008.03.016.

Giljohann, D.A., D.S. Seferos, W.L. Daniel, M.D. Massich, P.C. Patel, and C.A. Mirkin. 2010. Gold nanoparticles for biology and medicine. *Angew. Chem.* 49:3280–3294. doi:10.1002/anie.200904359.

Giljohann, D.A., D.S. Seferos, P.C. Patel, J.E. Millstone, N.L. Rosi, and C.A. Mirkin. 2007. Oligonucleotide loading determines cellular uptake of DNA-modified gold nanoparticles. *Nano Lett.* 7:3818–3821. doi:10.1021/nl072471q.

Giljohann, D.A., D.S. Seferos, A.E. Prigodich, P.C. Patel, and C.A. Mirkin. 2009. Gene regulation with polyvalent siRNA−nanoparticle conjugates. *J. Am. Chem. Soc.* 131:2072–2073. doi:10.1021/ja808719p.

Gill, M.R., N. Falzone, Y. Du, and K.A. Vallis. 2017. Targeted radionuclide therapy in combined-modality regimens. *Lancet Oncol.* 18:e414–e423. doi:10.1016/S1470-2045(17)30379-0.

Gill, M.R., J.U. Menon, P.J. Jarman, J. Owen, I. Skaripa-Koukelli, S. Able, J.A. Thomas, R.C. Carlisle, and K.A. Vallis. 2018. ^{111}In-labelled polymeric nanoparticles incorporating a ruthenium-based radiosensitize for EGFR-targeted combination therapy in oesophageal cancer cells. *Nanoscale*. In press. doi:10.1039/c7nr09606b.

Global Burden of Disease Cancer Collaboration, C. Fitzmaurice, T.F. Akinyemiju, F.H. Al Lami, T. Alam, R. Alizadeh-Navaei, C. Allen, U. Alsharif, N. Alvis-Guzman, E. Amini, B.O. Anderson, O. Aremu, A. Artaman, S.W. Asgedom, R. Assadi, T.M. Atey, L. Avila-Burgos, A. Awasthi, H.O. Ba Saleem, A. Barac, J.R. Bennett, I.M. Bensenor, N. Bhakta, H. Brenner, L. Cahuana-Hurtado, C.A. Castañeda-Orjuela, F. Catalá-López, J.-Y.J. Choi, D.J. Christopher, S.-C. Chung, M.P. Curado, L. Dandona, R. Dandona, J. das Neves, S. Dey, S.D. Dharmaratne, D.T. Doku, T.R. Driscoll, M. Dubey, H. Ebrahimi, D. Edessa, Z. El-Khatib, A.Y. Endries, F. Fischer, L.M. Force, K.J. Foreman, S.W. Gebrehiwot, S.V. Gopalani, G. Grosso, R. Gupta, B. Gyawali, R.R. Hamadeh, S. Hamidi, J. Harvey, H.Y. Hassen, R.J. Hay, S.I. Hay, B. Heibati, M.K. Hiluf, N. Horita, H.D. Hosgood, O.S. Ilesanmi, K. Innos, F. Islami, M.B. Jakovljevic, S.C. Johnson, J.B. Jonas, A. Kasaeian, T.D. Kassa, Y.S. Khader, E.A. Khan, G. Khan, Y.-H. Khang, M.H. Khosravi, J. Khubchandani, J.A. Kopec, G.A. Kumar, M. Kutz, D.P. Lad, A. Lafranconi, Q. Lan, Y. Legesse, J. Leigh, S. Linn, R. Lunevicius, A. Majeed, R. Malekzadeh, D.C. Malta, L.G. Mantovani, B.J. McMahon, T. Meier, Y.A. Melaku, M. Melku, P. Memiah, W. Mendoza, T.J. Meretoja, H.B. Mezgebe, T.R. Miller, et al. 2018. Global, regional, and national cancer incidence, mortality, years of life lost, years lived with disability, and disability-adjusted life-years for 29 cancer groups, 1990 to 2016: a systematic analysis for the global burden of disease study. *JAMA Oncol.* doi:10.1001/jamaoncol.2018.2706.

Goldblatt, E.M., P.A. Erickson, E.R. Gentry, S.M. Gryaznov, and B.-S. Herbert. 2009a. Lipid-conjugated telomerase template antagonists sensitize resistant HER2-positive breast cancer cells to trastuzumab. *Breast Cancer Res. Treat.* 118:21–32. doi:10.1007/s10549-008-0201-4.

Goldblatt, E.M., E.R. Gentry, M.J. Fox, S.M. Gryaznov, C. Shen, and B.-S. Herbert. 2009b. The telomerase template antagonist GRN163L alters MDA-MB-231 breast cancer cell morphology, inhibits growth, and augments the effects of paclitaxel. *Mol. Cancer Ther.* 8:2027–2035. doi:10.1158/1535-7163.MCT-08-1188.

Gomez-Millan, J., E.M. Goldblatt, S.M. Gryaznov, M.S. Mendonca, and B.-S. Herbert. 2007. Specific telomere dysfunction induced by GRN163L increases radiation sensitivity in breast cancer cells. *Int. J. Radiat. Oncol. Biol. Phys.* 67:897–905. doi:10.1016/j.ijrobp.2006.09.038.

Goytisolo, F.A., E. Samper, J. Martín-Caballero, P. Finnon, E. Herrera, J.M. Flores, S.D. Bouffler, and M.A. Blasco. 2000. Short telomeres result in organismal hypersensitivity to ionizing radiation in mammals. *J. Exp. Med.* 192:1625–1636. doi:10.1084/jem.192.11.1625.

Graham, S.M., R. Carlisle, J.J. Choi, M. Stevenson, A.R. Shah, R.S. Myers, K. Fisher, M.-B. Peregrino, L. Seymour, and C.C. Coussios. 2014. Inertial cavitation to non-invasively trigger and monitor intratumoral release of drug from intravenously delivered liposomes. *J. Control. Release* 178:101–107. doi:10.1016/j.jconrel.2013.12.016.

Greider, C.W., and E.H. Blackburn. 1985. Identification of a specific telomere terminal transferase activity in Tetrahymena extracts. *Cell.* 43:405–413.

Hahn, W.C., S.A. Stewart, M.W. Brooks, S.G. York, E. Eaton, A. Kurachi, R.L. Beijersbergen, J.H. Knoll, M. Meyerson, and R.A. Weinberg. 1999. Inhibition of telomerase limits the growth of human cancer cells. *Nat. Med.* 5:1164–1170. doi:10.1038/13495.

Haiss, W., N.T.K. Thanh, J. Aveyard, and D.G. Fernig. 2007. Determination of size and concentration of gold nanoparticles from UV−Vis spectra. *Anal. Chem.* 79:4215–4221. doi:10.1021/ac0702084.

Hanahan, D., and R.A. Weinberg. 2011. Hallmarks of cancer: the next generation. *Cell.* 144:646–674. doi:10.1016/j.cell.2011.02.013.

Harris, J.M., and R.B. Chess. 2003. Effect of pegylation on pharmaceuticals. *Nat. Rev. Drug Discov.* 2:214–221. doi:10.1038/nrd1033.

Heil, F., H. Hemmi, H. Hochrein, F. Ampenberger, C. Kirschning, S. Akira, G. Lipford, H. Wagner, and S. Bauer. 2004. Species-specific recognition of single-stranded RNA via toll-like receptor 7 and 8. *Science.* 303:1526–1529. doi:10.1126/science.1093620.

Her, S., D.A. Jaffray, and C. Allen. 2017. Gold nanoparticles for applications in cancer radiotherapy: Mechanisms and recent advancements. *Adv. Drug Deliv. Rev.* 109:84–101. doi:10.1016/j.addr.2015.12.012.

Herbert, B., A.E. Pitts, S.I. Baker, S.E. Hamilton, W.E. Wright, J.W. Shay, and D.R. Corey. 1999. Inhibition of human telomerase in immortal human cells leads to progressive telomere shortening and cell death. *Proc. Natl. Acad. Sci. U. S. A.* 96:14276–14281.

Herbert, B.-S., G.C. Gellert, A. Hochreiter, K. Pongracz, W.E. Wright, D. Zielinska, A.C. Chin, C.B. Harley, J.W. Shay, and S.M. Gryaznov. 2005. Lipid modification of GRN163, an N3'-->P5' thio-phosphoramidate oligonucleotide, enhances the potency of telomerase inhibition. *Oncogene.* 24:5262–5268. doi:10.1038/sj.onc.1208760.

Hermanson, G.T. 2010. Bioconjugate techniques. Academic Press. 1233 pp.

Hochreiter, A.E., H. Xiao, E.M. Goldblatt, S.M. Gryaznov, K.D. Miller, S. Badve, G.W. Sledge, and B.-S. Herbert. 2006. Telomerase template antagonist GRN163L disrupts telomere maintenance, tumor growth, and metastasis of breast cancer. *Clin. Cancer Res.* 12:3184–3192. doi:10.1158/1078-0432.CCR-05-2760.

Holt, S.E., D.L. Aisner, J. Baur, V.M. Tesmer, M. Dy, M. Ouellette, J.B. Trager, G.B. Morin, D.O. Toft, J.W. Shay, W.E. Wright, and M.A. White. 1999. Functional requirement of p23 and Hsp90 in telomerase complexes. *Genes Dev.* 13:817–826.

Huang, C.-Y., M.H. Pourgholami, and B.J. Allen. 2012a. Optimizing radioimmunoconjugate delivery in the treatment of solid tumor. *Cancer Treat. Rev.* 38:854–860. doi:10.1016/j.ctrv.2011.12.005.

Huang, K., H. Ma, J. Liu, S. Huo, A. Kumar, T. Wei, X. Zhang, S. Jin, Y. Gan, P.C. Wang, S. He, X. Zhang, and X.-J. Liang. 2012b. Size-dependent localization and penetration of ultrasmall gold nanoparticles in cancer cells, multicellular spheroids, and tumors in vivo. *ACS Nano.* 6:4483–4493. doi:10.1021/nn301282m.

Huang, Y., J. Hong, S. Zheng, Y. Ding, S. Guo, H. Zhang, X. Zhang, Q. Du, and Z. Liang. 2011. Elimination pathways of systemically delivered siRNA. *Mol. Ther.* 19:381–385. doi:10.1038/mt.2010.266.

Huffman, K.E., S.D. Levene, V.M. Tesmer, J.W. Shay, and W.E. Wright. 2000. Telomere shortening is proportional to the size of the G-rich telomeric 3'-overhang. *J. Biol. Chem.* 275:19719–19722. doi:10.1074/jbc.M002843200.

Huo, S., S. Jin, X. Ma, X. Xue, K. Yang, A. Kumar, P.C. Wang, J. Zhang, Z. Hu, and X.-J. Liang. 2014. Ultrasmall gold nanoparticles as carriers for nucleus-based gene therapy due to size-dependent nuclear entry. *ACS Nano.* 8:5852–5862. doi:10.1021/nn5008572.

Hurst, S.J., A.K.R. Lytton-Jean, and C.A. Mirkin. 2006. Maximizing DNA loading on a range of gold nanoparticle sizes. *Anal. Chem.* 78:8313–8318. doi:10.1021/ac0613582.

Imstepf, S., V. Pierroz, P. Raposinho, M. Bauwens, M. Felber, T. Fox, A.B. Shapiro, R. Freudenberg, C. Fernandes, S. Gama, G. Gasser, F. Motthagy, I.R. Santos, and R. Alberto. 2015. Nuclear targeting with an Auger electron emitter potentiates the action of a widely used antineoplastic drug. *Bioconjug. Chem.* 26:2397–2407. doi:10.1021/acs.bioconjchem.5b00466.

Jackson, M.R., B.M. Bavelaar, P. Waghorn, M.R. Gill, A.H. El-Sagheer, T. Brown, and K.A. Vallis. 2018. Dual-action ^{111}In-labelled oligonucleotides against the RNA subunit of telomerase inhibit enzymatic activity and are radiotoxic against telomerase-positive cancer cells. *Cancer Res.* Submitted.

Jafri, M.A., S.A. Ansari, M.H. Alqahtani, and J.W. Shay. 2016. Roles of telomeres and telomerase in cancer, and advances in telomerase-targeted therapies. *Genome Med.* 8:69. doi:10.1186/s13073-016-0324-x.

Ji, X., C. Xie, M. Fang, F. Zhou, W. Zhang, M. Zhang, and Y. Zhou. 2006. Efficient inhibition of human telomerase activity by antisense oligonucleotides sensitizes cancer cells to radiotherapy. *Acta Pharmacol. Sin.* 27:1185–1191. doi:10.1111/j.1745-7254.2006.00417.x.

Jiang, J., Y. Wang, L. Sušac, H. Chan, R. Basu, Z.H. Zhou, and J. Feigon. 2018. Structure of telomerase with telomeric DNA. *Cell.* 173:1179-1190.e13. doi:10.1016/j.cell.2018.04.038.

Jin, R., G. Wu, Z. Li, C.A. Mirkin, and G.C. Schatz. 2003. What controls the melting properties of DNA-linked gold nanoparticle assemblies? *J. Am. Chem. Soc.* 125:1643–1654. doi:10.1021/ja021096v.

Juliano, R.L. 2016. The delivery of therapeutic oligonucleotides. *Nucleic Acids Res.* gkw236. doi:10.1093/nar/gkw236.

Juliano, R.L., X. Ming, and O. Nakagawa. 2012. Cellular uptake and intracellular trafficking of antisense and siRNA oligonucleotides. *Bioconjug. Chem.* 23:147–157. doi:10.1021/bc200377d.

Kanasty, R., J.R. Dorkin, A. Vegas, and D. Anderson. 2013. Delivery materials for siRNA therapeutics. *Nat. Mater.* 12:967–977. doi:10.1038/nmat3765.

Kaplan, I.M., J.S. Wadia, and S.F. Dowdy. 2005. Cationic TAT peptide transduction domain enters cells by macropinocytosis. *J. Control. Release* 102:247–253. doi:10.1016/j.jconrel.2004.10.018.

Kassis, A.I. 2004. The amazing world of Auger electrons. *Int. J. Radiat. Biol.* 80:789–803. doi:10.1080/09553000400017663.

Kauffman, W.B., T. Fuselier, J. He, and W.C. Wimley. 2015. Mechanism matters: A taxonomy of cell penetrating peptides. *Trends Biochem. Sci.* 40:749–764. doi:10.1016/j.tibs.2015.10.004.

Kedde, M., C. le Sage, A. Duursma, E. Zlotorynski, B. van Leeuwen, W. Nijkamp, R. Beijersbergen, and R. Agami. 2006. Telomerase-independent regulation of ATR by human telomerase RNA. *J. Biol. Chem.* 281:40503–40514. doi:10.1074/jbc.M607676200.

Keefe, A.D., S. Pai, and A. Ellington. 2010. Aptamers as therapeutics. *Nat. Rev. Drug Discov.* 9:537–550. doi:10.1038/nrd3141.

Khvorova, A., and J.K. Watts. 2017. The chemical evolution of oligonucleotide therapies of clinical utility. *Nat. Biotechnol.* 35:238–248. doi:10.1038/nbt.3765.

Kisak, E.T., B. Coldren, C.A. Evans, and C.B. and J.A. Zasadzinski. 2003. The vesosome - a multicompartment drug delivery vehicle. *Curr. Med. Chem.*

Kiss, T., E. Fayet-Lebaron, and B.E. Jády. 2010. Box H/ACA small ribonucleoproteins. *Mol. Cell.* 37:597–606. doi:10.1016/j.molcel.2010.01.032.

Koller, E., T.M. Vincent, A. Chappell, S. De, M. Manoharan, and C.F. Bennett. 2011. Mechanisms of single-stranded phosphorothioate modified antisense oligonucleotide accumulation in hepatocytes. *Nucleic Acids Res.* 39:4795–4807. doi:10.1093/nar/gkr089.

Kortylewicz, Z.P., Y. Kimura, K. Inoue, E. Mack, and J. Baranowska-Kortylewicz. 2012. Radiolabeled cyclosaligenyl monophosphates of 5-iodo-2'-deoxyuridine, 5-iodo-3'-fluoro-2',3'-dideoxyuridine, and 3'-fluorothymidine for molecular radiotherapy of cancer: synthesis and biological evaluation. *J. Med. Chem.* 55:2649–2671. doi:10.1021/jm201482p.

Kotzerke, J., R. Punzet, R. Runge, S. Ferl, L. Oehme, G. Wunderlich, and R. Freudenberg. 2014. 99mTc-Labeled HYNIC-DAPI causes plasmid DNA damage with high efficiency. *PLOS ONE.* 9:e104653. doi:10.1371/journal.pone.0104653.

Koziel, J.E., and B.-S. Herbert. 2015. The telomerase inhibitor imetelstat alone, and in combination with trastuzumab, decreases the cancer stem cell population and self-renewal of HER2+ breast cancer cells. *Breast Cancer Res. Treat.* 149:607–618. doi:10.1007/s10549-015-3270-1.

Krpetić, Ž., S. Saleemi, I.A. Prior, V. Sée, R. Qureshi, and M. Brust. 2011. Negotiation of intracellular membrane barriers by TAT-modified gold nanoparticles. *ACS Nano*. 5:5195–5201. doi:10.1021/nn201369k.

Kumar, R., H. Korideck, W. Ngwa, R.I. Berbeco, G.M. Makrigiorgos, and S. Sridhar. 2013. Third generation gold nanoplatform optimized for radiation therapy. *Transl. Cancer Res.* 2. doi:10.3978/j.issn.2218-676X.2013.07.02.

Kwan, J.J., R. Myers, C.M. Coviello, S.M. Graham, A.R. Shah, E. Stride, R.C. Carlisle, and C.C. Coussios. 2015. Ultrasound-propelled nanocups for drug delivery. *Small* 11:5305–5314. doi:10.1002/smll.201501322.

Lai, C.K., J.R. Mitchell, and K. Collins. 2001. RNA binding domain of telomerase reverse transcriptase. *Mol. Cell. Biol.* 21:990–1000. doi:10.1128/MCB.21.4.990-1000.2001.

de Lange, T. 2009. How telomeres solve the end-protection problem. *Science*. 326:948. doi:10.1126/science.1170633.

Larson, S.M., J.A. Carrasquillo, N.-K.V. Cheung, and O.W. Press. 2015. Radioimmunotherapy of human tumours. *Nat. Rev. Cancer*. 15:347–360. doi:10.1038/nrc3925.

Layzer, J.M., A.P. McCaffrey, A.K. Tanner, Z. Huang, M.A. Kay, and B.A. Sullenger. 2004. In vivo activity of nuclease-resistant siRNAs. *RNA N. Y. N.* 10:766–771.

Lea-Banks, H., B. Teo, E. Stride, and C.C. Coussios. 2016. The effect of particle density on ultrasound-mediated transport of nanoparticles. *Phys. Med. Biol.* 61:7906. doi:10.1088/0031-9155/61/22/7906.

Lee, B.Q., T. Kibédi, and A.E. Stuchbery. 2015. Auger yield calculations for medical radioisotopes. *EPJ Web Conf.* 91:00007. doi:10.1051/epjconf/20159100007.

Lee, H., H. Fonge, B. Hoang, R.M. Reilly, and C. Allen. 2010. The effects of particle size and molecular targeting on the intratumoral and subcellular distribution of polymeric nanoparticles. *Mol. Pharm.* 7:1195–1208. doi:10.1021/mp100038h.

Lei, Q., C. Ren, X. Su, and Y. Ma. 2015. Crowding-induced cooperativity in DNA surface hybridization. *Sci. Rep.* 5:9217. doi:10.1038/srep09217.

Li, Y., and V. Tergaonkar. 2014. Noncanonical functions of telomerase: implications in telomerase-targeted cancer therapies. *Cancer Res.* 74:1639–1644. doi:10.1158/0008-5472.CAN-13-3568.

Lin, C.-Y., J.-R. Li, H.-C. Tseng, M.-F. Wu, and W.-L. Lin. 2012. Enhancement of focused ultrasound with microbubbles on the treatments of anticancer nanodrug in mouse tumors. *Nanomedicine* 8:900–907. doi:10.1016/j.nano.2011.10.005.

Lin, C.-Y., T.-M. Liu, C.-Y. Chen, Y.-L. Huang, W.-K. Huang, C.-K. Sun, F.-H. Chang, and W.-L. Lin. 2010. Quantitative and qualitative investigation into the impact of focused ultrasound with microbubbles on the triggered release of nanoparticles from vasculature in mouse tumors. *J. Control. Release* 146:291–298. doi:10.1016/j.jconrel.2010.05.033.

Lin, J., and A. Alexander-Katz. 2013. Cell membranes open "doors" for cationic nanoparticles/biomolecules: insights into uptake kinetics. *ACS Nano.* 7:10799–10808. doi:10.1021/nn4040553.

Lindow, M., and S. Kauppinen. 2012. Discovering the first microRNA-targeted drug. *J. Cell Biol.* 199:407–412. doi:10.1083/jcb.201208082.

Liu, J., and Y. Lu. 2003. A colorimetric lead biosensor using DNAzyme-directed assembly of gold nanoparticles. *J. Am. Chem. Soc.* 125:6642–6643. doi:10.1021/ja034775u.

Liu, M., R.F. Wang, C.L. Zhang, P. Yan, M.M. Yu, L.J. Di, H.J. Liu, and F.Q. Guo. 2007. Noninvasive imaging of human telomerase reverse transcriptase (hTERT) messenger RNA with ^{99m}Tc-radiolabeled antisense probes in malignant tumors. *J. Nucl. Med.* 48:2028–2036. doi:10.2967/jnumed.107.042622.

Liu, Y., G. Liu, and D.J. Hnatowich. 2010. A brief review of chelators for radiolabeling oligomers. *Materials.* 3:3204–3217. doi:10.3390/ma3053204.

Lorenzer, C., M. Dirin, A.-M. Winkler, V. Baumann, and J. Winkler. 2015. Going beyond the liver: Progress and challenges of targeted delivery of siRNA therapeutics. *J. Control. Release* 203:1–15. doi:10.1016/j.jconrel.2015.02.003.

Ma, Y., Z. Wang, Y. Ma, Z. Han, M. Zhang, H. Chen, and Y. Gu. 2018. A telomerase-responsive DNA icosahedron for precise delivery of platinum nanodrugs to cisplatin-resistant cancer. *Angew. Chem.* doi:10.1002/anie.201801195.

Ma, Y., Z. Wang, M. Zhang, Z. Han, D. Chen, Q. Zhu, W. Gao, Z. Qian, and Y. Gu. 2016. A telomerase-specific doxorubicin-releasing molecular beacon for cancer theranostics. *Angew. Chem.* 55:3304–3308. doi:10.1002/anie.201509182.

Mannaris, C., B.M. Teo, A. Seth, L. Bau, C. Coussios, and E. Stride. 2018. Gas-stabilizing gold nanocones for acoustically mediated drug delivery. *Adv. Healthc. Mater.* e1800184. doi:10.1002/adhm.201800184.

Manson, J., D. Kumar, B.J. Meenan, and D. Dixon. 2011. Polyethylene glycol functionalized gold nanoparticles: the influence of capping density on stability in various media. *Gold Bull.* 44:99–105. doi:10.1007/s13404-011-0015-8.

Marian, C.O., S.K. Cho, B.M. McEllin, E.A. Maher, K.J. Hatanpaa, C.J. Madden, B.E. Mickey, W.E. Wright, J.W. Shay, and R.M. Bachoo. 2010. The telomerase antagonist, imetelstat, efficiently targets glioblastoma tumor-initiating cells leading to decreased proliferation and tumor growth. *Clin. Cancer Res.* 16:154–163. doi:10.1158/1078-0432.CCR-09-2850.

Martínez, P., and M.A. Blasco. 2011. Telomeric and extra-telomeric roles for telomerase and the telomere-binding proteins. *Nat. Rev. Cancer.* 11:161–176. doi:10.1038/nrc3025.

Matsumura, Y., and H. Maeda. 1986. A new concept for macromolecular therapeutics in cancer chemotherapy: mechanism of tumoritropic accumulation of proteins and the antitumor agent smancs. *Cancer Res.* 46:6387–6392.

Melancon, M.P., W. Lu, Z. Yang, R. Zhang, Z. Cheng, A.M. Elliot, J. Stafford, T. Olson, J.Z. Zhang, and C. Li. 2008. In vitro and in vivo targeting of hollow gold nanoshells directed at

epidermal growth factor receptor for photothermal ablation therapy. *Mol. Cancer Ther.* 7:1730–1739. doi:10.1158/1535-7163.MCT-08-0016.

Mirkin, C.A., R.L. Letsinger, R.C. Mucic, and J.J. Storhoff. 1996. A DNA-based method for rationally assembling nanoparticles into macroscopic materials. *Nature.* 382:607–609. doi:10.1038/382607a0.

Mitchell, J.R., J. Cheng, and K. Collins. 1999. A box H/ACA small nucleolar RNA-like domain at the human telomerase RNA 3' end. *Mol. Cell. Biol.* 19:567–576. doi:10.1128/MCB.19.1.567.

Mo, S., R. Carlisle, R. Laga, R. Myers, S. Graham, R. Cawood, K. Ulbrich, L. Seymour, and C.-C. Coussios. 2015. Increasing the density of nanomedicines improves their ultrasound-mediated delivery to tumours. *J. Control. Release* 210:10–18. doi:10.1016/j.jconrel.2015.05.265.

Mo, S., C.-C. Coussios, L. Seymour, and R. Carlisle. 2012. Ultrasound-enhanced drug delivery for cancer. *Expert Opin. Drug Deliv.* 9:1525–1538. doi:10.1517/17425247.2012.739603.

Morshed, R.A., M.E. Muroski, Q. Dai, M.L. Wegscheid, B. Auffinger, D. Yu, Y. Han, L. Zhang, M. Wu, Y. Cheng, and M.S. Lesniak. 2016. Cell-penetrating peptide-modified gold nanoparticles for the delivery of doxorubicin to brain metastatic breast cancer. *Mol. Pharm.* 13:1843–1854. doi:10.1021/acs.molpharmaceut.6b00004.

Myers, R., C. Coviello, P. Erbs, J. Foloppe, C. Rowe, J. Kwan, C. Crake, S. Finn, E. Jackson, J.-M. Balloul, C. Story, C. Coussios, and R. Carlisle. 2016. Polymeric cups for cavitation-mediated delivery of oncolytic vaccinia virus. *Mol. Ther.* 24:1627–1633. doi:10.1038/mt.2016.139.

Nakamura, A.J., V.A. Rao, Y. Pommier, and W.M. Bonner. 2010. The complexity of phosphorylated H2AX foci formation and DNA repair assembly at DNA double-strand breaks. *Cell Cycle.* 9:389–397. doi:10.4161/cc.9.2.10475.

Nakamura, T.M., G.B. Morin, K.B. Chapman, S.L. Weinrich, W.H. Andrews, J. Lingner, C.B. Harley, and T.R. Cech. 1997. Telomerase catalytic subunit homologs from fission yeast and human. *Science.* 277:955–959. doi:10.1126/science.277.5328.955.

Nakamura, Y., A. Mochida, P.L. Choyke, and H. Kobayashi. 2016. Nanodrug delivery: Is the enhanced permeability and retention effect sufficient for curing cancer? *Bioconjug. Chem.* 27:2225–2238. doi:10.1021/acs.bioconjchem.6b00437.

Nam, J.-M., C.S. Thaxton, and C.A. Mirkin. 2003. Nanoparticle-based bio-bar codes for the ultrasensitive detection of proteins. *Science.* 301:1884–1886. doi:10.1126/science.1088755.

Nandakumar, J., and T.R. Cech. 2013. Finding the end: recruitment of telomerase to telomeres. *Nat. Rev. Mol. Cell Biol.* 14:69–82. doi:10.1038/nrm3505.

Nativo, P., I.A. Prior, and M. Brust. 2008. Uptake and intracellular fate of surface-modified gold nanoparticles. *ACS Nano.* 2:1639–1644. doi:10.1021/nn800330a.

Nel, A.E., L. Mädler, D. Velegol, T. Xia, E.M.V. Hoek, P. Somasundaran, F. Klaessig, V. Castranova, and M. Thompson. 2009. Understanding biophysicochemical interactions at the nano-bio interface. *Nat. Mater.* 8:543–557. doi:10.1038/nmat2442.

Ng, Q.K.T., C.I. Olariu, M. Yaffee, V.F. Taelman, N. Marincek, T. Krause, L. Meier, and M.A. Walter. 2014. Indium-111 labeled gold nanoparticles for in-vivo molecular targeting. *Biomaterials*. 35:7050–7057. doi:10.1016/j.biomaterials.2014.04.098.

Ngo Ndjock Mbong, G., Y. Lu, C. Chan, Z. Cai, P. Liu, A.J. Boyle, M.A. Winnik, and R.M. Reilly. 2015. Trastuzumab labeled to high specific activity with (111)In by site-specific conjugation to a metal-chelating polymer exhibits amplified Auger electron-mediated cytotoxicity on HER2-positive breast cancer cells. *Mol. Pharm.* 12:1951–1960. doi:10.1021/mp5007618.

Nguyen, T.H.D., J. Tam, R.A. Wu, B.J. Greber, D. Toso, E. Nogales, and K. Collins. 2018. Cryo-EM structure of substrate-bound human telomerase holoenzyme. *Nature*. 1. doi:10.1038/s41586-018-0062-x.

Norton, J.C., M.A. Piatyszek, W.E. Wright, J.W. Shay, and D.R. Corey. 1996. Inhibition of human telomerase activity by peptide nucleic acids. *Nat. Biotechnol.* 14:615–619. doi:10.1038/nbt0596-615.

Nykypanchuk, D., M.M. Maye, D. van der Lelie, and O. Gang. 2008. DNA-guided crystallization of colloidal nanoparticles. *Nature*. 451:549–552. doi:10.1038/nature06560.

Oehlke, J., A. Scheller, B. Wiesner, E. Krause, M. Beyermann, E. Klauschenz, M. Melzig, and M. Bienert. 1998. Cellular uptake of an alpha-helical amphipathic model peptide with the potential to deliver polar compounds into the cell interior non-endocytically. *Biochim. Biophys. Acta*. 1414:127–139.

Oishi, M., J. Nakaogami, T. Ishii, and Y. Nagasaki. 2006. Smart PEGylated gold nanoparticles for the cytoplasmic delivery of siRNA to induce enhanced gene silencing. *Chem. Lett.* 35:1046–1047. doi:10.1246/cl.2006.1046.

O'Sullivan, R.J., and J. Karlseder. 2010. Telomeres: protecting chromosomes against genome instability. *Nat. Rev. Mol. Cell Biol.* 11:171–181. doi:10.1038/nrm2848.

Pakiari, A.H., and Z. Jamshidi. 2010. Nature and strength of M-S bonds (m = Au, Ag, and Cu) in binary alloy gold clusters. *J. Phys. Chem. A*. 114:9212–9221. doi:10.1021/jp100423b.

Paleos, C.M., D. Tsiourvas, Z. Sideratou, and L. Tziveleka. 2004. Acid- and salt-triggered multifunctional poly(propylene imine) dendrimer as a prospective drug delivery system. *Biomacromolecules*. 5:524–529. doi:10.1021/bm030068h.

Park, J.-I., A.S. Venteicher, J.Y. Hong, J. Choi, S. Jun, M. Shkreli, W. Chang, Z. Meng, P. Cheung, H. Ji, M. McLaughlin, T.D. Veenstra, R. Nusse, P.D. McCrea, and S.E. Artandi. 2009. Telomerase modulates Wnt signalling by association with target gene chromatin. *Nature*. 460:66–72. doi:10.1038/nature08137.

Park, S.-J., T.A. Taton, and C.A. Mirkin. 2002. Array-based electrical detection of DNA with nanoparticle probes. *Science*. 295:1503–1506. doi:10.1126/science.1067003.

Parker, C., S. Nilsson, D. Heinrich, S.I. Helle, J.M. O'Sullivan, S.D. Fosså, A. Chodacki, P. Wiechno, J. Logue, M. Seke, A. Widmark, D.C. Johannessen, P. Hoskin, D. Bottomley, N.D. James, A. Solberg, I. Syndikus, J. Kliment, S. Wedel, S. Boehmer, M. Dall'Oglio, L. Franzén, R. Coleman, N.J. Vogelzang, C.G. O'Bryan-Tear, K. Staudacher, J. Garcia-Vargas, M. Shan, Ø.S. Bruland, O. Sartor, and ALSYMPCA Investigators. 2013. Alpha emitter radium-223

and survival in metastatic prostate cancer. *N. Engl. J. Med.* 369:213–223. doi:10.1056/NEJMoa1213755.

Parodi, A., N. Quattrocchi, A.L. van de Ven, C. Chiappini, M. Evangelopoulos, J.O. Martinez, B.S. Brown, S.Z. Khaled, I.K. Yazdi, M.V. Enzo, L. Isenhart, M. Ferrari, and E. Tasciotti. 2013. Synthetic nanoparticles functionalized with biomimetic leukocyte membranes possess cell-like functions. *Nat. Nanotechnol.* 8:61–68. doi:10.1038/nnano.2012.212.

Patel, H.M., and S.M. Moghimi. 1998. Serum-mediated recognition of liposomes by phagocytic cells of the reticuloendothelial system - The concept of tissue specificity. *Adv. Drug Deliv. Rev.* 32:45–60.

Patel, P.C., D.A. Giljohann, D.S. Seferos, and C.A. Mirkin. 2008. Peptide antisense nanoparticles. *Proc. Natl. Acad. Sci.* 105:17222–17226. doi:10.1073/pnas.0801609105.

Pitts, A.E., and D.R. Corey. 1998. Inhibition of human telomerase by 2'-O-methyl-RNA. *Proc. Natl. Acad. Sci. U. S. A.* 95:11549–11554.

Pooga, M., M. Hällbrink, M. Zorko, and U. Langel. 1998. Cell penetration by transportan. *FASEB* 12:67–77.

Pouget, J.-P., C. Lozza, E. Deshayes, V. Boudousq, and I. Navarro-Teulon. 2015. Introduction to radiobiology of targeted radionuclide therapy. *Front. Med.* 2. doi:10.3389/fmed.2015.00012.

Pouget, J.-P., I. Navarro-Teulon, M. Bardiès, N. Chouin, G. Cartron, A. Pèlegrin, and D. Azria. 2011. Clinical radioimmunotherapy—the role of radiobiology. *Nat. Rev. Clin. Oncol.* 8:720–734. doi:10.1038/nrclinonc.2011.160.

Pratt, B., and S. Evan. 2007. Physics principles in the clinical use of radioisotopes. *In* Radiotherapy in practice - radioisotope therapy. Oxford University Press, Oxford, United Kingdom.

Rahbar, K., H. Ahmadzadehfar, C. Kratochwil, U. Haberkorn, M. Schäfers, M. Essler, R.P. Baum, H.R. Kulkarni, M. Schmidt, A. Drzezga, P. Bartenstein, A. Pfestroff, M. Luster, U. Lützen, M. Marx, V. Prasad, W. Brenner, A. Heinzel, F.M. Mottaghy, J. Ruf, P.T. Meyer, M. Heuschkel, M. Eveslage, M. Bögemann, W.P. Fendler, and B.J. Krause. 2017. German multicenter study investigating ^{177}Lu-PSMA-617 radioligand therapy in advanced prostate cancer patients. *J. Nucl. Med.* 58:85–90. doi:10.2967/jnumed.116.183194.

Ram, R., O. Uziel, O. Eldan, E. Fenig, E. Beery, S. Lichtenberg, Y. Nordenberg, and M. Lahav. 2009. Ionizing radiation up-regulates telomerase activity in cancer cell lines by post-translational mechanism via ras/phosphatidylinositol 3-kinase/Akt pathway. *Clin. Cancer Res.* 15:914–923. doi:10.1158/1078-0432.CCR-08-0792.

Robart, A.R., and K. Collins. 2011. Human telomerase domain interactions capture DNA for TEN domain-dependent processive elongation. *Mol. Cell.* 42:308–318. doi:10.1016/j.molcel.2011.03.012.

Rodriguez, P.L., T. Harada, D.A. Christian, D.A. Pantano, R.K. Tsai, and D.E. Discher. 2013. Minimal "self" peptides that inhibit phagocytic clearance and enhance delivery of nanoparticles. *Science.* 339:971–975. doi:10.1126/science.1229568.

Rogakou, E.P., D.R. Pilch, A.H. Orr, V.S. Ivanova, and W.M. Bonner. 1998. DNA double-stranded breaks induce histone H2AX phosphorylation on serine 139. *J. Biol. Chem.* 273:5858–5868.

Rojas, B., C. Hooker, D.R. McGowan, and M.J. Guy. 2015. Five years of molecular radiotherapy growth in the UK: survey results from 2007 to 2012. *Nucl. Med. Commun.* 36:761–765. doi:10.1097/MNM.0000000000000306.

Rosi, N.L., D.A. Giljohann, C.S. Thaxton, A.K.R. Lytton-Jean, M.S. Han, and C.A. Mirkin. 2006. Oligonucleotide-modified gold nanoparticles for intracellular gene regulation. *Science.* 312:1027–1030. doi:10.1126/science.1125559.

Salem, A.K., P.C. Searson, and K.W. Leong. 2003. Multifunctional nanorods for gene delivery. *Nat. Mater.* 2:668–671. doi:10.1038/nmat974.

Saretzki, G. 2014. Extra-telomeric functions of human telomerase: cancer, mitochondria and oxidative stress. *Curr Pharm Des.* 20:6386-6403(18).

Sauerwald, A., S. Sandin, G. Cristofari, S.H.W. Scheres, J. Lingner, and D. Rhodes. 2013. Structure of active dimeric human telomerase. *Nat. Struct. Mol. Biol.* 20:454–460. doi:10.1038/nsmb.2530.

Schmidt, J.C., and T.R. Cech. 2015. Human telomerase: biogenesis, trafficking, recruitment, and activation. *Genes Dev.* 29:1095–1105. doi:10.1101/gad.263863.115.

Seferos, D.S., D.A. Giljohann, N.L. Rosi, and C.A. Mirkin. 2007. Locked nucleic acid–nanoparticle conjugates. *ChemBioChem.* 8:1230–1232. doi:10.1002/cbic.200700262.

Seferos, D.S., A.E. Prigodich, D.A. Giljohann, P.C. Patel, and C.A. Mirkin. 2009. Polyvalent DNA nanoparticle conjugates stabilize nucleic acids. *Nano Lett.* 9:308–311. doi:10.1021/nl802958f.

Sekaran, V., J. Soares, and M.B. Jarstfer. 2014. Telomere maintenance as a target for drug discovery. *J. Med. Chem.* 57:521–538. doi:10.1021/jm400528t.

Shammas, M.A., H. Koley, R.C. Bertheau, P. Neri, M. Fulciniti, P. Tassone, S. Blotta, A. Protopopov, C. Mitsiades, R.B. Batchu, K.C. Anderson, A. Chin, S. Gryaznov, and N.C. Munshi. 2008. Telomerase inhibitor GRN163L inhibits myeloma cell growth in vitro and in vivo. *Leukemia.* 22:1410–1418. doi:10.1038/leu.2008.81.

Sharma, N.K., A. Reyes, P. Green, M.J. Caron, M.G. Bonini, D.M. Gordon, I.J. Holt, and J.H. Santos. 2012. Human telomerase acts as a hTR-independent reverse transcriptase in mitochondria. *Nucleic Acids Res.* 40:712–725. doi:10.1093/nar/gkr758.

Shay, J.W., and S. Bacchetti. 1997. A survey of telomerase activity in human cancer. *Eur. J. Cancer 1990.* 33:787–791. doi:10.1016/S0959-8049(97)00062-2.

Song, L., S. Able, E. Johnson, and K.A. Vallis. 2017. Accumulation of ^{111}In-labelled EGF-Au-PEG nanoparticles in EGFR-positive tumours is enhanced by coadministration of targeting ligand. *Nanotheranostics.* 1:232–243. doi:10.7150/ntno.19952.

Song, L., N. Falzone, and K.A. Vallis. 2016. EGF-coated gold nanoparticles provide an efficient nano-scale delivery system for the molecular radiotherapy of EGFR-positive cancer. *Int. J. Radiat. Biol.* 1–8. doi:10.3109/09553002.2016.1145360.

Storhoff, J.J., R. Elghanian, R.C. Mucic, C.A. Mirkin, and R.L. Letsinger. 1998. One-pot colorimetric differentiation of polynucleotides with single base imperfections using gold nanoparticle probes. *J. Am. Chem. Soc.* 120:1959–1964. doi:10.1021/ja972332i.

Strosberg, J., G. El-Haddad, E. Wolin, A. Hendifar, J. Yao, B. Chasen, E. Mittra, P.L. Kunz, M.H. Kulke, H. Jacene, D. Bushnell, T.M. O'Dorisio, R.P. Baum, H.R. Kulkarni, M. Caplin, R. Lebtahi, T. Hobday, E. Delpassand, E. Van Cutsem, A. Benson, R. Srirajaskanthan, M. Pavel, J. Mora, J. Berlin, E. Grande, N. Reed, E. Seregni, K. Öberg, M. Lopera Sierra, P. Santoro, T. Thevenet, J.L. Erion, P. Ruszniewski, D. Kwekkeboom, and E. Krenning. 2017. Phase 3 trial of 177Lu-Dotatate for midgut neuroendocrine tumors. *N. Engl. J. Med.* 376:125–135. doi:10.1056/NEJMoa1607427.

Su, S., X. Zuo, D. Pan, H. Pei, L. Wang, C. Fan, and W. Huang. 2013. Design and applications of gold nanoparticle conjugates by exploiting biomolecule-gold nanoparticle interactions. *Nanoscale.* 5:2589–2599. doi:10.1039/c3nr33870c.

Subiel, A., R. Ashmore, and G. Schettino. 2016. Standards and methodologies for characterizing radiobiological impact of high-Z nanoparticles. *Theranostics.* 6:1651–1671. doi:10.7150/thno.15019.

Sui, J., Y.-F. Lin, K. Xu, K.-J. Lee, D. Wang, and B.P.C. Chen. 2015. DNA-PKcs phosphorylates hnRNP-A1 to facilitate the RPA-to-POT1 switch and telomere capping after replication. *Nucleic Acids Res.* 43:5971–5983. doi:10.1093/nar/gkv539.

Sulheim, E., J. Kim, A. van Wamel, E. Kim, S. Snipstad, I. Vidic, I.H. Grimstad, M. Widerøe, S.H. Torp, S. Lundgren, D.J. Waxman, and C. de Lange Davies. 2018. Multi-modal characterization of vasculature and nanoparticle accumulation in five tumor xenograft models. *J. Controlled Release.* 279:292–305. doi:10.1016/j.jconrel.2018.04.026.

Sullenger, B.A., and S. Nair. 2016. From the RNA world to the clinic. *Science.* 352:1417–1420. doi:10.1126/science.aad8709.

Taton, T.A., C.A. Mirkin, and R.L. Letsinger. 2000. Scanometric DNA array detection with nanoparticle probes. *Science.* 289:1757–1760.

Tefferi, A., T.L. Lasho, K.H. Begna, M.M. Patnaik, D.L. Zblewski, C.M. Finke, R.R. Laborde, E. Wassie, L. Schimek, C.A. Hanson, N. Gangat, X. Wang, and A. Pardanani. 2015. A pilot study of the telomerase inhibitor imetelstat for myelofibrosis. *N. Engl. J. Med.* 373:908–919. doi:10.1056/NEJMoa1310523.

Templeton, A.C., S. Chen, S.M. Gross, and R.W. Murray. 1999. Water-soluble, isolable gold clusters protected by tiopronin and coenzyme A monolayers. *Langmuir.* 15:66–76. doi:10.1021/la9808420.

Tenzer, S., D. Docter, J. Kuharev, A. Musyanovych, V. Fetz, R. Hecht, F. Schlenk, D. Fischer, K. Kiouptsi, C. Reinhardt, K. Landfester, H. Schild, M. Maskos, S.K. Knauer, and R.H. Stauber. 2013. Rapid formation of plasma protein corona critically affects nanoparticle pathophysiology. *Nat. Nanotechnol.* 8:772–781. doi:10.1038/nnano.2013.181.

Tezel, A., and S. Mitragotri. 2003. Interactions of inertial cavitation bubbles with stratum corneum lipid bilayers during low-frequency sonophoresis. *Biophys. J.* 85:3502–3512. doi:10.1016/S0006-3495(03)74770-5.

Theimer, C.A., and J. Feigon. 2006. Structure and function of telomerase RNA. *Curr. Opin. Struct. Biol.* 16:307–318. doi:10.1016/j.sbi.2006.05.005.

Ting, N.S.Y., B. Pohorelic, Y. Yu, S.P. Lees-Miller, and T.L. Beattie. 2009. The human telomerase RNA component, hTR, activates the DNA-dependent protein kinase to phosphorylate heterogeneous nuclear ribonucleoprotein A1. *Nucleic Acids Res.* 37:6105–6115. doi:10.1093/nar/gkp636.

Ting, N.S.Y., Y. Yu, B. Pohorelic, S.P. Lees-Miller, and T.L. Beattie. 2005. Human Ku70/80 interacts directly with hTR, the RNA component of human telomerase. *Nucleic Acids Res.* 33:2090–2098. doi:10.1093/nar/gki342.

Todorova, N., C. Chiappini, M. Mager, B. Simona, I.I. Patel, M.M. Stevens, and I. Yarovsky. 2014. Surface presentation of functional peptides in solution determines cell internalization efficiency of TAT conjugated nanoparticles. *Nano Lett.* 14:5229–5237. doi:10.1021/nl5021848.

Tokcaer-Keskin, Z., Z.G. Dikmen, F. Ayaloglu-Butun, S. Gultekin, S.M. Gryaznov, and K.C. Akcali. 2010. The effect of telomerase template antagonist GRN163L on bone-marrow-derived rat mesenchymal stem cells is reversible and associated with altered expression of cyclin d1, cdk4 and cdk6. *Stem Cell Rev.* 6:224–233. doi:10.1007/s12015-010-9124-7.

Torchilin, V.P. 2008. Tat peptide-mediated intracellular delivery of pharmaceutical nanocarriers. *Adv. Drug Deliv. Rev.* 60:548–558. doi:10.1016/j.addr.2007.10.008.

Tsoi, K.M., S.A. MacParland, X.-Z. Ma, V.N. Spetzler, J. Echeverri, B. Ouyang, S.M. Fadel, E.A. Sykes, N. Goldaracena, J.M. Kaths, J.B. Conneely, B.A. Alman, M. Selzner, M.A. Ostrowski, O.A. Adeyi, A. Zilman, I.D. McGilvray, and W.C.W. Chan. 2016. Mechanism of hard-nanomaterial clearance by the liver. *Nat. Mater.* 15:1212–1221. doi:10.1038/nmat4718.

Tsutsui, H., and S. Nishiguchi. 2014. Importance of Kupffer Cells in the development of acute liver injuries in mice. *Int. J. Mol. Sci.* 15:7711–7730. doi:10.3390/ijms15057711.

Tyagi, S., and F.R. Kramer. 1996. Molecular beacons: probes that fluoresce upon hybridization. *Nat. Biotechnol.* 14:303–308. doi:10.1038/nbt0396-303.

Uehara, H., G. Nardone, I. Nazarenko, and R.J. Hohman. 1999. Detection of telomerase activity utilizing energy transfer primers: comparison with gel- and ELISA-based detection. *BioTechniques.* 26:552–558.

Venteicher, A.S., Z. Meng, P.J. Mason, T.D. Veenstra, and S.E. Artandi. 2008. Identification of ATPases pontin and reptin as telomerase components essential for holoenzyme assembly. *Cell.* 132:945–957. doi:10.1016/j.cell.2008.01.019.

Vivès, E., P. Brodin, and B. Lebleu. 1997. A truncated HIV-1 Tat protein basic domain rapidly translocates through the plasma membrane and accumulates in the cell nucleus. *J. Biol. Chem.* 272:16010–16017. doi:10.1074/jbc.272.25.16010.

Wadia, J.S., R.V. Stan, and S.F. Dowdy. 2004. Transducible TAT-HA fusogenic peptide enhances escape of TAT-fusion proteins after lipid raft macropinocytosis. *Nat. Med.* 10:310–315. doi:10.1038/nm996.

Waghorn, P.A., M.R. Jackson, V. Gouverneur, and K.A. Vallis. 2017. Targeting telomerase with radiolabeled inhibitors. *Eur. J. Med. Chem.* 125:117–129. doi:10.1016/j.ejmech.2016.09.028.

Wang, C., Y. Jiang, X. Li, and L. Hu. 2015. Thioglucose-bound gold nanoparticles increase the radiosensitivity of a triple-negative breast cancer cell line (MDA-MB-231). *Breast Cancer.* 22:413–420. doi:10.1007/s12282-013-0496-9.

Wang, J., L. Wu, J. Ren, and X. Qu. 2012. Visualizing human telomerase activity with primer-modified Au nanoparticles. *Small.* 8:259–264. doi:10.1002/smll.201101938.

Weissig, V., and D. Guzman-Villanueva. 2015. Nanopharmaceuticals (part 2): products in the pipeline. *Int. J. Nanomedicine.* 10:1245–1257. doi:10.2147/IJN.S65526.

Wilhelm, S., A.J. Tavares, Q. Dai, S. Ohta, J. Audet, H.F. Dvorak, and W.C.W. Chan. 2016. Analysis of nanoparticle delivery to tumours. *Nat. Rev. Mater.* 1:16014. doi:10.1038/natrevmats.2016.14.

Williams, S.C.P. 2013. No end in sight for telomerase-targeted cancer drugs. *Nat. Med.* 19:6. doi:10.1038/nm0113-6.

Wong, K.K., S. Chang, S.R. Weiler, S. Ganesan, J. Chaudhuri, C. Zhu, S.E. Artandi, K.L. Rudolph, G.J. Gottlieb, L. Chin, F.W. Alt, and R.A. DePinho. 2000. Telomere dysfunction impairs DNA repair and enhances sensitivity to ionizing radiation. *Nat. Genet.* 26:85–88. doi:10.1038/79232.

Wu, R.A., H.E. Upton, J.M. Vogan, and K. Collins. 2017a. Telomerase Mechanism of Telomere Synthesis. *Annu. Rev. Biochem.* 86:439–460. doi:10.1146/annurev-biochem-061516-045019.

Wu, W., S. Wieckowski, G. Pastorin, M. Benincasa, C. Klumpp, J.-P. Briand, R. Gennaro, M. Prato, and A. Bianco. 2005. Targeted delivery of amphotericin B to cells by using functionalized carbon nanotubes. *Angew. Chem.* 44:6358–6362. doi:10.1002/anie.200501613.

Wu, X., S. Smavadati, K. Nordfjäll, K. Karlsson, F. Qvarnström, M. Simonsson, M. Bergqvist, S. Gryaznov, S. Ekman, and Y. Paulsson-Karlsson. 2012. Telomerase antagonist imetelstat inhibits esophageal cancer cell growth and increases radiation-induced DNA breaks. *Biochim. Biophys. Acta.* 1823:2130–2135. doi:10.1016/j.bbamcr.2012.08.003.

Wu, X., J. Zhang, S. Yang, Z. Kuang, G. Tan, G. Yang, Q. Wei, and Z. Guo. 2017b. Telomerase antagonist imetelstat increases radiation sensitivity in esophageal squamous cell carcinoma. *Oncotarget.* 8:13600–13619. doi:10.18632/oncotarget.14618.

Xiao, Y., K.Y. Dane, T. Uzawa, A. Csordas, J. Qian, H.T. Soh, P.S. Daugherty, E.T. Lagally, A.J. Heeger, and K.W. Plaxco. 2010. Detection of telomerase activity in high concentration of cell lysates using primer-modified gold nanoparticles. *J. Am. Chem. Soc.* 132:15299–15307. doi:10.1021/ja106513f.

Xu, P., E.A. Van Kirk, Y. Zhan, W.J. Murdoch, M. Radosz, and Y. Shen. 2007. Targeted charge-reversal nanoparticles for nuclear drug delivery. *Angew. Chem.* 46:4999–5002. doi:10.1002/anie.200605254.

Yamamoto, T., M. Nakatani, K. Narukawa, and S. Obika. 2011. Antisense drug discovery and development. *Future Med. Chem.* 3:339–365. doi:10.4155/fmc.11.2.

Yi, W.-J., J. Yang, C. Li, H.-Y. Wang, C.-W. Liu, L. Tao, S.-X. Cheng, R.-X. Zhuo, and X.-Z. Zhang. 2012. Enhanced nuclear import and transfection efficiency of TAT peptide-based gene delivery systems modified by additional nuclear localization signals. *Bioconjug. Chem.* 23:125–134. doi:10.1021/bc2005472.

Yu, C., Y. Yu, Z. Xu, H. Li, D. Yang, M. Xiang, Y. Zuo, S. Li, Z. Chen, and Z. Yu. 2015. Antisense oligonucleotides targeting human telomerase mRNA increases the radiosensitivity of nasopharyngeal carcinoma cells. *Mol. Med. Rep.* 11:2825–2830. doi:10.3892/mmr.2014.3105.

Zhang, Q., N.-K. Kim, and J. Feigon. 2011. Architecture of human telomerase RNA. *Proc. Natl. Acad. Sci.* 108:20325–20332. doi:10.1073/pnas.1100279108.

Zhang, Y., Q. He, Z. Hu, Y. Feng, L. Fan, Z. Tang, J. Yuan, W. Shan, C. Li, X. Hu, J.L. Tanyi, Y. Fan, Q. Huang, K. Montone, C.V. Dang, and L. Zhang. 2016a. Long noncoding RNA LINP1 regulates repair of DNA double-strand breaks in triple-negative breast cancer. *Nat. Struct. Mol. Biol.* 23:522–530. doi:10.1038/nsmb.3211.

Zhang, Y., J. Yu, H.N. Bomba, Y. Zhu, and Z. Gu. 2016b. Mechanical force-triggered drug delivery. *Chem. Rev.* 116:12536–12563. doi:10.1021/acs.chemrev.6b00369.

Zheng, T., S. Bott, and Q. Huo. 2016. Techniques for accurate sizing of gold nanoparticles using dynamic light scattering with particular application to chemical and biological sensing based on aggregate formation. *ACS Appl. Mater. Interfaces.* 8:21585–21594. doi:10.1021/acsami.6b06903.

Zong, S., Z. Wang, H. Chen, and Y. Cui. 2013. Ultrasensitive telomerase activity detection by telomeric elongation controlled surface enhanced Raman scattering. *Small.* 9:4215–4220. doi:10.1002/smll.201301372.

Zou, Y., A. Sfeir, S.M. Gryaznov, J.W. Shay, and W.E. Wright. 2004. Does a sentinel or a subset of short telomeres determine replicative senescence? *Mol. Biol. Cell.* 15:3709–3718. doi:10.1091/mbc.E04-03-0207.